Journal of Materials Chemistry A

# Recent Progress of High Entropy Materials for Energy Storage and Conversion

| | |
|---|---|
| Journal: | *Journal of Materials Chemistry A* |
| Manuscript ID | TA-REV-09-2020-009578.R1 |
| Article Type: | Review Article |
| Date Submitted by the Author: | 24-Nov-2020 |
| Complete List of Authors: | Shahbazian-Yassar, Reza; University of Illinois at Chicago, Mechanical and Industrial Engineering; University of Illinois at Chicago<br>Amiri, Azadeh; University of Illinois at Chicago |
| | |

ARTICLE

# Recent Progress of High-Entropy Materials for Energy Storage and Conversion

Received 00th January 20xx,
Accepted 00th January 20xx

DOI: 10.1039/x0xx00000x

Azadeh Amiri [a] and Reza Shahbazian-Yassar *[a]

The emergence of high-entropy materials (HEMs) with their excellent mechanical properties, stability at high temperatures, and high chemical stability is poised to yield new advancement in the performance of energy storage and conversion technologies. This review covers the recent developments in catalysis, water splitting, fuel cells, batteries, supercapacitors, and hydrogen storage enabled by the HEMs covering metallic, oxides, and non-oxide alloys. Here, first, the primary rules for the proper selection of the elements and the formation of a favorable single solid solution phase in HEMs are defined. Further, recent developments in different fields of energy conversion and storage achieved by HEMs are reviewed and discussed. Higher electrocatalytic and catalytic activity with longer cycling stability and durability compared to conventional noble metal-based catalysts are reported for high-entropy materials. In electrochemical energy storage systems, high-entropy oxides and alloys have shown superior performance as anode and cathode materials with long cycling stability and high capacity retention. Also, used as metal hydride for hydrogen storage, remarkable high hydrogen storage capacity and structural stability are observed for HEAs. At the end, the future directions and new energy-related technologies that can be enabled by the application of HEMs are outlined.

## 1. Introduction

Over the years, the alloying strategy was limited to adding small fractions of other elements into a base element to obtain the new composite material with improved properties. In this approach, limited types of possible alloys can be developed using different base elements, and most of them are already explored and identified. A new method of alloying emerged in 2004, by two research groups[1,2] independently, introducing single-phase solid solution alloys of five or more principal elements with near-equimolar compositions. Yeh *et al.* [2] first introduced the concept of high-entropy alloys (HEAs) based on the fact that configurational entropy of mixing ($\Delta S_{mix}$ from Equation 1) increases with adding more equimolar principle elements to the alloy system.

$$\Delta S_{mix} = -R\sum_{i=1}^{n} c_i \ln c_i = -R\sum_{n} \frac{1}{n}\ln\frac{1}{n} = R\ln n \qquad (1)$$

(n is the number of elements, $c_i$ is the concentration of component i and R is the gas constant)

Based on this hypothesis, the thermodynamic contribution of high $\Delta S_{mix}$ in a system with a minimum of five equimolar elements to the Gibbs free energy ($\Delta G_{mix}$) at high temperature is enough to compensate for the enthalpy formation ($\Delta H_{mix}$) of intermetallic compounds and form a single-phase solution of multiple elements ($\Delta G_{mix} \leq 0$ from Equation 2). Later the definition of HEA expanded to alloys composed of five or more elements with compositions between 5% to 35% (composition-based definition)[3] and multi-elemental alloys with $\Delta S_{mix} > 1.5R$ (entropy-based definition)[4].

$$\Delta G_{mix} = \Delta H_{mix} - T\Delta S_{mix} \qquad (2)$$

Having multiple elements with different characters gives the HEAs four core effects of (1) high-entropy, (2) lattice distortion, (3) sluggish diffusion, and (4) cocktail effect (Figure 1). The high-entropy effect is the main concept of HEMs when having multiple near-equimolar components increase the configurational entropy (Equation 1) and stability of the single-phase structure at higher temperature.[5] Crystal lattice of HEA is composed of atoms with different sizes randomly occupying lattice sites. These slightly unbalanced sites of the lattice and random positions of atoms lead to severe lattice distortion. The lattice distortion is known as the reason for lower intensity in X-ray diffraction peaks[6–8], lower thermal and electrical conductivity[7,8], as well as the higher hardness of these materials[7,8]. In addition, the lattice distortion of HEAs can delay atomic movement and replacements and results in another effect called sluggish diffusion.[2,8] The sluggish diffusion effect may lead to the formation of nano-precipitate or amorphous phases in as-cast HEAs.[2] Finally, the cocktail effect of HEA comes having multiple elements with various properties in a mixture[5]. The final property of alloy is not equal to the sum of the properties of components and is unpredictable.[5,7] The synergetic mixture of elements results in HEA with excellent features as functional materials in energy storage and conversion systems.

[a] Department of Mechanical and Industrial Engineering, University of Illinois, Chicago, IL 60607, USA. E-mail: rsyassar@uic.edu

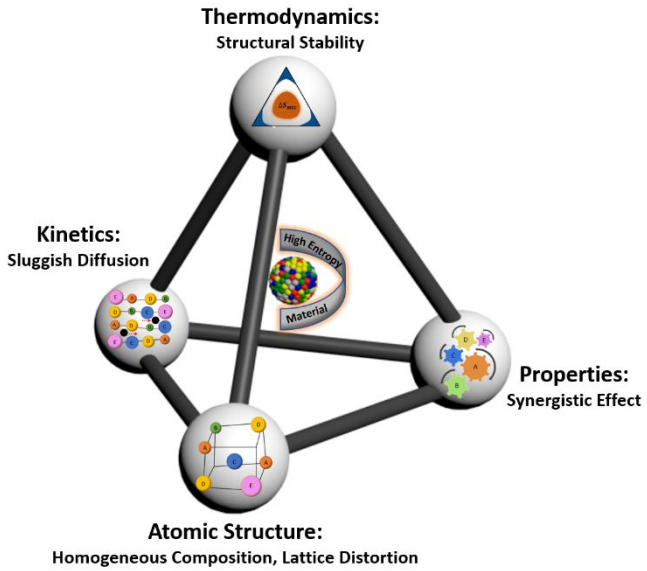


**Figure 1 -** The schematic showcases the four core effects of HEMs

The concept of high-entropy stabilized multi-element alloys and their astonishing properties later extended to oxides and other systems. Rost *et al*. [9] explored the idea of entropy-driven stabilization in a mixture of five metal oxide to form a single solid solution with a rock-salt crystalline structure. Similar to multi-elemental alloys, here, the configurational disorder can increase with the addition of different metal cations to a single cation sublattice when the anion sublattice is only occupied by oxygen. Therefore, the configurational entropy of multi-elemental oxides can be obtained from Equation 3:

$$\Delta S_{mix} = -R\left[\left(\sum_{i=1}^{n} c_i \ln c_i\right)_{cation-site} + \left(\sum_{i=1}^{n} c_i \ln c_i\right)_{anion-site}\right] \quad (3)$$

Having oxygen as the single anion in ionic structure, the second term for anion-sites is zero and the entropy increases by adding to the total number of cations. Later, several other multi-elemental oxides with fluorite[10–12], perovskite[13,14], and spinel[15,16] crystal structures materialized and broadened the variety of high-entropy oxide included in this approach. The concept of entropy-stabilized metallic, oxide and non-oxide ceramic materials can be generalized to high-entropy materials (HEMs), considering the development of new types of high-entropy ceramics such as carbides[17–20], diborides[21,22], nitrides[23] and silicides[24], sulfides[25] as well as phosphides[26] and fluorides[27]. Zeolite[28] and Metal-organic framework (MOF)[29,30] with five near-equimolar active metallic elements are the other forms of organic-inorganic HEMs.

The high-entropy concept is not limited to inorganic materials and is not defined by only the number of elements and compositional disorder. High-entropy configuration for organic materials such as polymers and carbon material can be considered as an effective way of designing interesting new materials. In this regard, the entropy is depicted as the degree of disorder of the system. Feng and Zhuang[31] introduced the concept of meso-entropy carbon materials. Considering the value of entropy of each form of carbon allotropes, the meso-entropy of materials can be designed between the high and low entropy form. The level of disorder and entropy value can be manipulated by changes in the structure of carbon materials like the number of members in carbon rings. High entropy can also be considered for organic semicrystalline copolymers materials as high-entropy polymers. Having different types of polymers with various ratios in repeating units increases the lattice-packing entropy and can affect the phase transition of crystalline polymers.[32]

Some of the fundamental aspects, structural effects, and designing strategies of HEAs are discussed in recent years.[5,33–38] Research on HEOs and other HEMs are more recent and less established compared to that on metallic alloys. Due to some appealing and advantageous features like synergistic effect, high-temperature stability, and corrosion-resistant, HEMs are excellent candidates in various energy-related applications. [39,40] In this respect, the focus of this work is to review the emerging applications and performances of all the HEMs in catalysis and energy conversion and storage applications reported in the literature. Afterward, considering the confirmed or possible capabilities of HEMs, other prospective applications of these materials in various energy-related systems are discussed. But first, the general criteria for the proper selection of elements in HEM for the formation of the favorable single solid solution phase are addressed and classified.

## 2. Parameters affecting HEAs formation

A few years after introducing HEAs, comparing different experimental results showed that not all the HEAs exhibit a single crystallin solid-solution phase.[41] There are HEAs in an amorphous phase like high-entropy bulk metallic glasses and multi-phase alloys with intermetallic compounds as well as solid solutions with ordered structure.[41,42] This indicates that the entropy-driven effect from Equation 1 is not the only factor in determining the thermodynamically stable phases in multi-component alloys. The entropy of mixing from Equation 1 is defined for ideal solutions.[41] However, for the non-ideal regular solutions, there is always a deviation from the ideal case, and configurational entropy is not precisely equal to the value calculated[41]. In this respect, several research studies[41–49] attempted to investigate the effect of other parameters to define more reliable thermodynamic criteria for phase selection of multi-component HEMs. Most of the studies are statistical analysis on a large database of synthesized HEAs with their reported phase or phases and with the focus on factors distinguishing the condition required for solid solution phase formation over the intermetallic compounds. It should be mentioned that the high-entropy and other factors that favor the formation of solid solution over other intermetallic phases result in enhancing the mechanical properties of HEAs due to the solution hardening effect, which increases the overall strength and ductility of the materials.[39] A summary of these new parameters and their effects on the prediction of phase formation is described below.

### 2.1 Enthalpy of mixing ($\Delta H_{mix}$)

Zhang *et al.*[41] investigated the effect of mixing enthalpy ($\Delta H_{mix}$) on existing phases in HEAs reported in the literature. $\Delta H_{mix}$ for each multi-component system can be calculated based on Miedema's model[50] from the following equation:

$$\Delta H_{mix} = \sum_{i=1, i\neq j}^{n} 4\Delta H_{mix}^{AB} c_i c_j \quad (3)$$

where n is the number of components, $c_i$ and $c_j$ are the concentrations of components i and j, respectively; and $\Delta H_{mix}^{AB}$ is the mixing enthalpy of those two components (i&j) in their AB-type binary mixture. Later Guo and Liu42, with a similar statistical analysis in a larger database, studied the role of mixing enthalpy as one of the determining parameters on the formation of different phases in multi-component alloys. Their analysis concluded that a solid solution (data mixed with intermetallic) forms only when mixing enthalpy is moderately positive or not very negative (-22 ≤ $\Delta H_{mix}$ ≤ 7 kJ.mol-1) while amorphous phase forms at more negative mixing enthalpies (-49 ≤ $\Delta H_{mix}$ ≤ -5.5 kJ.mol-1) (Figure 2a). From the proposed idea of HEAs formation and based on Equation 2, when the entropy contribution to the Gibbs free energy at high temperature is larger than that of enthalpy, the solid solution is likely formed. As mentioned before, only for an ideal solution, the calculated mixing entropy from Equation 1 is an exact value; and there are deviations and excess amounts for regular solutions. Besides, for an ideal solution, the enthalpy of mixing is zero ($\Delta H_{ideal-mix} = 0$) but it has a negative or positive value ($|\Delta H_{real-mix}| >$) for non-ideal solutions. The designated range of $\Delta H_{mix}$ for the formation of solid solution phase evidence that when the absolute value of mixing enthalpy is small, the regular solution is closer to an ideal case. Therefore, the low magnitude of $\Delta H_{mix}$ is more favorable for the formation of single-phase solid solutions. On the other hand, elements are less willing to randomly distribute in the solution due to higher binding energies between them at more negative $\Delta H_{mix}$ and their miscibility gaps at more positive $\Delta H_{mix}$.

### 2.2 Atomic size difference ($\delta$)

The difference in the atomic size of the elements in a mixture turns out to be an important and critical factor affecting the phase selection of multi-component alloys. When the atomic sizes of the components are quite similar, they all have an equal probability of locating in any of the crystal lattice sites, and their random distribution leads to a disordered structure of the solid solution. For the non-ideal real mixture of multiple components, there is an atomic size mismatch effect. The effect of this parameter on the phase stability of multi-component alloys was also first studied by Zhang *et al*. [41] by calculating the $\delta$ parameter for HEAs from the following equation:

$$\delta = 100\sqrt{\sum_{i=1}^{n} c_i\left(1-\frac{r_i}{\bar{r}}\right)^2} \quad , \quad \bar{r} = \sum_{i=1}^{n} c_i r_i \quad (4)$$

where n is the number of components, $c_i$ is the concentration of component i, $r_i$ is the atomic radius of component i and $\bar{r}$ is the average atomic size of the n components in alloy. The role of $\delta$ as a separate parameter was evaluated in several studies to find its critical value for phase selection. The analysis by Guo and Liu[42] concluded that solid solution (data mixed with intermetallic) forms only when the atomic-size difference of elements is small ($\delta \leq 8.5$) while amorphous phase forms at the larger difference in atomic-size of components ($\delta \geq 9$) (Figure 2b). Yang and Zhang[43] narrowed down the specified range of $\delta$ for the formation of solid solutions exclusively. Their evaluations led to a rule of $\delta \leq 6.6$ for solid solution phase selection over intermetallic compounds (Figure 3a). Differences in atomic sizes are important factors affecting the lattice distortion of HEAs. Lattice distortion can reduce the thermal and electrical conductivity due to the scattering of electron and phonons.[39] Also, the peak intensities of X-ray diffraction are largely decreased as a result of scattering by distorted lattice planes.[51]

### 2.3 Electronegativity difference ($\Delta\chi$)

The effect of the difference in electronegativity of elements in HEAs is another parameter studied for phase selection criteria. Guo and Liu[42] considered the Pauling electronegativity of elements in the mixture to calculate their electronegativity difference from the following equation:

$$\Delta\chi = \sqrt{\sum_{i=1}^{n} c_i(\chi_i - \bar{\chi})^2} \quad , \quad \bar{\chi} = \sum_{i=1}^{n} c_i\chi_i \quad (5)$$

where n is the number of components, $c_i$ is the concentration of component i, $\chi_i$ is the Pauling electronegativity of component i and $\bar{\chi}$ is the average electronegativity of the n components in alloy. However, in their study, $\Delta\chi$ exhibited no significant determinative effect on the formation of solid solutions, intermetallic, and amorphous phases (Figure 2c). Later Poletti and Battezzati[49] used a similar factor but considering Allen electronegativity ($\chi_{Allen}$)[52] of components and reported that

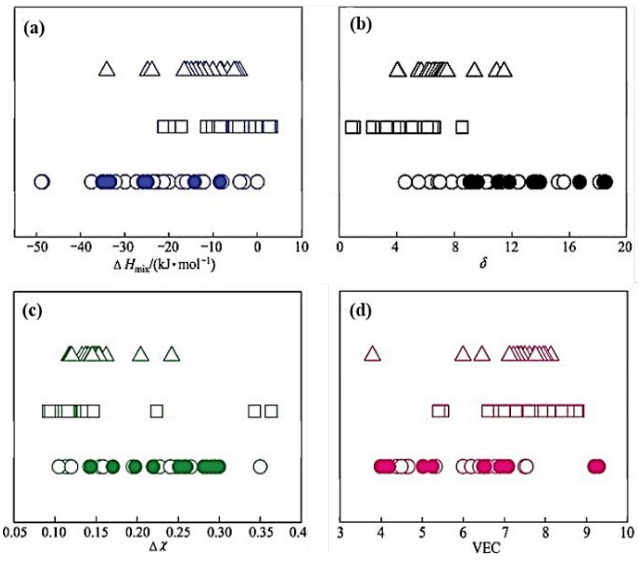


**Figure 2 -** Effect of (a) $\Delta H_{mix}$, (b) $\delta$, (c) $\Delta\chi$, and (d) VEC on phase stability in HEAs. The symbols □, △, ○ and ● represent solid solution phase, intermetallic phase, equimolar amorphous phase, and non-equimolar amorphous phase, respectively. Reproduced with permission (ref. [40]). Copyright 2011, Elsevier.

$3 < \Delta\chi_{Allen} < 6$ is the scope that only solid solution phase forms (Figure 3b).

### 2.4 Valance electron concentration (VEC)

Valance electron concentration (VEC) is the total number of electrons in the outer shell of an atom. VEC for a multi-component system is defined based on the following weighted-average equation:

$$VEC = \sum_{i=1}^{n} c_i \mathrm{VEC}_i \qquad (6)$$

where n is the number of components, $c_i$ are the concentration of component *i* and $\mathrm{VEC}_i$ is the valance electron concentration of component *i.* VEC did not show any controlling effect on the phase stability of HEAs (Figure 2d).[40] However, VEC was found to play an essential role in governing the crystallin structure types of solid solution HEAs. Most of the reported solid solution HEAs have FCC and BCC structures, but a limited number of HCP-type HEAs based on heavy lanthanides metals are reported[53–55]. The study on the effect of VEC on the crystallography of HEAs by Guo *et al*.[46] suggested that VEC ≥ 8 and VEC $<$ 6.87 favor FCC and BCC structures, respectively, while VEC between these values showed mixed FCC+BCC structure.[56] However, no HEAs reported with $\mathrm{VEC} < 5$ were included in this study. Later HEAs with HCP solid solution structure composed of heavy lanthanide group elements with $\mathrm{VEC}_i$ of 3 were reported.[46] Therefore, VEC has a critical role in determining the crystal structure of HEAs and physical properties related to FCC or BCC structures.[57] HEAs with FCC structure have good ductility due to strain hardening but lower strength[58] while solid solutions with BCC structure have higher strength because of solution hardening but are more brittle because of lower ductility compared to FCC alloys.[59]

### 2.5 $\Omega$ Parameter

Another parameter for phase formation prediction in multi-component alloys is $\Omega$ parameter. Defined by Yang and Zhang[43]; $\Omega$ is the ratio of entropic contribution to Gibbs free energy at high temperature to enthalpic input and is calculated from the following equation:

$$\Omega = \frac{T_m \Delta S_{mix}}{|\Delta H_{mix}|} \quad , \quad T_m = \sum_{i=1}^{n} c_i T_{mi} \qquad (7)$$

where n is the number of components, $c_i$ is the concentration of component i, $T_{mi}$ is the melting point of component i and $T_m$ is the weighted average melting point for mixture of n components. Considering the atomic size difference effect with $\delta$ parameter and the ratio of entropy to enthalpy effect with $\Omega$ parameter, the required conditions for phases stability of solid solution are $\Omega \geq 1.1$ and $\delta \leq 6$ (Figure 3a).

### 2.6 Excess entropy ($S_E$)

The configurational entropy of mixing ($S_C$) for an ideal mixture of n components is only dependent on the concentration of elements ($S_C = \Delta S_{mix}$) and reaches its maximum when components are in equal atomic concentrations (Equation 1). However, a non-ideal or real solution is composed of atoms with different sizes and packing fractions, which makes its total configurational mixing entropy deviate from the ideal case. The excess entropy ($S_E$)[48] can represent the difference between the configurational mixing entropy for the ideal solution and regular

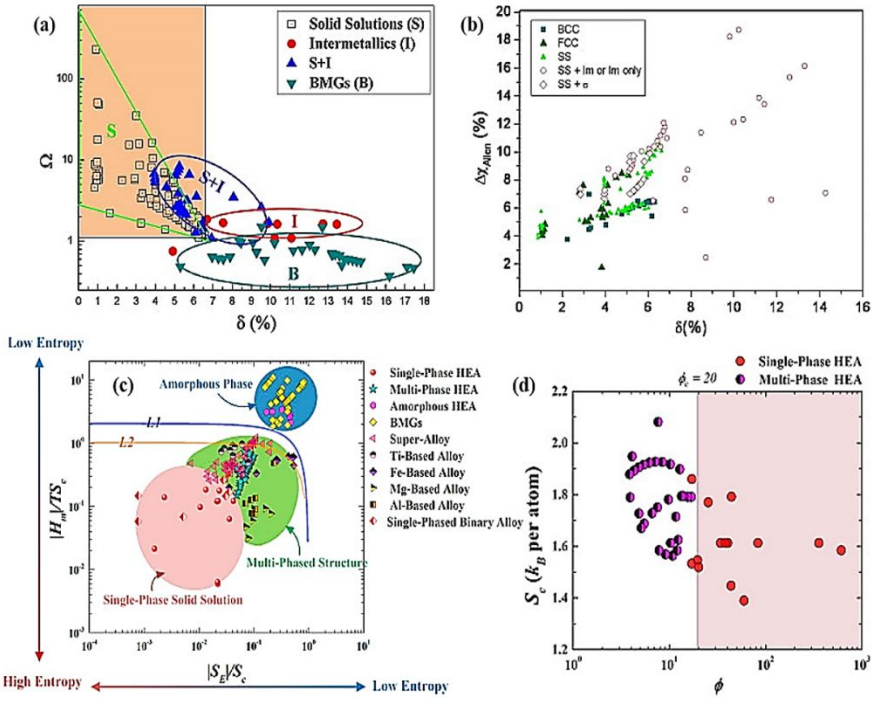


**Figure 3 -** Effect of (a) Ω and δ parameters (Reproduced with permission (ref. [36]). Copyright 2012, Elsevier.), (b) $\chi_{Allen}$ and δ parameters (Reproduced with permission (ref.[42]). Copyright 2014, Elsevier.), (c) $|S_E|/S_C$ and $|H_m|/(TS_C)$ terms (Reproduced with permission (ref. [41]). Copyright 2015, Elsevier.), and (d) single Ø parameter (Reproduced with permission (ref. [40]). Copyright 2015, Elsevier.); on phase stability in HEAs.

mixture (Equation 8). Unlike $S_C$ of an ideal solution, $S_E$ and subsequently, total mixing entropy ($S_T$) of a real solution depend not only on the concentration of elements ($c_i$) but also on their atomic radiuses ($r_i$) and packing densities ($\xi$) (according to the hard-sphere model[60]).

$$S_T(c_i,r_i,\xi) = S_C(c_i) + S_E(c_i,r_i,\xi) \quad (8)$$

Ye et al.[48] substituted mixing entropy ($S_{mix}$) in Equation 2 with $S_T$ and expressed the following condition required for the formation of a single solid solution phase in a multi-component mixture:

$$\frac{|S_E|}{S_C} \ll 1 - \frac{|H_m|}{TS_C} \quad (9)$$

Based on this theory, they investigated the effect of $S_E$ on phase selection of mixtures by calculating and plotting two terms of $|S_E|/S_C$ and $|H_m|/TS_C$ for a large number of HEAs in literature. The result implied that lower ratios of these two terms are more favorable for the entropy-dominant formation of single-phase solid solution while at higher ratios, multiphase solid solutions and intermetallic phases tend to be formed (Figure 3c). Higher excess entropy and enthalpy of mixing can be seen in multi-component systems with an amorphous phase, and their formation is mostly enthalpic favorable (Figure 3c).

### 2.7 Ø parameter

The discussed impacts of excess entropy and mixing enthalpy on phase formation criteria for HEAs were later combined by Ye et al. [47] in a single parameter of Ø defined as following:

$$Ø = \frac{S_C - (\frac{|\Delta H_{mix}|}{T_m})}{|S_E|} \quad (10)$$

Applying this parameter to the literature database denoted that there is a critical value of $Ø_c = 20$, which separates regions of single-phase and multi-phases (Figure 3d). Therefore, a single parameter rule of $Ø > Ø_c$ was proposed to design the single-phase HEAs.

### 2.8 Λ Geometric parameter

Singh *et al.*[45] introduced a new purely geometric parameter of $\Lambda$ (Equation 11) and compared it with previous ruling parameters. They concluded that for $(\Lambda > 0.96)$, $(0.24 < \Lambda < 0.96)$ and $(\Lambda < 0.24)$, single-phase, two-phase, and multi-phase HEAs are expected to be formed, respectively.

$$\Lambda = \frac{\Delta S_{mix}}{\delta^2} \quad (11)$$

### 2.9 Effect of kinetic on phase formation:

Most of the studies on the phase stability of HEAs and all the mentioned phase controlling parameters are from a thermodynamic point of view and focusing on the detected phases in HEAs samples at their thermodynamic equilibrium state (parameters in Figure 4). However, for practical applications, it is vital to assess the structure and existing phases in samples after all cooling, solidification, and annealing steps. In this regard, kinetic effects play a considerable role in the phase stability of HEAs, especially in the formation of intermetallic phases in a system with an as-cast single solid solution phase.[61] He *et al.*[62] examined the impact of rapid and slow cooling rates for both solidification and solid-state phase transformation after annealing of $CoCrFeNiTi_{0.4}$ HEA as an example. It was observed that the formation of different intermetallic phases decreases in higher cooling rates and faster kinetics. This simply suggests that phase selection in HEAs can be tailored by controlling the kinetic factors during synthesis. Luan *et al.*[63] presented a perturbation model related to the number of elements and temperature to evaluate the stabilities of single-phase HEAs compared to the formation of possible intermetallic. This model shows that with an increase in the number of elements, the number of possible intermetallic consisting of different combinations of those elements increases and leads to destabilization of single-phase solid solution and formation of multiphase structure. In other words, the increase in the number of elements is entropically favorable for the formation of a single-phase solid solution; but it also contributes to the unfavorable enthalpic contribution to the total free Gibs energy of mixing. This fact points out the essential impact of high temperature on the phase stability of HEAs since it decreases the Gibs free energy and boost the stability of single-phase solid solutions. Therefore, based on the thermodynamic factors, most of the single-phase HEAs formed at high temperatures are not stable at room temperature and are expected to be in multiphase structure. However, the kinetic factors during synthesis such as fast cooling and sluggish dynamic effect of multicomponent systems considerably control the formation and stability of the single-phase HEAs at room temperature.

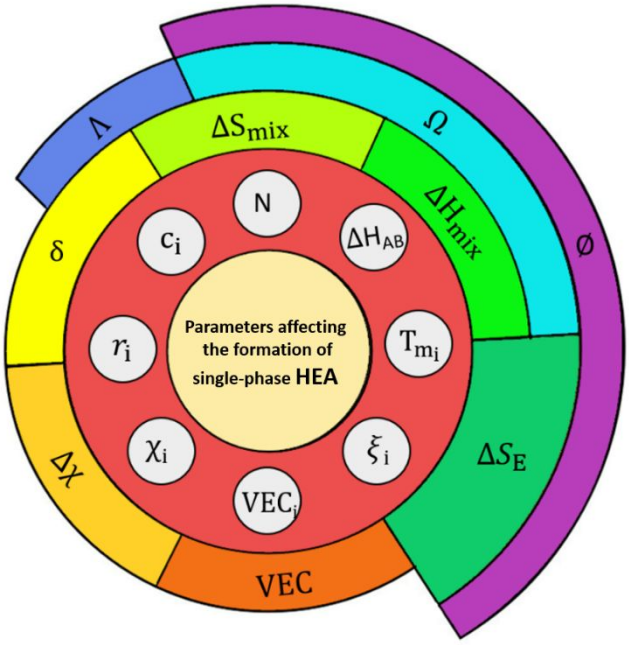


**Figure 4 -** Parameters affecting the formation of single-phase HEAs

## 3. Parameters affecting HEOs formation

Generally, thermodynamic rules for phase stability of HEAs correspondingly apply to HEOs with adjustments for an ionic crystal structure. However, due to the limited number of successfully synthesized oxide and non-oxide HEMs in research studies, no statistical analysis on the database has been done yet to confirm their practical effects. Here, we address the general principles of choosing appropriate constituents for the formation of single-phase HEOs based on the so far reported works.

### 3.1 Enthalpy of mixing $(\Delta H_{mix})$

The effect of mixing enthalpy for HEOs is quite similar to HEAs, which is preferred to be near zero. Large positive $\Delta H_{mix}$ of metal oxides with different structures might not be compensated by the high-entropy effect or requires a much higher temperature for phase transition and mixing to happen.[9,64] On the other hand, large negative $\Delta H_{mix}$ of extensive soluble metal oxides are not favorable for entropy dominate formation of a single-phase mixed oxide. In this aim, metal oxide with different crystal structures (e.g., rock-salt, wurtzite) or cation coordination is an appropriate candidate to be selected. Rost *et al*. [9] used five equimolar metal oxides with rock-salt (MgO, CoO and NiO), tenorite (CuO) and wurtzite (ZnO) crystal structures and synthesized a HEO with single-phase rock-salt crystallin structure. In this case, even with the ideal mixing entropy of zero, there is positive structural transition enthalpy for tenorite and wurtzite to final rock-salt structure. Therefore, the formation of the single-phase mixed oxides with rock-salt structure is entropy favorable and is called entropy-stabilized oxide. Among all possible prototype oxides of metal cations, at least one should have a different crystal structure to prove the entropy-stabilization of the product single-phase HEO.

### 3.2 Ionic radius

In the same way as the difference in atomic size radius $(\delta)$ for HEAs, the ionic radius of metal cations affects lattice distortion and formation of single-phase HEOs. In order to obtain single-phase HEOs with cubic rock-salt or fluorite structure, choosing metal cations with similar cationic radius $(r_c)$ is considered.[9,12] In $ABO_3$ type perovskite HEOs with a primitive cubic structure in which either or both A and B cation sites can be composed of multiple oxides, the ionic radius differences are calculated separately for each of multi cationic sites as $\delta_{rA}$ and $\delta_{rB}$. However, the formation of single-phase high-entropy perovskite oxide did not follow the atomic size difference range of $\delta < 6.5\%$ and occurred even in larger $\delta_{rB}$ of 11-13%.[14] Therefore, other structural factors of Goldschmidt's tolerance factor (t) for the stability of perovskite cubic structure from the following equation were applied to the multi-component systems:

$$t = \frac{\bar{r}_A + r_O}{\sqrt{2}\,(\bar{r}_B + r_O)} \qquad (12)$$

where $\bar{r}_A$ and $\bar{r}_B$ are the weighted average ionic radius of cations in A and B sites, respectively, and $r_O$ is radius of the oxygen anion. A cubic phase is likely stable if $0.9 \le t \le 1.0$, while a hexagonal or tetragonal phase may form if $t > 1.0$ and an orthorhombic or rhombohedral phase may form if $t < 0.9$. The experiments suggested that the Goldschmidt tolerance factor close to unity ($t \approx 1.00$) is perhaps a necessary but not sufficient criterion to form a single high-entropy perovskite phase.[13,14]

### 3.3 Oxidation State

In a single-phase multi-cation HEO, isovalent metal cations occupy the same cation sublattice sites, and anions preserve electroneutrality of the lattice.[9,40] Therefore, the affinity of an element towards a particular oxidation state plays a crucial role in the formation of single-phase HEO and type of the crystal structure. In a cubic Rock-Salt multi-cation oxide, metals have an equal oxidation state of +2 ($M^{2+}$) and oxide form of MO (like transition metals), but in the Fluorite structure, they have a similar oxidation state of +4 ($M^{4+}$) and oxide form of $MO_2$ (like rare-earth metals). In an $ABO_3$ perovskite HEOs, the oxidation state of A and B sites could be similar (+III) or different (+II and +IV); however, all cations in the same sublattice have the same oxidation state. The critical role of some cations in the formation and stability of single-phase HEOs has been observed and attributed to a more stable form of those cations in a specific oxidation state.[10]

### 3.4 Cation Coordination number

In an ionic crystal structure, each ion is surrounded by other ions (cations and anions). The number of ions that immediately surround a particular ion is the coordination number (C.N) and it depends on the relative size of ions. All cations occupying the same sublattice have the same coordination number. In perovskite oxide with two cation sublattices, the A sites are occupied by larger cations with CN of 12 and B sites by smaller cations with CN of 6.

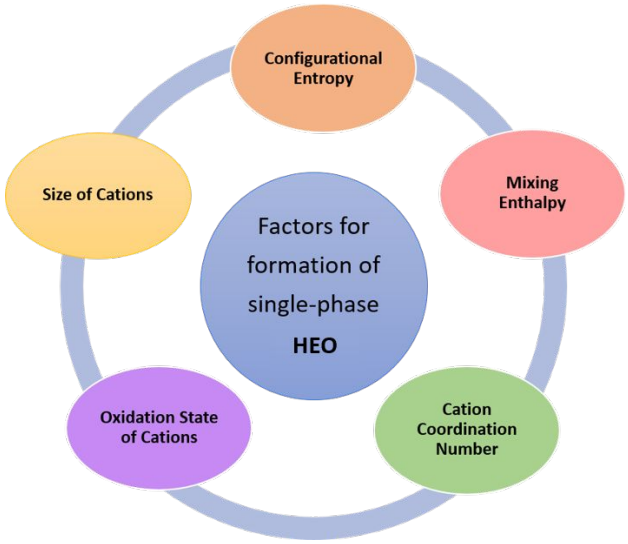


**Figure 5 -** Parameters affecting the formation of single-phase HEOs

## 4. Synthesis Methods and Characterization Techniques for Crystallin HEMs

There are different physical and chemical synthesis routes to regulate the affecting thermodynamic or kinetics factors and successfully fabricate HEMs with single solid solution phase and homogeneous distribution of elements. The role of synthesis approach and conditions are more crucial in the formation of high-entropy nanomaterial to control the size, phase structure and composition distribution.

HEAs with single-phase crystal structure have been successfully synthesized by various physical and chemical routes. The mechanical alloying like arc melting[65–67] and high energy ball milling[68,69] are simpler processes to synthesis HEAs in a larger amount and relatively bigger particle size. Dealloying of mechanically alloyed multicomponent alloy precursor is a common method to fabricate nano-porous HEAs.[70–72] Wet-chemistry processes such as solvothermal synthesis[73], ultrasonicated-assisted wet chemistry[74], and sol-gel auto-combustion[75] are effectively used for the formation of nano-size HEAs. Other novel synthesis methods of carbothermal shock[76–78], fast-moving bed pyrolysis[79] and sputtering deposition[80,81] are reported to produce the fine size HEA NPs but in low yield of production. Different synthesis methods reported in the literature for the formation of bulk and nano-size HEAs are analysed and compared in more details by other studies.[39,82–84]

The fabrication of HEO powders is easier by conventional solid-state mixing of metal salts but requires high-temperature synthesis, which is their main disadvantages,[9,85] Lower energy demanded wet-chemistry methods such as co-precipitation[86,87], solvothermal[88], hydrothermal[87], spray pyrolysis[86,89,90], mechanochemistry[91,92], sonochemistry[93] and solution combustion[94] are reported for successful preparation of HEO NPs with different components and crystal structure.[95]

The properties of synthesized HEMs, including the crystal structure, morphologies, elemental composition, distribution, and chemical states, are assessed through different material characterization techniques. The microstructure, morphology, and size of HEMs are mainly characterized by scanning electron microscopy (SEM), transmission electron microscopy (TEM), and high-angle annular dark-field scanning transmission electron microscopy (HAADF-STEM).[96–98] The crystallography and phase structure of materials are analysed by identifying the crystallographic peaks in the X-ray diffraction (XRD) test and electron diffraction patterns in the selected area diffraction (SAD) test. Furthermore, the atomic scale HAADF-STEM and associated fast Fourier transform (FFT) analysis are advanced characterization tools to identify lattice planes, atomic lattice defects, and dislocations.[79,81] Chemical composition of HEMs is characterized by Energy-dispersive X-ray spectroscopy (EDX) on a selected area by electron microscopy and X-ray photoelectron spectroscopy (XPS) for the elemental composition peaks at near surface.[26–28] Elemental mapping illustration by EDX is one the most important tools for confirming the uniform distribution of constituent elements in all multicomponent HEMs, especially for NPs in catalysis applications.[74,76,99–101] Inductively coupled plasma-optical emission spectrometry (ICP-OES) inductively coupled plasma-mass spectroscopy (ICP-MS) are other tools for compositional analysis of bulk samples.[76,101] The XPS and X-ray absorption spectroscopy (XAS) are techniques used to determine the chemical states of the constituent elements on the surface of HEMs.[26–28]

## 5. High-Entropy Materials in Catalysis and Electrocatalysis Applications

### 5.1 Electrocatalysis in Fuel Cells

Fuel cells are one of the most promising energy conversion devices with high efficiency and low pollution that generate an electric current through an electrochemical redox reaction. Anodic oxidation of hydrogen-rich fuel and cathodic reduction of oxygen demand highly active and corrosion-resistant electrocatalysts to improve the efficiency of fuel cells.[102] HEAs have been studied as potential electrocatalysts for cathodic reduction of oxygen in different electrolyte media and for anodic oxidation of fuels in direct methanol fuel cell (DMFC), direct formic acid fuel cell (DFAFC) and direct ethanol fuel cell (DEFC).

#### 5.1.1 Methanol Oxidation Reaction (MOR)

Improving the low power density of DMFCs related to the slow rate of methanol oxidation reaction (MOR) at the anode surface is in great demand. One approach is developing highly active and cost-effective electrocatalysts. It is also essential for the catalyst materials to be corrosion resistant in the acidic electrolyte inside the cell.[102] Pt is the highly active noble metal as a catalyst for MOR, but it has limitations due to its high cost and low abundance in the Earth. The other issue with the Pt catalyst is the poisoning due to CO adsorption on its surface happening after methanol dehydrogenation, which can rapidly deactivate it.[103] Therefore, many efforts have been made to solve this problem by alloying Pt with other elements. Several binary[104–110] (PtRu, PtFe, PtCo), ternary[104,105,111] (PtRuCo, PtRuOs) and quaternary[104,105,112,113] (PtRuIrOs, PtRuNiZr) Pt-based alloys with more and fewer improvements in catalysis performance have been reported in the literature.[114] Among all of them, the binary PtRu alloys showed the highest activity due to their completely rapid oxidation mechanism.[108–110]

Taking the advantages of high-entropy multi-element alloys into consideration, Tsai *et al.*[103] developed a Pt-based HEAs catalyst for MOR. They fabricated the Pt-based multi-element $Pt_{50}Fe_{11}Co_{10}Ni_{11}Cu_{10}Ag_8$ nanoparticles (NPs) with single FCC solid solution structure by radio frequency sputter deposition method. It was found that this multi-element alloy with less amount of Pt content has higher MOR activity compared to the Pt catalyst alone. However, the performance of this alloy was still lower than that of $Pt_{43}Ru_{57}$. In another study, Tsai *et al.*[115] investigated the effect of Pt composition in the $Pt_x(FeCoNiCuAg)_{(100-x)}$ multi-element NPs on its MOR activity. Among four different compositions (x = 22, 29, 52, 56), $Pt_{52}Fe_{11}Co_{10}Ni_{11}Cu_{10}Ag_8$ showed the highest mass activity. It was again observed that the multi-element alloy has higher activity than those with the Pt alone and lower than the binary

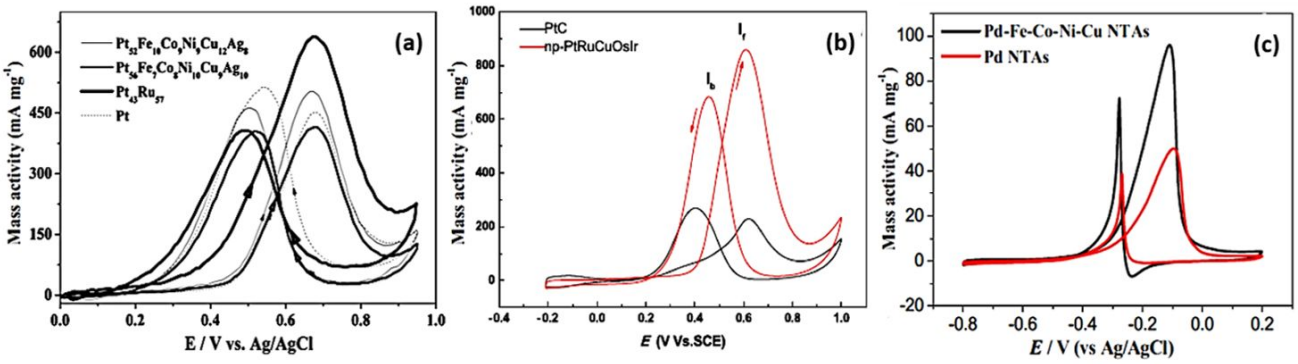


**Figure 6** - Comparison of the catalytic activity toward MOR. Cyclic voltammetry curves in mass activities of (a) $Pt_{56}Fe_7Co_8Ni_{10}Cu_9Ag_{10}$ NPs, $Pt_{52}Fe_{10}Co_9Ni_9Cu_{12}Ag_8$ NPs, Pt NPs, and $Pt_{43}Ru_{57}$ NPs (the 100th cycle) in 0.5 M $H_2SO_4$ + 1.0 M $CH_3OH$ (Reproduced with permission (ref. [115]). Copyright 2009, Elsevier.) ; (b) np-PtRuCuOsIr and PtC catalysts in 0.5 M $H_2SO_4$ + 0.5 M $CH_3OH$ (Reproduced with permission (ref. [116]). Copyright 2015, Elsevier.) ; and (c) PdNiCoCuFe NTAs and Pd in 1.0 M NaOH + 0.5 M $CH_3OH$ (Reproduced with permission (ref. [122]). Copyright 2014, Elsevier.) for methanol electrooxidation.

PtRu alloy (Figure 6a). Chen *et al.*[116] likewise compared the electrocatalytic activity of their fabricated Pt-based HEAs with that of the commercial PtC catalyst. The nano-porous PtRuCuOsIr (np-PtRuCuOsIr) was synthesized by chemical dealloying of mechanically alloyed AlCuPtRuOsIr precursor. From the electrochemical test results, a specific activity of 3 (mA $cm^{-2}$) for np-PtRuCuOsIr HEA was observed, which was six times higher than 0.5 (mA $cm^{-2}$) obtained for PtC catalyst. In a better comparison, mass activities (normalized by Pt loading) of 857.5 and 229.5 (mA $mg^{-1}$) for the np-PtRuCuOsIr and PtC, respectively, indicate that HEM nano-catalyst has about 3.7 times higher intrinsic activity towards MOR (Figure 6b). This result reflects the fact that HEAs containing Pt not only enhance the performance of DMFC but also reduce the catalyst cost due to less amount of Pt element required. Another improved performance of HEAs for methanol electrooxidation is related to its higher CO tolerance compared to commercial PtC catalyst, which makes it more ideal electrocatalyst for DMFC application.

Among all active metals, palladium (Pd) is the most similar metal to Pt, which is an attractive low-cost and more abundant option to be replaced in Pt-based catalysts.[117,118] Similar to the Pt-based alloys, alloying Pd with other active, cheap and stable transition metals can boost its activity.[119–121] Wang *et al.*[122] synthesized a quinary PdNiCoCuFe alloy nanotube arrays (NTAs) by a template-assisted electrodeposition method and compared it with Pd NTAs for their performance in methanol oxidation. It is reported that the PdNiCoCuFe alloy NTAs exhibited considerably higher electrocatalytic activity relative to Pd NTAs (Figure 6c). This enhancement in activity is attributed to the synergistic effect of multi-component systems and the electronic effects associated with alloys.

#### 5.1.2 Ethanol Oxidation Reaction (EOR)

DEFC has theoretically high energy density due to the electrooxidation of ethanol at anode which is a 12-electron/12-proton reaction with multiple dehydrogenation and oxidation steps[123]. However, designing the suitable catalyst with high selectivity for the 12-electron process to achieve the complete EOR is very challenging and in great interest. Most of the single Pd and Pt metal and their binary alloy catalysts have shown the activity only toward 4-electron transfer process.[124–126]

Wu *et al.*[127] evaluated the EOR performance of a HEA NPs catalyst composed of six platinum group metals (RuRhPdOsIrPt) compared to the synthesized and commercial monometallic catalysts. The senary HEA with FCC solid solution structure showed 2.5-30.1 times higher specific current density (normalized by electrochemically active surface area (ECSA)) compared to all monometallic catalysts (Figure 7a). More interestingly, the HEAcatalyst at 0.6 V has 1.5 times higher mass activity than the Au@PrIr/C which is the highest active catalyst reported for EOR with 12electron process[128] (Figure 7b). Comparing the CVs curves of different mono and multi element catalysts revealed that not all these metallic elements have high EOR activity, but they can improve the adsorption/desorption of intermediate species and C-C breaking on the surface of HEM catalyst. The HEM catalyst also demonstrated high stability during cycling in 1 M KOH electrolyte with ethanol and good activity retention over 50 cycles (Figure 7c). The HEAwith six elements has more ideal surface configuration with various adsorption/desorption sites for intermediate species of multistep EOR which can boost the selectivity of 12-electron process and the overall efficiency of EOR. This indicates that by more control on the effect of each element and compositional tuning, multielement HEMs are potential catalysts for many other complex reactions.

#### 5.1.3 Formic Acid Oxidation Reaction (FAOR)

The electro-oxidation of formic acid into $H_2$ and $CO_2$ is the anodic reaction of DFAFC, which can be achieved via direct or indirect competing pathways.[129] Different alloying and shape engineering strategies are applied to improve the efficiency of highly active Pt and Pd catalyst for industrial applications.[130–133] Katiyar *et al.*[134] **s**tudied the electrocatalyst performance CuAgAuPdPt HEA NPs compared to Pt NPs catalyst for the FAOR. The ratio of forward to reserve current of oxidation peaks ($i_f/i_r$) measured for HEA was 1.47 and 3.5 times higher than that of Pt NPs (0.4). Also, analysing the gas produced from the reaction catalysed by HEA NPs and Pt NPs showed that a lower amount

 

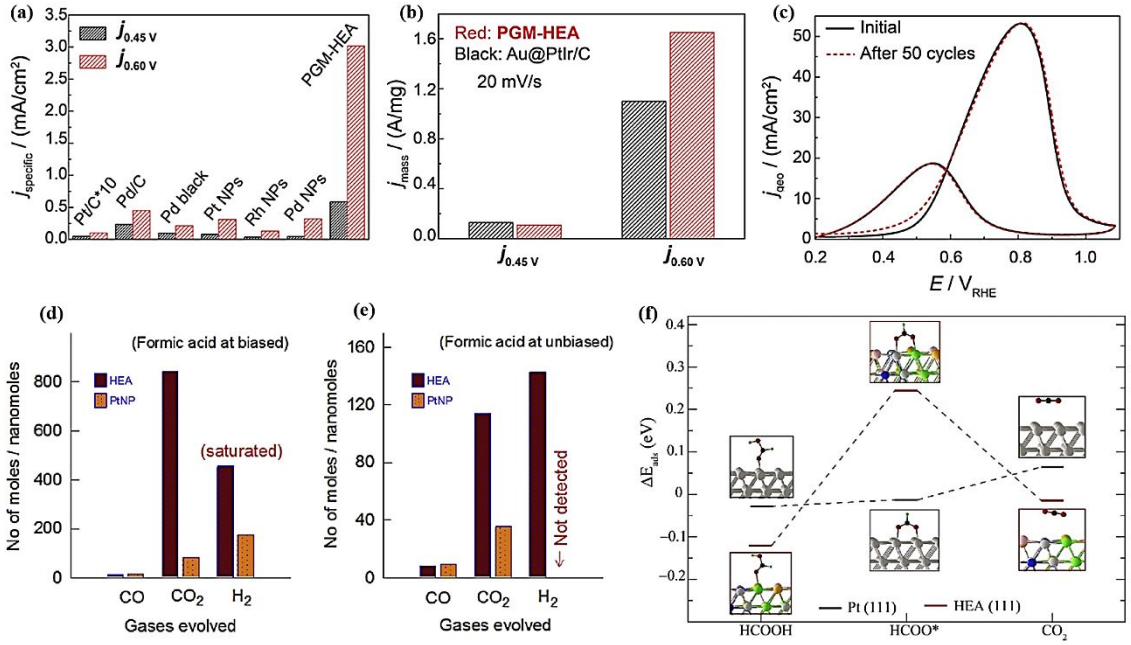


**Figure 7-** Comparison of (a) specific activities of RuRhPdOsIrPt HEA NPs (shown with PGM-HEA label) with monometallic catalyst, and (b) mass activity of HEA NPs (shown with PGM-HEA label) with Au@PtIr/C catalyst for EOR at 0.45 and 0.6 V. (c) Performance stability of RuRhPdOsIrPt NPs in EOR after 50 cycles. Reproduced with permission (ref [127]). Copyright 2020, American Chemical Society. Comparison of moles of gasses produced on CuAgAuPdPt and Pt NPs catalysts during FAOR at (d) 0.7 biased and (a) unbiased (without energy input) conditions. (f) DFT calculated adsorption energies of reactant (HCOOH), intermediate (HCOO*) and product ($CO_2$) of FAOR on the (111) surface of pristine Pt and CuAgAuPdPt (shown with HEA label) showing their mechanism of catalysis reaction. Reproduced with permission (ref [134]). Copyright 2020, Elsevier.

of CO is produced on the HEM catalyst (Figure 7d-e). These results imply the FAOR on HEA is mainly dominated by the direct oxidation pathway. To explain the experimental results, the mechanism of the FAOR is also studied by DFT calculation of the adsorption energies of reactant (HCOOH), intermediate (HCOO*) and product ($CO_2$) of the reaction on HEA and Pt (111) surfaces (Figure 7f). It was revealed that the synergistic effect of different metallic elements in HEM leads to a change in the d-band canter and adsorption energies of species on its surface compared to the pristine elements. The reaction profile shows that FAOR is exothermic on HEA and endothermic on Pt surface, which could be the reason for the higher activity of the HEM catalyst.

#### 5.1.4 Oxygen Reduction Reaction (ORR)

The oxygen reduction reaction (ORR) is the crucial cathodic reaction in fuel cells and demands a highly active electrocatalyst to overcome its overpotential and slow kinetic of either 4-electron or 2-electron pathways.[135] Among all metal elements, Pt is known as the state-of-art electrocatalyst for ORR due to its excellent catalytic activity and long-term stability in acidic and alkaline media of fuel cells.[136] However, the major limitations associated with their high cost and rareness for feasible applications in commercialized fuel cells have led to research efforts to develop alternative low Pt loading or Pt-free electrocatalysts.[137] The volcano-like plots of catalytic activities and binding energies of metals are usually used to design new electrocatalyst alloys by predicting the activity based on the constituents and their compositions. However, such prediction for a multi-component system is more complicated than the average calculated binding energies and activity of single metals.[136,137]

Loffler *et al.*[138] experimentally investigated the electrocatalytic activity of the well-known CrMnFeCoNi HEA (Cantor alloy) as a non-noble metal alloy toward ORR. The quinary HEANPs were synthesized by combinatorial co-sputtering into an ionic liquid and their electrocatalytic activity in alkaline media was compared to Pt as well as binary and quaternary alloys of the same elements. The interesting result revealed higher activity (lower overpotential) of HEANPs catalyst composed of five equimolar non-expensive transition metal elements compared to that of Pt catalyst. In contrast, the activities of all other quaternary and binary alloys were considerably lower than Pt catalyst (Figure 8a). These findings suggest that HEA, with homogenous distribution of five different metals in a single-phase solid solution, provides a higher number of active sites for electrocatalysis.

Chen *et al.* [116] evaluated the catalytic activity of np-PtRuCuOsIr HEA toward ORR at the cathode in addition to MOR at the anode, which was mentioned before (section 4.1.1). The result from the ORR electrocatalytic activity measurement test in 0.1 M $HClO_4$ solution exhibit the specific activity of 0.77 mA $cm^{-2}$ and mass-specific activity of 0.249 A $mg_{Pt}^{-1}$ for np-PtRuCuOsIr which are about 3.8 and 1.8 times higher than those of the commercial PtC, respectively (Figure 8b). The durability of the np-PtRuCuOsIr was also tested in an acidic electrolyte

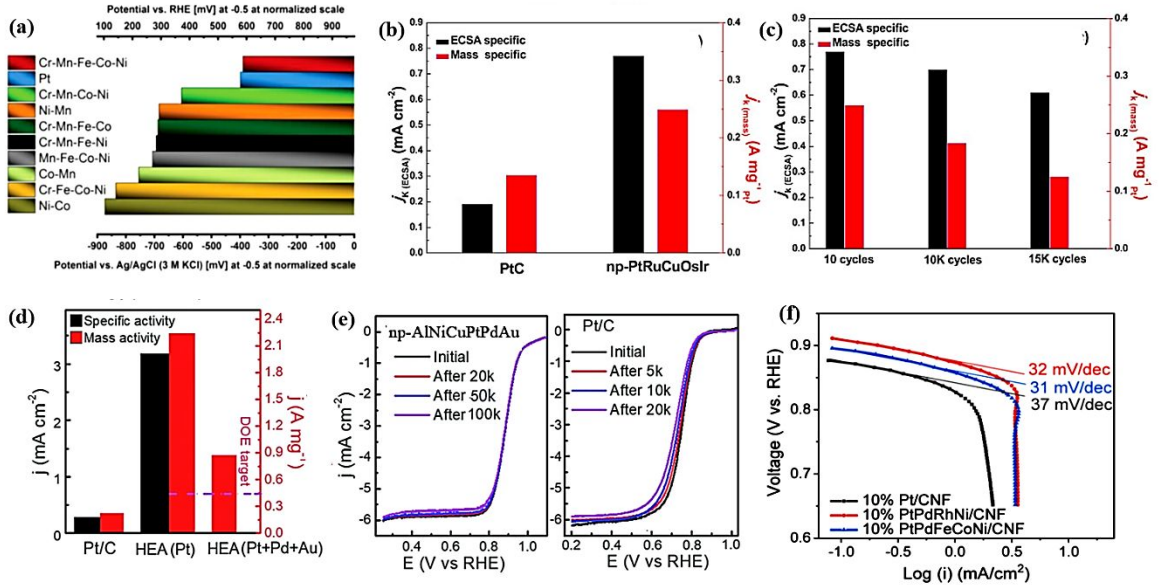


**Figure 8 -** Comparison of catalytic activities of HEAs toward the ORR. (a) Overpotential at -0.5 V at normalized scale for all sputtered NPs (Pt, binary, quaternary, and quinary Cr–Mn–Fe–Co–Ni). Reproduced with permission (ref. [138]). Copyright 2018, Wiley-VCH. The ECSA specific and mass-specific kinetic current densities at 0.90 V (vs. RHE) for (b) the np-PtRuCuOsIr and PtC catalysts; and (c) the np-PtRuCuOsIr after 10, 10K and 15K cycles. Reproduced with permission (ref. [116]). Copyright 2015, Elsevier. (d) EASA specific and Pt mass-specific activities of Pt/C and HEA; and Pt + Pd + Au mass activities of HEA at 0.9 V and (e) durability of np-AlNiCuPtPdAu and Pt/C after different cycles in $O_2$-saturated 0.1 M $HClO_4$. Reproduced with permission (ref. [139]). Copyright 2019, Royal Society of Chemistry. (f) Tafel plots of ORR activities of PtPdRhNi, PtPdFeCoNi, and Pt catalyst in 1 M KOH. Reproduced with permission (ref. [140]). Copyright 2020, National Academy of Science.

(0.1 M $HClO_4$). After 10K and 15K cycles, specific activity retention was measured as 90.3% and 73.1% of the initial value, respectively, and the corresponding mass activity retention was 70.2% and 50.0% (Figure 8c).

Qiu *et al.* [139] proposed a combined method of arc-melting followed by fast cooling and dealloying from the Al-rich precursor for preparation of equimolar senary np-AlNiCuPtPdAu HEAs. The characterization tests demonstrated that the as-prepared np-AlNiCuPtPdAu is composed of uniformly distributed six different elements in the FCC solid solution structures of nano-ligaments. Also, the surface of nano-ligaments is coated with a very thin spinal oxide layer due to the natural surface oxidation of less noble metals in the air. The fabricated np-HEA was examined for different electrocatalytic performances, including electrocatalysis ORR. It was found that specific activity and Pt mass activity of np-AlNiCuPtPdAu in an acidic electrolyte solution ($O_2$-saturated 0.1 M $HClO_4$) are 11.4 and 10 times higher than those of commercial Pt/C, respectively. Likewise, the activity of np-AlNiCuPtPdAu normalized by its total mass of precise metals (Pt, Pd, and Au) was found to be four times higher than that of Pt/C (Figure 8d). Additionally, the HEA catalyst showed durability and long-term performance stability in acidic environment after 100 000 CV cycles, while 35% loss of mass activity after 20 000 cycles was observed in Pt/C results (Figure 8e).

Yao *et al.*[140] synthesized a series of ultrafine and homogenously dispersed HEA NPs on carbon support through a fast thermal shock method to explore their vast compositional design by controlling the formulation of precursor solutions. Two quaternary (PtPdPhNi) and quinary (PtPdFeCoNi) uniformly dispersed multi-metallic nanoclusters on the carbon nanofiber (CNF) supports as optimized examples were screened for their activities for ORR in 1 M KOH electrolyte compared to control sample (Pt/CNF) by droplet cell analysis. Both HEAs loaded samples had lower overpotentials and better catalytic performances than single metal Pt loaded catalyst. The Tafel plots of three tested catalysts exhibit smaller slopes for the HEAs/CNF than that of the Pt/CNF with a similar mechanism in ORR (Figure 8f). Batchelor *et al.* [141] presented a theoretical approach to predict the electrocatalytic activity of HEAs based on DFT calculated OH and O adsorption energies on random available binding sites on the surface of IrPdPtRhRu. Furthermore, the model works for the optimization of HEA by adjusting the elemental compositions to increase the binding sites with the highest activities. According to this study, the high number of surface configurations provides the near-continuum adsorption energies on the surface of HEA and makes it an inherently protentional electrocatalyst for the ORR.

### 5.2 Electrocatalysts for Hydrogen Generation from Water Splitting

Hydrogen production by water splitting method from the different electric sources like solar photovoltaic (PV) and wind power is a simple and environment-friendly energy generation approach.[142,143] In this method, hydrogen and oxygen are generated by electrochemically splitting water molecules ($e^- + H_2O \rightarrow ½\ O_2 + H_2$) through hydrogen evolution reaction (HER) on cathodes and oxygen evolution reaction (OER) on anodes.[144] However, water splitting efficiency is mainly limited by the electrolysis overpotentials and kinetic of the HER/OER and

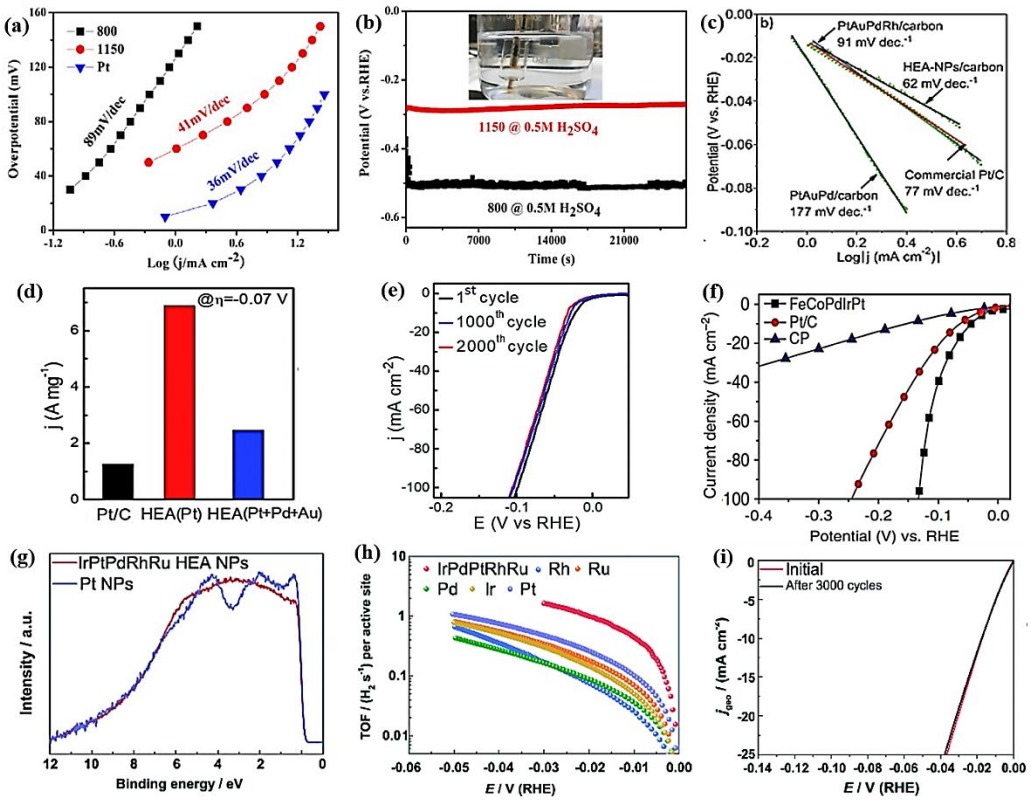


**Figure 9 -** Comparison of catalytic activity toward HER. (a) Tafel plots and (b) electrochemical stability of single-phase (@1150) and dual-phase (@800) $Ni_{20}Fe_{20}Mo_{10}Co_{35}Cr_{15}$ catalysts in 0.5M $H_2SO_4$ at room temperature. Reproduced with permission (ref. [157]). Copyright 2018, Elsevier. (c) Tafel plots of PtAuPdRhRu HEM-NPs/carbon, PtAuPdRh/carbon, PtAuPd/carbon, and commercial Pt/C (Pt loading = 20 wt.%) catalysts in 1M KOH. Reproduced with permission (ref. [158]). Copyright 2019, Wiley-VCH. (d) Pt and Pt + Pd + Au mass-specific activities at 0.07 V and (e) cycling stability of np-AlNiCuPtPdAu. Reproduced with permission (ref. [139]). Copyright 2019, Royal Society of Chemistry. (f) Linear sweep voltammetry curve of FeCoPdIrPt@GO NPs and Pt/C (ref. [159]). Comparison of (g) the valance band spectrum of IrPdPtRhRu and Pt NPs; and (h) TOF of IrPdPtRhRu NPs and monometallic NPs in 0.05 M $H_2SO_4$ ; (i) polarization curve of IrPdPtRhRu NPs at initial and after 3000 cycles. Reproduced with permission (ref. [160]). Copyright 2020, Royal Society of Chemistry.

requires highly active electrocatalysts to enhance it.[145] Pt/Ru/Ir-based catalysts are known as the best theoretically active catalysts for these reactions, yet high-cost and scarcity of the noble-metals are the critical constraints to their practical large-scale applications.[146–149] Therefore, various transition-metal-based alloys as low-cost and nature abundant catalysts with comparable catalytic performances to that of noble-metal-based catalysts were developed and studied.[69–74] However, the weak corrosion resistance and chemical stability of the materials in acidic and alkaline electrolytes are reported as the critical drawbacks for their applications.[155,156]

### 5.2.1 Hydrogen Evolution Reaction (HER)

Inspired by the emergence of the new multi-element alloys with unique structural properties, phase stability, and corrosion resistance, Zhang *et al.*[157] investigated the catalytic performance of a HEA ($Ni_{20}Fe_{20}Mo_{10}Co_{35}Cr_{15}$) for HER. In this work, the HEA samples were fabricated by an arc melting method with two different annealing temperatures of 800 °C and 1150 °C. The sample annealed at 1150 °C is a single FCC phase solid solution while the other one annealed at 800 °C shows the FCC phase plus μ phase precipitates. The results of the electrocatalytic activity of single-phase (FCC) and dual-phase (FCC+μ) samples for HER in acidic electrolytes were compared together and to that of commercial Pt catalyst .The single-phase HEA with lower onset potentials and smaller Tafel slope showed better performance than dual-phase sample (Figure 9a). Moreover, the electrochemical stability test of the HEA electrode in an acidic electrolyte (0.5M $H_2SO_4$) demonstrated that the single FCC phase HEA works without activity degradation for 8 hours and is more durable than the dual-phase HEA (Figure 9b). The superior electrocatalytic performances of the single-phase HEAs are mainly attributed to its disordered atom distribution, which provides a simple solid solution phase with higher coordination numbers. In addition to the effect of disordered surface atoms, the synergistic effect of under-layer atoms boosts the hydrogen adsorption on the electrode and facilitate the charge transfer required for HER.

Liu *et al.*[158] synthesized ternary PtAuPd, quaternary PtAuPdRh, and quinary PtAuPdRhRu alloy NPs by co-reduction of metal ions with ethylene glycol under ambient condition and tested their electrocatalytic HER performances in 1 M KOH solution. Lower Tafel slope of 62 mV $dec^{-1}$ obtained for HEA NPs compared to those of ternary (177 mV $dec^{-1}$) and quaternary (91 mV $dec^{-1}$) synthesized alloys as well as commercial Pt catalyst (77 mV $dec^{-1}$) (Figure 9c). Another HER electrocatalytic

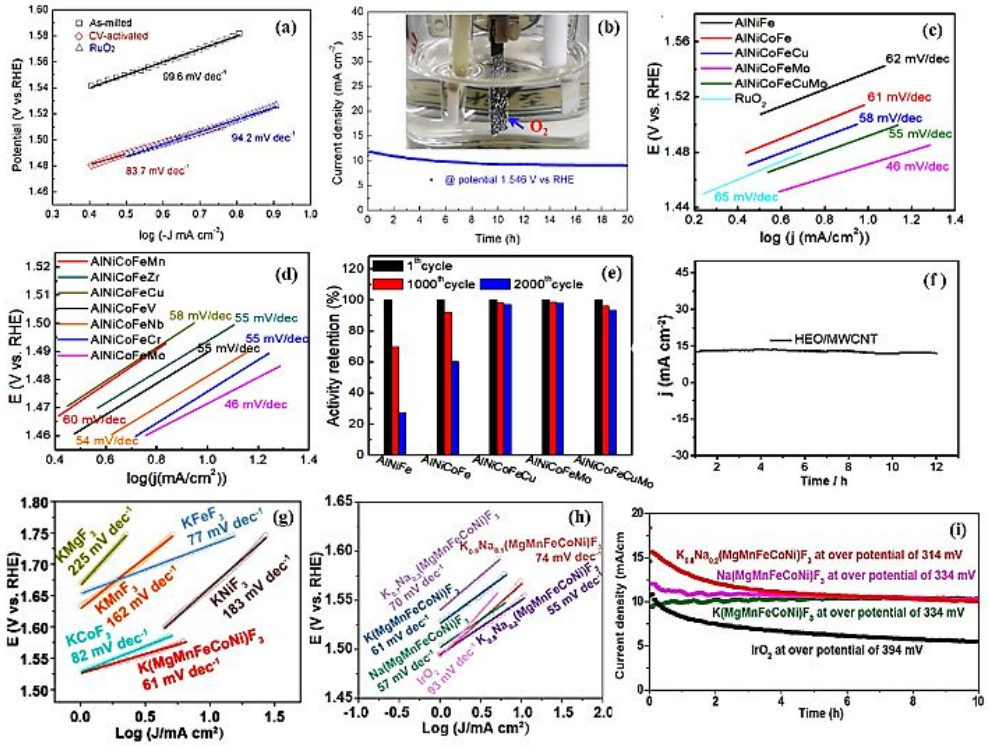


**Figure 10 -** Comparison of catalytic activity toward OER. (a) Tafel plots for $RuO_2$, as-milled and CV-activated MnFeCoNi catalyst; and (b) electrochemical stability test of CV-activated MnFeCoNi HEM working electrode in 1M KOH solution. Reproduced with permission (ref. [114]). Copyright 2018, Elsevier. Comparison of (c) Taffel plots of different metallic np-HEMs, np-AlNiCoFe, np-AlNiFe, and $RuO_2$ ; (d) Tafel plot of metallic np-HEMs different in their fifth element; and (e) activity retention at 1.55 V after 1000 and 2000 cycles of different metallic np-HEMs, np-AlNiCoFe, np-AlNiFe, and $RuO_2$. Reproduced with permission (ref. [161]). Copyright 2019, American Chemical Society. (f) Electrochemical activity retention of HEO on multiwalled carbon nanotube support (HEO/MWCNT) at 1.58V vs. RHE in 1.0 M KOH. Reproduced with permission (ref. [16]) Copyright 2019, Royal Society of Chemistry. Comparison of Taffel plots (g) perovskite fluorite HEM ($K(MgMnFeCoNi)F_3$) and other $ABF_3$ perovskite fluorite with single metal at B sites; and (h) perovskite fluorite HEMs with different composition at A site ($K_{1-x}Na_x$ $(MgMnFeCoNi)F_3$) and commercial $IrO_2$ catalyst at 1 M KOH solution. Reproduced with permission (ref [27]). Copyright 2020, American Chemical Society.

performance is reported by Qiu *et al.* [139] for their senary AlNiCuPtPdAu nano-porous HEA with ultrafine structure and high specific area. The np-AlNiCuPtPdAu exhibited higher mass-specific activity normalized by mass of Pt and mass of all the three metals (Pt, Pd and Au) compared to those of commercial Pt/C catalyst (Figure 9d). The np-HEA was also very stable in acidic electrolytes for 2000 CV cycles (Figure 9e). Gao *et al.*[159] evaluated FeCoPdIrPt@GO NPs synthesized by a fast-moving bed pyrolysis method as a working electrode for HER in 1 M KOH. This HEA electrode also demonstrated superior electrocatalyst performance than commercial Pt/C electrode with a lower overpotential of 42 mV compared to 64 mV at the current density of 10 mA $cm^{-2}$ and 26 times higher mass activity of 9.1 mA $\mu gPt^{-1}$ compared to 0.35 mA $\mu gPt^{-1}$ for Pt/C at overpotential of 100 mV (Figure 9f). Wu *et al*.[160] investigated the effect of the electronic structure of HEA NPs on the HER activity by measuring their valance band spectrum. IrPdPtPhRu NPs were synthesized through the co-reduction of the metal ions in an aqueous precursor solution sprayed into the preheated triethylen glycol as the reducing agent. The valance band spectrum of HEM and Pt NPs were experimentally measured by hard X-ray photoelectron spectroscopy (HAXPES). It was observed that unlike Pt NPs, the valance band spectra of IrPdPtRhRu HEA NPs is broad and without any sharp peaks was observed, which is because of their disorder atomic arrangements (Figure 9g). The turnover frequency (TOF) test results revealed higher intrinsic activity of IrPdPtRhRu NPs compared to the monometallic NPs (Figure 9h) and cycling CV measurement proved their excellent performance stability in an acidic electrolyte (Figure 9i).

### 5.2.2 Oxygen Evolution Reaction (OER)

Similar to the idea of using the HEA catalyst for HER, Dai *et al.* [114] reported the outstanding electrocatalytic performance of MnFeCoNi for OER comparing to highly active $RuO_2$ catalysts. The CV-activation of the HEA electrode fabricated by mechanical alloying grows nanosheets of MOx (M = Mn, Fe, Co and Ni) compounds and forms a core-shell structure with much-enhanced surface area and active sites. The obtained electrode showed comparable activity performance to that of $RuO_2$ with a low overpotential of 302 mV at the current density of 10 mA $cm^{-2}$ and the Tafel slope is only 83.7 mV $dec^{-1}$ (Figure 10a). Besides, the MnFeCoNi HEA working electrode exhibits a stable activity in 1M KOH electrolyte for 20 h (Figure 10b).

Qiu *et al.* [161] prepared different nano-porous HEAs of non-noble metals by chemical dealloying of Al-rich precursor alloys with compositions of np-AlNiCoFeX (X = Mo, Nb, Cr). They selected highly OER active NiFe and NiCoFe alloys as the starting materials and then added other elements to further increase the compositional complexity to enhance the OER performance. From the Tafel plot, an increase in the number of elements improves the activity of the catalyst and OER kinetic (Figure 10c). Furthermore, they tested the catalyst activity of quinary HEAs dissimilar in the fifth component to find the enhancing effect of different elements. This result showed that the addition of Mo, Cr and Nb has the highest to third highest catalytic enhancing effect, respectively. This is attributed to their preference for higher oxidation states, which can modify the strength of oxygen adsorption on the oxide surface (Figure 10d). Moreover, it is demonstrated that incorporating a higher number of suitable metal species into the active binary and the ternary alloy is an effective way to improve the OER catalysis as well as activity retention and durability of the catalyst over long-time cycling (Figure10e).

Wang *et al.* [16] reported the electrocatalytic activity of a HEO toward OER. They prepared the high-entropy $(CoCuFeMnNi)_3O_4$ with a single-phase spinel structure (Fd-3m) and a very small particle size of 5nm via a solvothermal synthesis followed by low-temperature pyrolysis at 400 °C. The synthesized nanoparticles loaded on multi-walled carbon nanotubes (MWCNT) revealed excellent catalytic performance for water oxidation reaction and reached a current density of 10 mA $cm^{-2}$ at 1.58 V in 1 M KOH (Figure 10f). More interestingly, the HEO supported on MWCNT showed excellent stability in the alkaline test environment for 12 h without any decay in catalytic activity, which makes it a promising catalyst candidate for OER in hydrogen generation from water splitting (Figure 10f).

A new type of HEM was developed by Wang *et al.* [27] and studied as a catalyst for OER. $ABF_3$ perovskite fluoride HEMs (HEPFs) were synthesized by combining the hydrothermal method with mechanochemistry. The catalytic activity of synthesized $K(MgMnFeCoNi)F_3$ in 1 M KOH solution was first compared with all $KMF_3$ perovskite fluorides with single metal at B site. From the electrochemical test in 1 M KOH solution, it was obtained that $K(MgMnFeCoNi)F_3$ has higher catalytic activity and kinetic for OER (operational of 369 mV at 10 $mAcm^{-2}$ and Tafel slope of 61 mV $dec^{-1}$) compared to all related $KMF_3$ perovskite fluorides with single metal at B site (Figure 10g). The superior performance of fluorite HEM is a result of their highly and randomly distributed active sites and low charge transfer resistance. Further activity improvement was observed by introducing sodium and modifying the composition of the A sites of $ABF_3$ type HEMs. Comparing the OER performances, $K_{0.8}Na_{0.2}(MgMnFeCoNi)F_3$ with a lower overpotential of 314 mV at a current density of 10 mA $cm^{-2}$ and Tafel slope of 55 mV $dec^{-1}$ exhibited the best performance among the different $K_{1-x}Na_x(MgMnFeCoNi)F_3$ HEMs as well as the commercial $IrO_2$ (Figure 10h). Also, the stability of the catalysts at the constant potential for 10 h revealed that fluorite HEM performs much better than commercial $IrO_2$ and $K_{0.8}Na_{0.2}(MgMnFeCoNi)F_3$ is able to hold the current density above 10 mA $cm^{-2}$ with lower overpotential than those of $K(MgMnFeCoNi)F_3$ and $Na(MgMnFeCoNi)F_3$ (Figure 10i).

Zhao et al. [26] developed a phosphide type of HEM and synthesized multi-elemental phosphides (HEMPs) nanosheets with Co, Cr, Fe, Mn and Ni metals in a single phosphide phase by the eutectic solvent method. The new HEMPs were evaluated as electrocatalyst for water splitting at both cathodic HER and anodic OER in alkaline media (1 M KOH solution). Commercial Pt/C and commercial $IrO_2$ were used as control samples for HER and OER, respectively. Electrochemical analysis exhibited that HEMPs with lower overpotential (Figure 11a) and Tafel slopes have higher electrocatalyst activity than those of single-metal phosphides for HER and OER (Figure 11b-c). For the

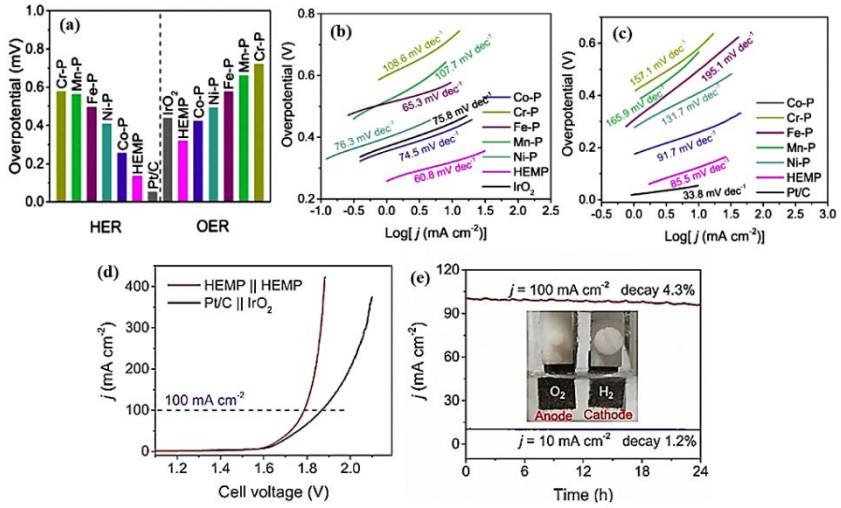


**Figure 11 -** Comparison of electrocatalytic activity toward water splitting in 1 M KOH solution. (a) overpotential of the phosphide HEM (labelled as HEMP) electrocatalyst and individual metal phosphides at a current density of 10 mA $cm^{-2}$ for HER (left) and OER (right). Tafel plots of different electrode samples for (b) OER and (c) HER. (d) Polarization curve of coupled phosphide HEM electrodes and coupled Pt/C-$IrO_2$ electrodes; (e) Chronoamperometric curves of coupled phosphide HEM cathode and anode at the current density of 10 and 100 mA $cm^{-2}$ with the inset showing the picture of the device working as the two-electrode configuration cell. Reproduced with permission (ref. [26] ). Copyright 2020, Wiley-VCH.

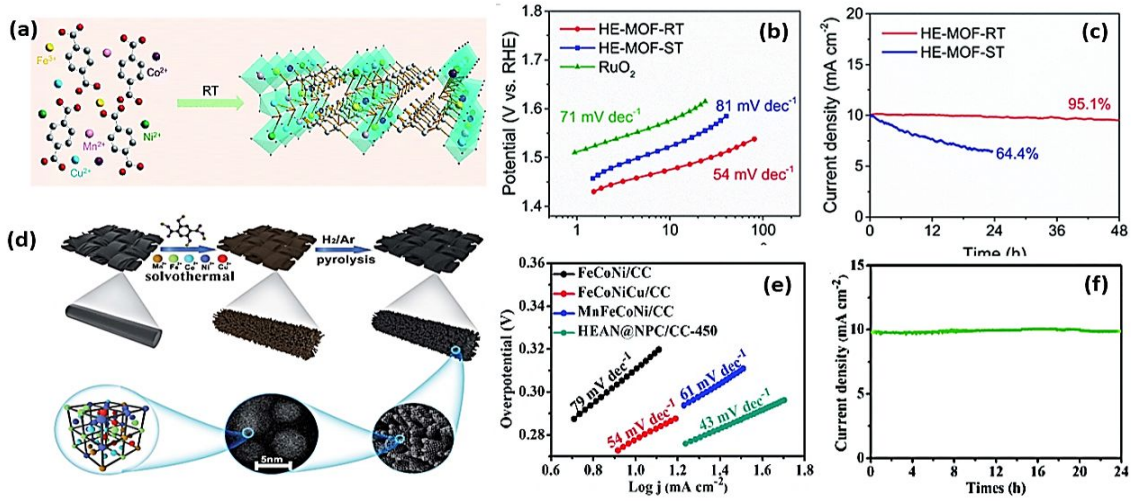


**Figure 12 -** (a) Schematic of high entropy MOF synthesized by room temperature solution method; (b)Tafel plots of HE-MOF-RT, HE-MOF-RT and $RuO_2$ electrocatalysts for OER test in $O_2$-saturated 1 M KOH electrolyte; and (c) chronoamperometric curves of HE-MOF-RT and HE-MOF-ST at a current density of 10 mA $cm^{-2}$. Reproduced with permission (ref. [30]). Copyright 2019, Royal Society of Chemistry. (d) Schematic of MOF-template synthesis of HEA NPs on carbon cloth; (e) Tafel plots of FeCoNi/CC, FeCoNiCu/CC, MnFeCoNi/CC and HEAN@NPC/CC-450 electrocatalysts for OER test in $O_2$-saturated 1 M KOH electrolyte; and (f) current density retention of (HEAN@NPC/CC-450) over time. Reproduced with permission (ref. [29]). Copyright 2020, Royal Society of Chemistry.

OER, the phosphide HEM nanosheets with an overpotential of 320 mV and a Tafel slope of 60.8 mV $dec^{-1}$ showed even better performance than commercial $IrO_2$ with the overpotential and Tafel slope of 440 mV and 75.8 mV $dec^{-1}$, respectively (Figure 11a-b). In a more practical test, the excellent electrocatalytic activity of HEMP nanosheet for the overall water splitting process was tested in a two-electrode configuration in which phosphide HEM deposited on nickel foam were used as both cathode and anode. The electrocatalytic water splitting of the cell with phosphide HEM electrodes was compared to the other one with commercial Pt/C as the cathode and commercial $IrO_2$ as an anode. The cell with phosphide HEM electrodes with a lower potential of 1.78 V at the current density of 100 mA $cm^{-2}$ exhibit superior performance than the cell with a commercial electrode coupled with the potential of 1.87 V at the same current density (Figure 11d). Additionally, the phosphide HEM catalyst performed excellent stability and current retention for 24 h and only slight current degradation of 1.2% was observed while it was run at the current density of 10 mA $cm^{-2}$ (Figure 11e).

Metal-organic frameworks (MOFs) composed of metal ions and organic group linkers with high surface area and active sites are attractive materials for catalytic and electrocatalytic reactions like OER.[162,163] Zhao *et al.*[30] reported the synthesis of high-entropy MOF(MnFeCoNiCu-MOF) from a solution of five equimolar metal ions and 1,4-benzendicarboxylic acid (1,4-BDC) at room temperature (HE-MOF-RT) (Figure 12a). Another multi-metallic MOF material was also prepared with the solvothermal method by heating the solution (HE-MOF-ST). The characterization of synthesized material showed that the room temperature method gives a homogenous and random distribution of metal ions near equimolar composition and high-entropy material is successfully formed. However, the one prepared by solvothermal method gives unequal distribution of metal ions and aggregation of Fe ions, which indicates the material is a polymetallic composite MOF and HE-MOF. The OER activity of HE-MOF was examined in the alkaline solution (1 M KOH) and compared to that of polymetallic MOF from solvothermal method as well as conventional $RuO_2$ catalyst. The obtained result revealed that the HE-MOF has lower overpotential of 245 mV at a current density of 10 mA $cm^{-2}$ and smaller Tafel slope of 54 mV $dec^{-1}$ which are much smaller than those of HE-MOF-ST (293 mV and 81mV $dec^{-1}$) and commercial $RuO_2$ (346 mV and 71 mV $dec^{-1}$) in alkaline systems (Figure 12-b). Moreover, the HE-MOF synthesized at room temperature with homogenous distribution of element showed higher activity retention compared to the one prepared by solvothermal method and aggregated elemental distribution (Figure 12c).

Huang *et al.*[29] employed a MOF templated method to synthesize sub-5 nm HEA particles on carbon cloth. The quinary metal MOF/CC precursor was pyrolyzed at 450 °C to form HEA NPs which are decorated on the porous structure by thin graphite linkers (Figure 12d). The HEA NPs with FCC crystal structure decorated on porous structure of carbon linkers were tested as electrocatalyst for OER in 1.0 M KOH and compared to ternary and quaternary NPs catalyst prepared by the same method. The result revealed that HEA NPs with Tafel slope of 43 mV $dec^{-1}$ has enhanced activity compared to other catalysts of ternary and quaternary NPs (Figure 12e). The improved OER activity and low overpotential of HEA NPs catalyst are attributed to the atomic defect in structure observed by HETEM and high surface tension associated with that. Besides the higher catalytic activity, the HEA NPs showed long term stability and good activity retention for over 24 hrs (Figure 12f).

### 5.3 Catalysts for CO Oxidation

The catalytic oxidation of CO concentrated on the surface of the catalyst is the primary key to air purification from this toxic gas.[164] Precious metals like Pt, Ru and Au are the highest active

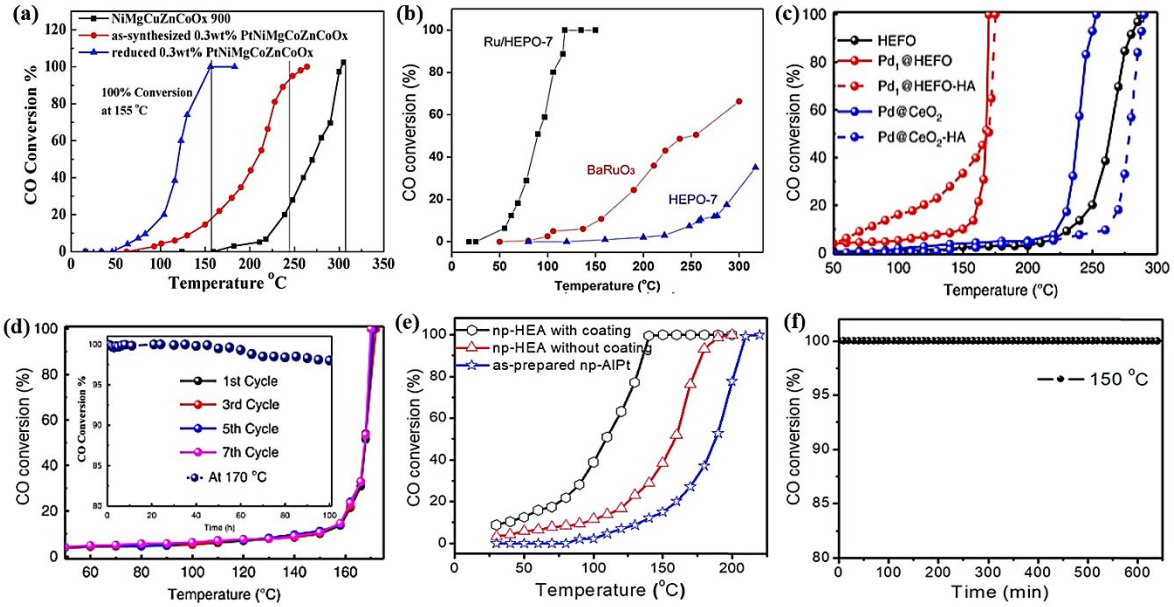


**Figure 13 -** Comparison of catalytic activity toward CO oxidation. CO conversion as a function of the reaction temperature over (a) Rock-salt HEO ($NiMgCuZnCoO_x$) and 0.3 wt.% Pt doped HEO ($PtNiMgCuZnCoO_x$). (Reproduced with permission (ref. [175]). Copyright 2018, Royal Society of Chemistry); (b) Perovskite HEO ($BaSrBi(ZrHfTiFe)O_3$ shown with HEPO-7 label), 0.2 wt.,% Ru doped HEO (Ru/HEPO-7) and $BaRuO_3$ (Reproduced with permission (ref. [177]). Copyright 2019, Wiley-VCH); (c) Fluorite HEO ($CeZrHfTiLaO_x$ shown with HEFO label), 1 wt.% Pd doped HEO ($Pd_1$@HEFO) and 1 wt.% Pd doped $CeO_2$ (Pd@$CeO_2$) (ref. [178]); (d) 1 wt.% Pd doped HEO for seven cycles (inset shows the CO conversion performance stability of catalyst at 170 °C foe 100 hrs.) (ref. [178]); and (e) np-AlNiCuPtPdAu with and without oxide coating and np-AlPt. Reproduced with permission (ref. [139]). Copyright 2019, Royal Society of Chemistry. (f) CO oxidation durability of np-AlNiCuPtPdAu with oxide coating at 150 °C. Reproduced with permission (ref. [139]). Copyright 2019, Royal Society of Chemistry.

material for this surface reaction, but their high price is an inevitable limitation for practical applications.[165,166] Oxides of transition metals like Co, Mn and Cu are also known as a suitable catalyst for CO oxidation by cause of their high oxygen content which can inhibit the rate-limiting step for the reaction and allow the active site of metals work over cycling condition.[164,167] Developing highly active, long-term functional, high-temperature stable and cost-effective catalyst or support material with the capability of good dispersion of noble metal atoms on their active sites is one attractive field of research in the catalysis area.[168–174]

The newly developed HEOs, are highly stable at high temperature due to the temperature dependence of entropic contribution to Gibbs free energy.[9] This unique property, along with the disorder multicomponent cation sites in their structure, was the inspiration to consider them as a new type of catalyst system.[175,176] Chen *et al.* [175] showed the possibility of designing a HEO-supported noble metal catalysts system for CO oxidation. The homogeneous entropy-stabilized mixed metal oxide solid solution of (NiMgCuZnCo)O not only can act as an active catalyst itself but is an excellent support to randomly disperse and stabilize Pt atoms. The 0.3 wt. % Pt/(NiMgCuZnCo)O showed high activity for CO oxidation (100% conversion at 155 °C) due to highly dispersed active sites and extreme thermal stability (900 °C) owing to the entropy-stabilized behavior inside the metal oxide (Figure 13a). Okejri *et al.* [177] similarly reported a Ru atom dispersed perovskite HEO nanoparticle catalyst for CO oxidation. The synthesized $BaSrBi(ZrHfTiFe)O_3$ (HEPO-7), Ru/$BaSrBi(ZrHfTiFe)O_3$ (Ru/HEPO-7) and $BaRuO_3$ by a sonochemical-based synthesis method were tested for CO oxidation performance at ambient pressure. It was observed that Ru/HEPO-7 with only 0.2 wt. % Ru has much higher activity than $BaRuO_3$ with 53 wt. % Ru and can reach 100% CO conversion at 118 °C (Figure 13b). The HEPO-7 without Ru did not show good catalytic activity which shows Ru metal is the main active sites of the catalyst and its high dispersion in the high-entropy phase resulted in the superior catalytic activity of Ru/HEPO-7. Xu *et al.*[178] synthesized the entropy-stabilized single-atom Pd catalyst in $(CeZrHfTiLa)O_x$ fluorite HEO support via mechanical milling with fumed silica followed by calcination at 900 °C and etching silica with NaOH. The CO conversion activity of fluorite HEO doped with 1 wt.% Pd ($Pd_1$@HEFO) was tested and compared to the activity of 1 wt.% Pd doped $CeO_2$ (Pd@$CeO_2$) synthesized with the same method. It was observed that $Pd_1$@HEFO has an onset temperature of 80 °C and 100% CO conversion temperature of 170 °C which are considerably lower than 223 °C and 253°C for Pd@$CeO_2$, respectively (Figure 13c). The cycled CO oxidation measurements and long-term stability test at 170 °C also demonstrated the excellent activity retention and high-temperature stability of Pd doped HEO catalyst (Figure 13d). Different characterization test results showed that Pd atoms are homogeneously incorporated in both surface and bulk phase of fluorite HEO with the existence of Pd — O — M (M=Ce, Zr or La) and no agglomeration. The enhanced reducibility of lattice oxygen on the surface and higher oxygen vacancies of the HEO carrier after incorporation of Pd atoms in lattice are reported as the main reasons for its superior catalytic activity.

Qiu *et al.* [139] examined the catalytic activity of the equimolar senary AlNiCuPtPdAu np-HEM with ultrafine structure and high specific area toward CO oxidation. The as-synthesized np-AlNiCuPtPdAu was coated with a very thin spinal oxide layer due to the natural surface oxidation of less noble metals in the air. Therefore, the catalytic activity of the metallic np-AlNiCuPtPdAu with oxide coating and after removing the thin oxide layer was tested and compared with that of the np-AlPt binary alloy with high Pt content in the same condition. The np-AlNiCuPtPdAu samples with removed oxide layer showed better catalytic performance compare to np-AlPt (Figure 13e) and excellent coarsening resistance at high temperature due to the slow diffusivity aspect of multi-element solid solutions. A comparison of results for all samples demonstrated that np-HEA with thin oxide coating has higher activity than two other tested samples and reaches to 100% conversation rate at a lower temperature (Figure 13c). Additionally, the catalyst stays active for a long time, with no efficiency decay at the operation temperature of 150 ℃ (Figure 13f). This is known as a favorable result in the field of catalysis that the oxide coating layer shows an enhancing effect on the catalytic activity of a metallic core catalyst in addition to proving better thermal stability at high temperatures. The high efficiency of np-HEAs with oxide coating is attributed to oxygen source on their surface resulting from $O_2$ dissociation as well as the role of the oxide layer in stabilizing ultrafine nano-ligaments as preventing them from losing active sites during the reaction time. Interestingly the oxide-coated alloy is highly active without any high-temperature activation step needed, unlike other np-Au or Pt-based alloyed coated with $Al_2O_3$ or $TiO_2$ layers.

### 5.4 Catalysts for Ammonia Decomposition

Catalytic decomposition of ammonia is a promising route for hydrogen storage applications[179,180]. The main limitation of the large-scale application is related to the cost of the ruthenium (Ru) as the conventional metal catalyst.[181–183] Researchers' efforts to find a low-cost and Earth-abundant replacement catalyst for this process found the bimetallic Co-Mo alloy as the best protentional option.[184,185] However, the existence of the large miscibility gap in the phase diagram of this binary alloy limits the range of its functional compositions.[186–189]

Recently, Xie *et al.* [76] investigated the idea of using quinary CoMoFeNiCu HEA NPs for the decomposition of ammonia and compared it with Co-Mo and conventional Ru metal catalysts. The quinary HEA NPs with five different Co/Mo composition ratios were synthesized by carbothermal shock technique and all formed single-phase solid solutions. This indicates that the addition of other metals and multi-element alloying can resolve the issue related to the miscibility gap of Co-Mo. Evaluation of the performance of HEA catalysts with various Co-Mo ratio toward catalytic $NH_3$ conversion at different temperatures demonstrates that all the HEAs have higher performances than that of bimetallic Co-Mo (Figure 14a). Among five HEA catalysts, the second Mo rich sample (HEA-$Co_{25}Mo_{45}$) with the Co/Mo ratio of 25/45 showed the highest activity (Figure 14a). Besides, comparing the reaction rate at 500 ℃ with different catalysts showed that the best HEA sample in this work is about 4 and 12 times more active than bimetallic Co-Mo and monometallic Ru catalysts, respectively (Figure 14b). Yao *et al.*[101] recently compared catalytic activity of $Ru_{0.44}Rh_{0.30}Co_{0.12}Ni_{0.14}$ NPs synthesized by the electrical Joule heating method and compared it with those of Ru and RhCoNi as control samples. Interestingly higher performance was observed for the HEA catalyst and reached 100% $NH_3$ decomposition at 470°C (Figure 14c).

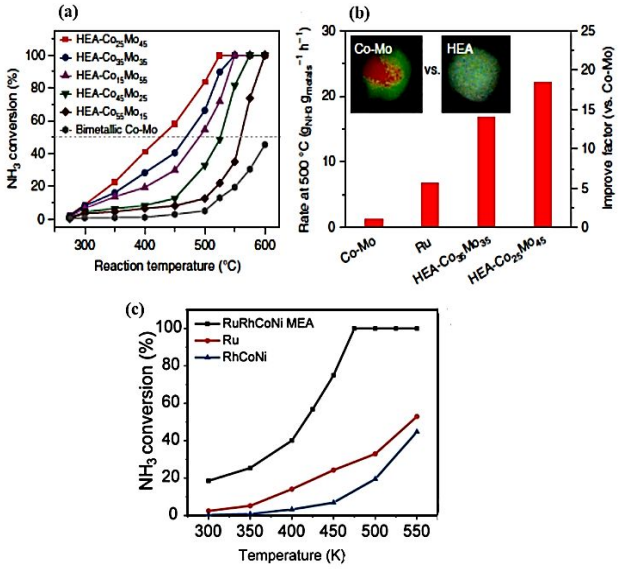


**Figure 14-** Comparison of catalytic activity toward $NH_3$ decomposition. (a) $NH_3$ conversion of different HEA-$Co_xMo_y$ nanoparticles and bimetallic Co-Mo (Co/Mo = 25/45) depending on the reaction temperature; (b) reaction rate of bimetallic Co-Mo, Ru, and HEA-$Co_xMo_y$ catalysts (T =500 °C). Reproduced with permission (ref. [76]), Copyright 2019, Springer Nature; (c) $NH_3$ conversion of RuRhCoNi compared to Ru and RhCoNi. Reproduced with permission (ref. [101]). Copyright 2020, American Association for the Advancement of Science.

### 5.5 Catalysts for $CO_2$ conversion

$CO_2$ reduction to CO by $H_2$ through a heterogeneous catalytic reaction is one of the promising ways for atmospheric $CO_2$ utilization. Chen *et al.* [176] presented a new method of synthesizing the HEO-supported noble metal catalyst at ambient temperature (Figure 15a). The advantages of this catalyst system are reducing the amount of precious metal used as well as decreasing the activation temperature of the catalyst. The mechanochemically synthesized (NiMgCuZnCo)O doped with 5 wt.% Pt showed high $CO_2$ conversion, CO yield and selectivity as well as stable performance during the 20 h (Figure 15b). Pedersen *et al.* [190] recently conducted a DFT analysis to study the catalytic activity of HEAs for CO and $CO_2$ reduction by predicting the CO and H adsorption energies on the surface of two CoCuGaNiZn and AgAuCuPdPt as examples. Using this method showed how the distribution of adsorption energies is affected by tuning the composition with different affinity for $H_2$ formation and CO reduction, which provides a way to predict and optimize the compositional distribution of HEAs to improve the catalytic activity of them towards different reactions.

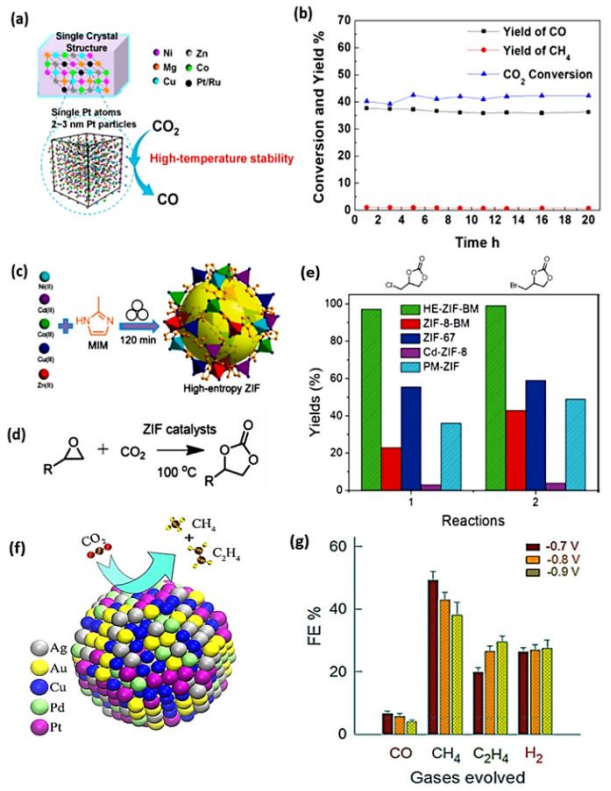


**Figure 15 –** (a) Schematic of Pt/Ru-(NiMgCuZnCo)O entropy-stabilized metal oxide solid solution synthesized by mechanical ball milling; and (b) $CO_2$ hydrogenation stability of 5 wt. % Pt doped HEO at 500°C for 20 h. Reproduced with permission (ref. [176]). Copyright 2019, American Chemical Society. Schematic of (c) ZIF HEM synthesized by mechanochemistry method; (d) catalytic cycloaddition of $CO_2$ with epoxides to produce cyclic carbonates; and (e) Yields of two cyclic carbonates obtained from the cycloaddition of $CO_2$ with corresponding epoxides catalysed by HE-ZIF-BM, ZIF-8-BM, ZIF-67, Cd-ZIF-8, and PM-ZIF. Reproduced with permission (ref. [191]). Copyright 2019, Wiley-VCH. (f) Schematic of $CO_2$ conversion to hydrocarbon fuels on Cu-based HEA catalyst; and (g) bar diagram for the faradic efficiencies of carbonaceous species and hydrogen gaseous products of the reaction. Reproduced with permission (ref. [192] ). Copyright 2020, American Chemical Society.

Xu *et al.* [191] reported the synthesis of a zeolitic imidazolate framework HEM (HE-ZIF) at room-temperature by mechanochemistry method. HE-ZIF is composed of five transition metal cations of $Zn^{2+}$, $Co^{2+}$, $Cd^{2+}$, $Ni^{2+}$, and $Cu^{2+}$ dispersed in the ZIF structure (Figure 15c). The catalytic performance of HE-ZIF for $CO_2$ cycloaddition with epoxides to produce cyclic carbonates (Figure 15d) was examined under 10 bar $CO_2$ pressure at 100 °C for 8 h and compared with other reported active single-metal ZIF-type catalysts. The reaction yields catalyzed by the HE-ZIF (97.2% for 2-(chloromethyl) oxirane, and 99.0% for 2-(bromomethyl)oxirane were interestingly higher than other single-atom ZIF catalysts due to the synergistic effect of the five metal ions as Lewis acid in epoxide activation (Figure 15e).

Another important process related to $CO_2$ conversion, is electroreduction of $CO_2$ into hydrocarbon fuels. While many noble metal catalysts like Ag, Au, Pd and Pt have shown high selectivity for CO in catalytic reduction of $CO_2$, Cu-based catalyst have shown selectivity towards other hydrocarbons. Nellaiappan *et al.*[192] have studied the electroreduction of $CO_2$ to gaseous hydrocarbon by Cu-based HEA catalyst (Figure 15f) AgAuCuPdPT HEA was synthesized by melting and cryo-milling with single FCC crustal structure and homogenous distribution of elements. The HEA is considered as a single atom catalyst when Cu is the active metal catalyst and other metals have synergistic effect on Cu catalytic activity. Electroreduction of $CO_2$ is tested in $CO_2$-saturated $K_2SO_4$ electrolyte solution with HEA as working and Pt as the counter electrode. Evaluation of gashouse product by gas chromatography has shown 100% faradic efficiency of gashouse product and higher selectivity to hydrocarbon fuels of $CH_4$ and $C_2H_4$ compared to CO and $H_2$ at a low applied potential of 0.9 V vs. Ag/AgCl (0.3 V RHE)(Figure 15g).

### 5.6 Catalysis for Azo Dye Degradation

Azo dyes, organic compounds with R−N=N−R functional group, are widely used in many industries such as textiles, cosmetics, and food. The release of the stable dyestuff existing in the effluent of these industries is known as pollution to environment.[193] Therefore, many efforts have been made to investigate an efficient approach for the degradation of azo dyes.[194–200] Degradation by zero-valent metals is one of the low-cost and simple methods generally used in industrial application.[201–204] The main limitation of this method is the low corrosion resistant of zero-valent metals in water, which can rapidly decay their efficiency.[205] Metallic glasses are other investigated material with thermodynamically stable structure and good capability for azo degradation.[206–208] However, the synthesis of metallic glasses requires several conditions and processes, which makes it not cost-effective and favorable for commercial applications.[209] Herein, there is a need to find and develop new highly stable and low-cost materials with simple preparation methods for the degradation processes of different azo dyes.

In this regard and after reported progress in high-entropy alloys and their outstanding features, Lv *et al.* [209] worked on the HEA for azo degradation. They synthesized three HEAs samples of AlCoCrTiZn ($S_1$), AlCoCrFeNi ($S_2$), and CoCrFeMnNi ($S_3$) by the mechanical alloying method and tested their performances in the degradation of Direct Blue 6 ($DB_6$, $C_{32}H_{20}N_6S_4O_{14}Na_4$). The degradation efficiency was evaluated by plotting the normalized intensity of the $DB_6$ concentration at 25 °C as a function of reaction time (Figure 16a). Based on the comparison between three HEA samples tested in this work, $S_1$ has a higher efficiency in the degradation of $DB_6$ than those of $S_2$ and $S_3$. Furthermore, the performances of the $S_1$ and metallic glasses powders were compared simply by the value $t_0$, which is the time that concentration intensity decreases to the initial condition (Figure 16b). The obtained result indicates that AlCoCrTiZn powders with $t_0$ = 0.83 min has very low efficiency to that of the best reported metallic glasses (BM MgZn glassy powder) with $t_0$ = 0.78 min. It can also be seen that the efficiency of $S_1$ is about 20 times higher than the BM Fe-based glassy powder (BM G-Fe, $t_0$ = 16 min), which is reported to be

200 times faster than that of the commonly used commercial Fe powder. The outstanding performance of HEA is attributed to its unique atomic structure with high lattice distortion, specific chemical compositions, and large available surface area. Later, Wu *et al.*[210] investigated the effect of the composition and particle size of the HEA on their efficiency toward the decolorization of DB6. To select suitable elements for HEA with high efficacity, they chose Al, Cr, Fe, Mn, Ti, Zn and Co metal elements with high activity. Among them, the elements with BCC structure are more favorable as the BCC phase is more brittle, and finer powders can be synthesized by the ball milling method. In this regard, they selected AlCrFeMn as their main sample and AlCrFeMnM (M = Mg, Ti, Ni) samples to find the effect of adding different fifth element. Comparing the normalized concentration of dye as a function of temperature for the four synthesized HEA samples showed that the addition of Ti and Mg to the AlCrFeMn can improve the efficiency and AlCrFeMnMg has the best performance among all samples (Figure 16c). Moreover, the evaluation of the $t_0$ of the highly active samples with the previous works exhibits that their performances are considerably higher than those of metallic glasses powders (Figure 16d).

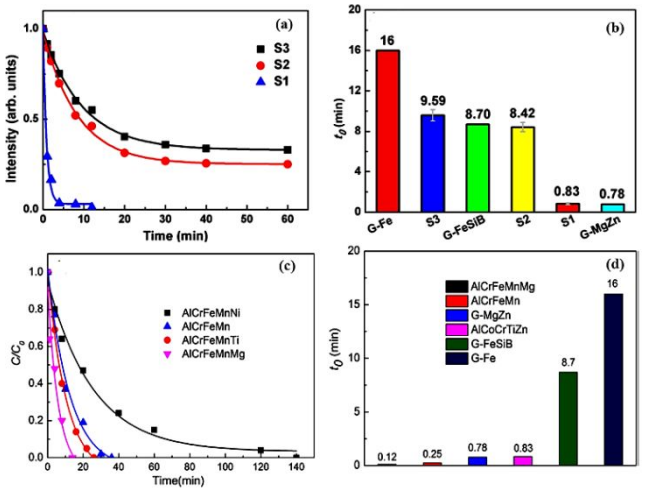


**Figure 16 -** Comparison of catalytic activity toward Azo dye degradation. Comparison of $DB_6$ degradation efficiency at 25 °C of (a) S3, S2 and S1 by the normalized concentration as a function of degrading time; and (b) S1, S2, S3, MgZn and Fe-based glassy powders by $t_0$ value. Reproduced with permission (ref. [209]). Copyright 2019, Springer Nature. Comparison of the discoloration efficiency of (c) AlCrFeMn and AlCrFeMnM (M = Mg, Ti, Ni) by concentration change over time; and (d) AlCrFeMn, AlCrFeMnMg and BMG-MgZn, AlCoCrTiZn, G-FeSiB and BM G-Fe by $t_0$ value. Reproduced with permission (ref. [210]). Copyright 2019, Elsevier.

### 5.7 Catalysts for Carbon Nanotubes Growth

There are various methods for the growth of carbon nanotubes (CNTs) and catalytic pyrolysis is one simple and efficient of these routes. Lal and Sundara[211] showed that HEO NPs themselves could efficiently play a catalytic role in the growth of CNTs to form the HEO–CNT nanocomposite. The as-synthesized HEO (Ni, Fe, Co, Cr, and Al-based) NPs from a simple sol-gel auto combustion technique were used as a catalyst for the CVD growth of multiwalled CNTs with acetylene gas as the carbon precursor. The yield of as-grown CNTs in the form of HEO–CNT nanocomposite. and reduced HEO–CNTs (by passing $H_2$ to reduce surface oxygen) was exceptionally high compared to the previous reports.

**Table 1-** List of all high-entropy materials used as catalysts in different catalysis processes

| High-Entropy Material Catalyst | Catalysis Reaction | Synthesis Method | Ref |
|---|---|---|---|
| $Pt_{50}Fe_{11}Co_{10}Ni_{11}Cu_{10}Ag_8$ NPs | MOR | Radio frequency sputter deposition method | 103 |
| PdNiCoCuFe NTAs | MOR | Template assisted electrodeposition method | 122 |
| np-PtRuCuOsIr | MOR<br>ORR | Chemical dealloying of AlCuPtRuOsIr precursor | 116 |
| np-AlNiCuPtPdAu | ORR, HER, CO Oxidation | Chemical dealloying of Al-rich precursor | 139 |
| np-AlNiCoFeX (X = Cu, Cr, Mn, Mo, Nb, Zr, V) | OER | Chemical dealloying of Al-rich precursor | 161 |
| CuAgAuPdPt NPs | FAOR, MOR | Arc melting + cryo-milling | 88 |
| RuRhPdOsIrPt NPs | EOR | Co-reduction of metal ions with triethylene glycol | 212 |
| PtAuPdRhRu NPs | HER | Co-reduction of metal ions with ethylene glycol | 158 |
| IrPdPtRhRu NPs | HER | Co-reduction of metal ions with triethylene glycol | 114 |
| CrMnFeCoNi NPs | ORR | Co-sputtering into an ionic liquid | 138 |
| $Ni_{20}Fe_{20}Mo_{10}Co_{35}Cr_{15}$ | HER | Arc melting method | 157 |
| MnFeCoNi nanosheets | OER | Mechanical alloying | 114 |

| | | | |
|---|---|---|---|
| PtPdRhNi/CNF NPs<br>PtPdFeCoNi/CNF NPs | ORR | Carbothermal shock method | 213 |
| FeCoPdIrPt@GO NPs | HER | Fast-moving bed pyrolysis method | 159 |
| CoMoFeNiCu ($HEACo_{25}Mo_{45}$) | Ammonia Decomposition | Carbothermal shock method | 76 |
| $Ru_{0.44}Rh_{0.30}Co_{0.12}Ni_{0.14}$ | Ammonia Decomposition | Electrical Joule heating method | 214 |
| IrPdPtRhRu | ORR | DFT analysis | 141 |
| CoCuGaNiZn | $CO_2$ reduction | DFT analysis | 190 |
| AgAuCuPdPt | $CO_2$ reduction | Melting and cryo-milling | 192 |
| AlCoCrFeNi<br>AlCoCrTiZn<br>CoCrFeMnNi | Azo dye degradation | Ball milling | 209 |
| AlCrFeMnM<br>(M = Mg, Ti, Ni) | Azo dye degradation | Ball milling | 210 |
| $(CoCuFeMnNi)_3O_4$ NPs/ MWCNT | OER | Solvothermal method | 16 |
| Pt doped (NiMgCuZnCo)O | CO oxidation, $CO_2$ reduction | Ball milling | 175 |
| Ru doped $BaSrBi(ZrHfTiFe)O_3$ | CO oxidation | Sono-Chemical method | 176 |
| Pd doped $(CeZrHfTiLa)O_x$ | CO oxidation | Ball milling in fumed silica template | 178 |
| Ni, Fe, Co, Cr, and Al-based oxide NPs | CNT growth | Sol-gel auto-combustion method | 211 |
| $K_{1-x}Na_x(MgMnFeCoNi)F_3$ | OER | Hydrothermal method combined with mechanochemistry | 27 |
| CoCrFeMnNi - P | HER, OER | Eutectic solvent method | 26 |
| NiCdCoCuZn-ZIF | $CO_2$ conversion to carbonate | Mechanochemistry method | 145 |
| MnFeCoNiCu-MOF | OER | Room temperature wet chemistry | 30 |

## 6. High-Entropy Materials in Electrochemical Energy Storage Application

Following the pioneering work on the development of the first HEO[9], Bérardan *et al.* [85,215,216] studied the electrochemical properties of this material. It was first reported that (CoCuMgNiZn)O substituted with aliovalent dopants (e.g., $Li^+$, $Na^+$, $K^+$) show colossal dielectric constants and the charge compensation mechanism of aliovalent dopants incorporation into a single-phase rock salt structure of HEO was discussed.[85,215] However, the most promising properties of HEOs, which makes them a new potential material for lithium-based batteries, is their superior Li-ion conductivity at room temperature. [149] This group showed that the 30% Li-doped

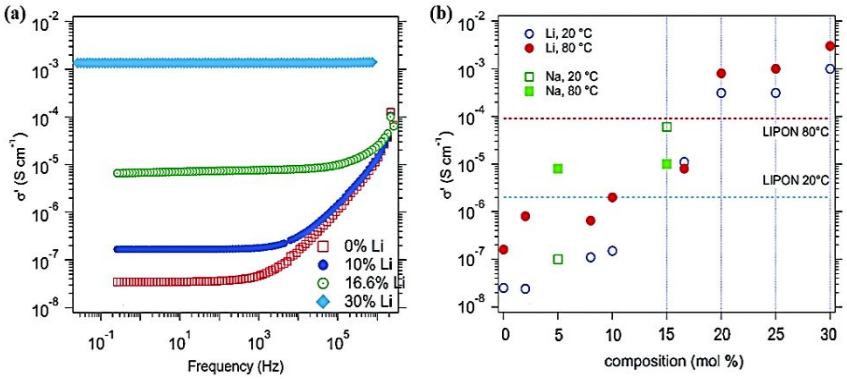


**Figure 15 -** Ionic conductivity of a) Li doped (CoCuMgNiZn)O samples at room temperature b) Li and Na doped (CoCuMgNiZn)O samples compared with LIPON. Reproduced with permission (ref. [149]). Copyright 2016, Royal Society of Chemistry.

(CoCuMgNiZn)O has ion conductivity of $10^{-3}$ S $cm^{-1}$, which is five orders of magnitude higher than that of pristine HEO ($10^{-8}$ S $cm^{-1}$) (Figure 17a). This indicates that by incorporating enough ions into the HEO structure, they can show higher conductivity than that of LIPON at room temperature (Figure 17b). These findings have inspired many recent studies on the performance of the high-entropy materials in electrochemical energy storage devices.

### 6.1 HEO as Anode Material in Li-ion Battery

Transition metal oxides (TMs) as active anode material have been widely studied for new lithium-ion batteries due to their larger theoretical capacities than that of conventional graphite anodes.[217–220] However, their solid structures change severely after cycling and result in rapid capacity decay and limit their applications for long-term stable and efficient batteries. The development of entropy stabilized metal oxides with their excellent Li-ion conductivity received attention recently to be used as the conversion anode material in Li-ion batteries.[221–223] Sarkar *et al.*[221] tested (CoCuMgNiZn)O with rock-salt crystal structure as conversion-based electrode material in half coin cell with lithium metal and showed that it can be cycled over 500 times without capacity fading (Figure 18b). The increase in capacity over cycling is the typical electrochemical behavior of conversion-based electrodes and is related to the activation process of large particles of the material. Moreover, they showed the importance of the entropy-stabilized concept on the material performance and cell cycling by testing each 4-cation oxides (medium entropy oxides) in the same system (Figure 18c). The rapid capacity degradation of cells with medium entropy oxides indicates that the high configurational entropy (1.61 R) of five-cation system is the main factor for stable structure of electrode material and its cycling stability. Preservation of rock-salt structure over cycling and during lithiation/de-lithiation processes was observed experimentally and is described as the main reason for the cycling stability of the material. It is explained that while some of the cations in the lattice are involved in conversion reaction and are reduced to metals; the other uninvolved non-reduced cations are responsible to hold the structure and trap the reduced metals inside the lattice (Figure 18d).

In other relevant work, (CoCuMgNiZn)O NPs were investigated by Qiu *et al.* [223] as anode material in coin cell and compared with $Co_3O_4$ anode as reference material. Interestingly, the HEO with a high reversible capacity of 920 $mAhg^{-1}$ at 100 $mAg^{-1}$ after 300 cycles performed better than the $Co_3O_4$ with a lower specific capacity and only 79% capacity reception. (Figure 18e-f). The difference in the performance and

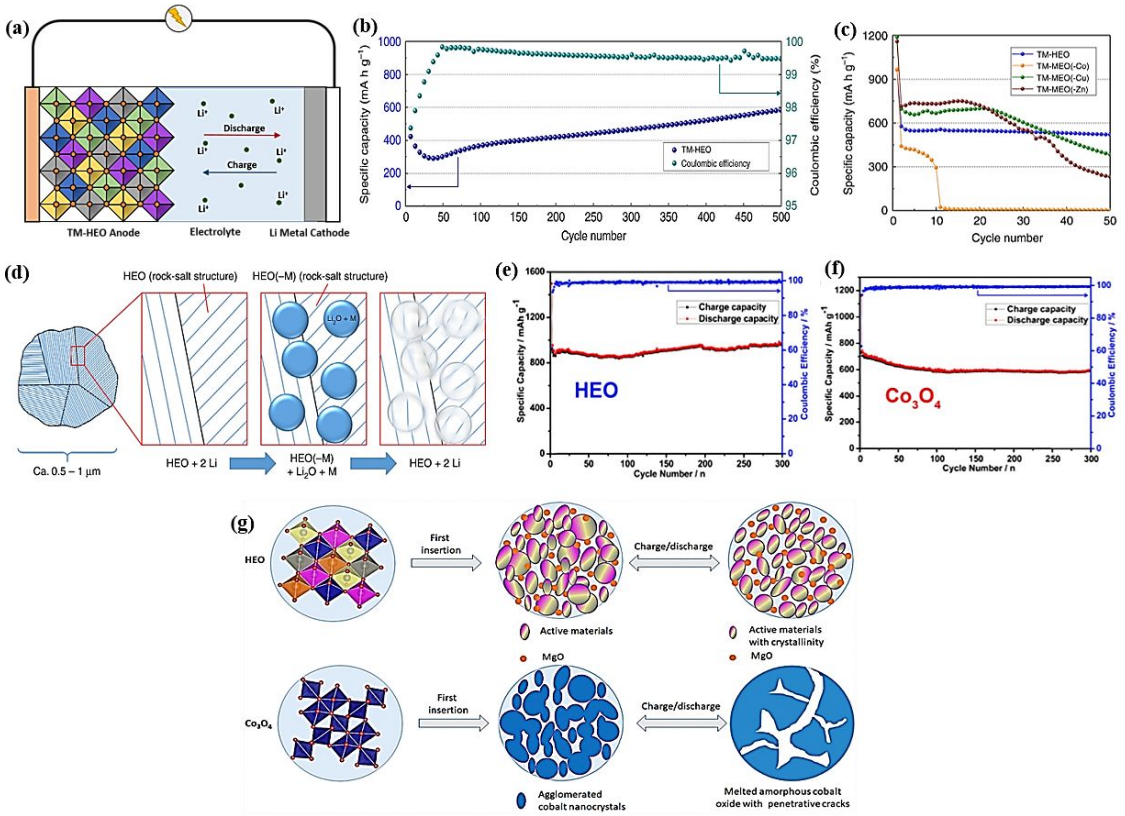


**Figure 18 -** (a) Schematic of Li-ion half-cell with TM-based HEO at anode. Cycling performance of (b) the calcined HEO at 200 mA $g^{-1}$ with the corresponding Coulombic efficiency; and (c) HEO with five metallic element (labelled as TM-HEO) and other mixed metal oxide with four metallic element (labelled as TM-MEO). Reproduced with permission (ref. [221]). Copyright 2018, Springer Nature. (d) Schematics of the (de)lithiation mechanism of active cations (Co,Cu,Zn and Ni) inside the (CoCuMgNiZn)O with poly/nanocrystalline structure during the conversion reaction. Reproduced with permission (ref. [221]). Copyright 2018, Springer Nature. Cycling performance and the corresponding Coulombic efficiency of the (e) HEO electrode and (f) $Co_3O_4$ electrode at 100 mA $g^{-1}$ during 300 cycles. Reproduced with permission (ref. [223]). Copyright 2019, Elsevier. (f) Schematic of HEO and $Co_3O_4$ electrode changes over cycling. Reproduced with permission (ref. [223]). Copyright 2019, Elsevier.

mechanism was analyzed by studying the surface morphology and crystal structure of anode material nanoparticles. A significant change in morphology and large cracks were detected on the surface of $Co_3O_4$ after several cycling, which is attributed to the agglomeration of nanoparticles and change in the overall crystallinity of the material. In contrast, no significant structural change was detected on the surface of HEO after repeated cycling (Figure 18g). It is proposed that the presence of inactive MgO along with the lattice distortion and entropy-stabilization features of the HEO prevent the particle agglomeration and morphology change and lead to long cycling performance of the anode material.

Testing the electrode material in half-cells with a Li counter electrode provides excess available Li, while in the full-cell configuration, the limited Li content of the cathode material is responsible for supplying Li for reactions[224]. Herein, Wang *et al.* [222] evaluated the performance of HEO as anode material in a full-cell with $LiNi_{1/3}Co_{1/3}Mn_{1/3}O_2$ as the cathode material (Figure 19a). The cell started working with the initial capacity of 446 $mAhg^{-1}$ and maintained at 300 $mAhg^{-1}$ after 50 cycles (Figure 19b).

The outstanding performance of transition-metal-based HEO with rock salt structure compared to conventional transition metal oxide as anode material has inspired the researchers to study and develop other types of HEO for battery electrodes. Chen *et al.* [225] studied spinel HEO of $(Mg_{0.2}Ti_{0.2}Zn_{0.2}Cu_{0.2}Fe_{0.2})_3O_4$ synthesized by solid-state reaction as anode material in a half cell LIB and observed superior Li storage and electrochemical performances. The high reversible specific capacity of 504 mA h $g^{-1}$ at a current density of 100 mA $g^{-1}$ after 300 cycles as well as exceptional 96.2% capacity retention (about 272 mA h $g^{-1}$) at the high current density of 2000 mA $g^{-1}$ after 800 cycles was achieved (Figure 19c). The remarkable electrochemical performance and stability of the electrode material are ascribed to the fast reaction kinetic, capacitive behavior and structural stability of high-entropy spinel oxide.

Yan *et al.* [226] explored a different HEO with perovskite structure as anode material for lithium-ion batteries (Figure 19d). The high-entropy perovskite titanate in the form of $[(Bi, Na)_{0.2}(La, Li)_{0.2}(Ce, K)_{0.2}Ca_{0.2}Sr_{0.2}]TiO_3$ was synthesized by the solid-state method and its performance as anode for LIBs was explored in a coin cell. The initial discharge capacity of 125.9

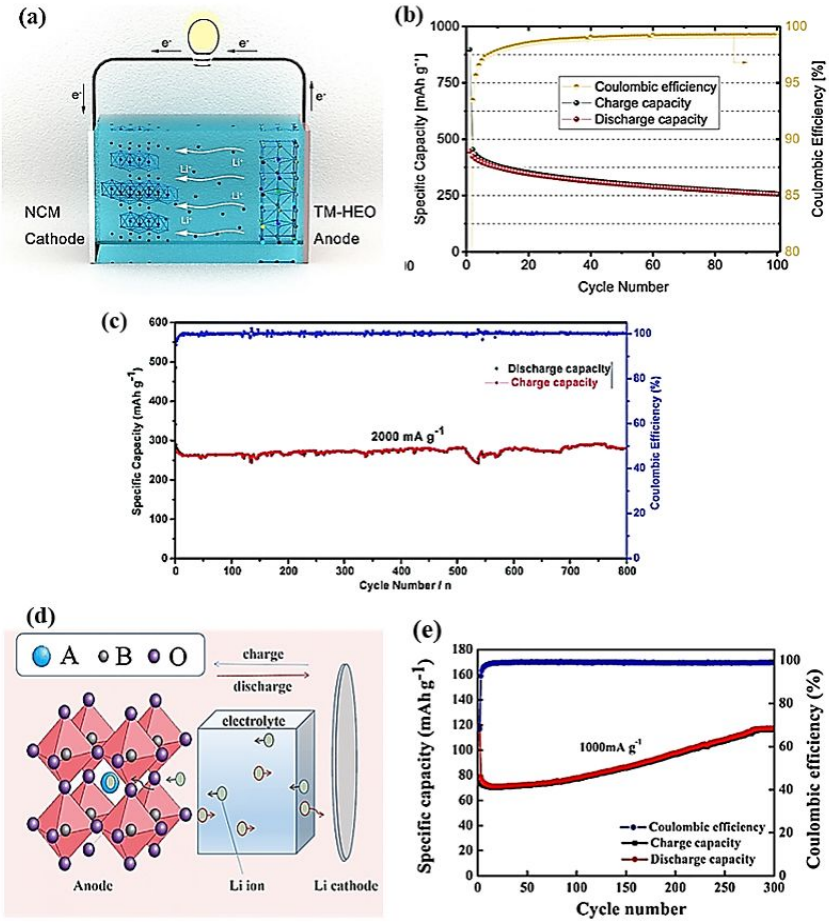


**Figure 19 -** (a) Schematic of the NCM111//TM-HEO full-cell with the intercalation-based cathode and conversion-based anode; and cycling performance and the corresponding Coulombic efficacy of (d) the NCM111//TM-HEO full-cell at 120 mA $g^{-1}$ for 100 cycles. Reproduced with permission (ref. [222]). Copyright 2019, Elsevier. (c) Cycling performance of $(Mg_{0.2}Ti_{0.2}Zn_{0.2}Cu_{0.2}Fe_{0.2})_3O_4$ electrode at 2000 mA $g^{-1}$ for 800 cycles. Reproduced with permission (ref. [225]). Copyright 2020, Royal Society of Chemistry. (d) Cycling performance of $[(Bi, Na)_{0.2}(La, Li)_{0.2}(Ce, K)_{0.2}Ca_{0.2}Sr_{0.2}]TiO_3$ electrode at 1000 mA $g^{-1}$ for 300 cycles; and (e) the schematic of the Li-ion half-cell with perovskite HEO anode. Reproduced with permission (ref. [226]). Copyright 2020, Springer Science Business Media.

$mAhg^{-1}$ and reversible capacity of 120.4 $mAhg^{-1}$ at 100 $mAg^{-1}$ with no degradation after 300 cycles was obtained (Figure 19e). The excellent cycling performance of the anode material is again attributed to an entropy-stabilized structure.

### 6.2 HEO as Cathode Material in Li/Na-ion Battery

Most of the reported works on HEOs are based on a multi-cations system with only oxygen in the anion sites. Therefore, the total stabilizing configurational entropy of material comes from the cations. Wang *et al.* [227] reported the development of the multi-anionic and multi-cationic system in that both cations and anions contribute to the total $S_{config,}$ which results in a system with higher stabilizing entropy. In this new material, additional halide (F, Cl) and alkali metal ions ($Li^+$, $Na^+$) were added to the multi-cationic transition-metal-based HEO (CoCuMgNiZnO) to make the multi-anionic and multi-cationic rock-salt type ionic crystal in the form of Li(HEO)F and Na(HEO)Cl. The synthesized oxyfluoride Li(HEO)F were used as active cathode material in a half cell Li-ion battery and showed specific capacity retention over 300 cycles. Besides, using these high-entropy materials as cathode material enables us to achieve a higher and more stable specific capacity comparing to conventional LiNiOF materials (Figure 20a).

Zhao *et al.*[228] applied the concept of high-entropy strategy to design layered oxide cathodes for Na-ion batteries. They used the HEO with nine components as a new $O_3$-type $NaNi_{0.12}Cu_{0.12}Mg_{0.12}Fe_{0.15}Co_{0.15}Mn_{0.1}Ti_{0.1}Sn_{0.1}Sb_{0.04}O_2$ as Na-ion layered cathodes, and it demonstrated long cycling stability after 500 cycles with the outstanding capacity retention (83% at 3.0 C) (Figure 20b). Moreover, monitoring the transition between $O_3$ and $P_3$ phases during charge-discharge and Na+ (de)intercalation process demonstrated that the phase transition is highly reversible. More notably, more than 60% of the total capacity being stored in the $O_3$-type region in contrast with other $O_3$-type Na-ion cathodes. The presence of multiple transition-metal components in the layered HEO to hold the structure during the Na+ (de)intercalation is presented as the possible mechanism for such a reversible phase transition and long cycling life of the cathode material (Figure 20c).

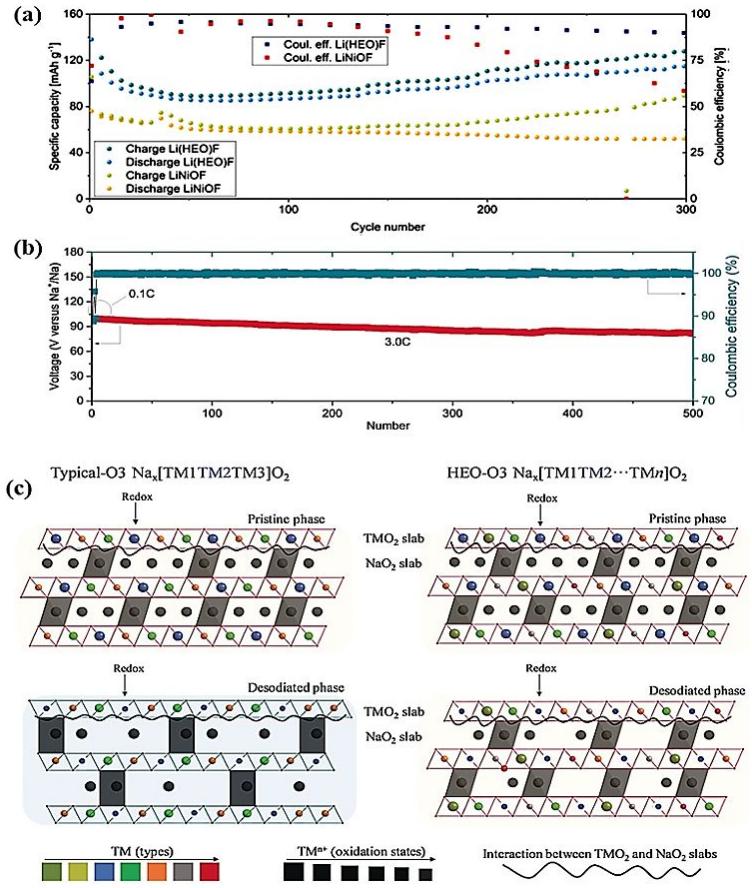


**Figure 20 -** (a) Capacity retention and Coulombic efficiency of Li(HEO)F and LiNiOF at 0.1 C. Reproduced with permission (ref. [227]). Copyright 2019, Royal Society of Chemistry. (b) Capacity retention and Coulombic efficiency of the $O_3$-type layered HEO at 3.0 C; and (c) schematic of the possible mechanism of the Na+ (de)intercalation process for typical $O_3$-type layered cathode (left) with three different transition metal (TM1-3) elements compared to HEO-$O_3$ layered cathode (right) with multiple transition metals (TM1-n). Reproduced with permission (ref. [228]). Copyright 2020, Wiley-VCH.

**Table 2 -** List of all high-entropy oxide tested as battery electrodes

| HEO Battery Electrode | Crystal Structure | Active Electrode | Performance | Ref |
|---|---|---|---|---|
| $(Co_{0.2}Cu_{0.2}Mg_{0.2}Ni_{0.2}Zn_{0.2})$ O | Rock-salt oxide Nano to micro size | Anode Half-cell test | Initial discharge specific capacity of 980 mAh $g^{-1}$ Reversible capacity of 590 mAh $g^{-1}$ at 0.2 A $g^{-1}$ after 500 cycles | 221 |
| $(Co_{0.2}Cu_{0.2}Mg_{0.2}Ni_{0.2}Zn_{0.2})$ O | Rock-salt oxide Nanocrystalline | Anode Half-cell test | Initial discharge specific capacity of 1585 mAh $g^{-1}$ Reversible capacity of 920 mAh $g^{-1}$ at 0.1 A $g^{-1}$ after 300 cycles | 223 |
| $(Co_{0.2}Cu_{0.2}Mg_{0.2}Ni_{0.2}Zn_{0.2})$ O | Rock-salt oxide Nanocrystalline | Anode Full cell with $LiNi_{1/3}Co_{1/3}Mn_{1/3}O_2$ cathode | Initial discharge specific capacity of 446 mAh $g^{-1}$ Reversible capacity of 256 mAh $g^{-1}$ at 0.12 A $g^{-1}$ after 100 cycles | 222 |
| $(Mg_{0.2}Ti_{0.2}Zn_{0.2}Cu_{0.2}Fe_{0.2})_3O_4$ | Spinel oxide Nanocrystalline | Anode Half-cell | Initial discharge specific capacity of 1261 mAh $g^{-1}$ Reversible capacity of 504 mAh $g^{-1}$ at 0.1A $g^{-1}$ after 300 cycles | 225 |
| $[(Bi, Na)_{0.2}(La, Li)_{0.2}(Ce, K)_{0.2}Ca_{0.2}Sr_{0.2}]TiO_3$ | Perovskite oxide Micro size | Anode Half-cell | Initial discharge specific capacity of 125.9 mAh $g^{-1}$ Reversible capacity of 120 mAh $g^{-1}$ at 1 A $g^{-1}$ after 300 cycles | 226 |
| $Li_x(Co_{0.2}Cu_{0.2}Mg_{0.2}Ni_{0.2}Zn_{0.2})OF_x$ | Rock-salt oxide Nanocrystalline | Cathode Half-cell | 90% of capacity retention at 0.1 C after 300 | 227 |
| $NaNi_{0.12}Cu_{0.12}Mg_{0.12}Fe_{0.15}Co_{0.15}Mn_{0.1}Ti_{0.1}Sn_{0.1}Sb_{0.04}O_2$ | $O_3$-Type layered oxide Micro size | Cathode Half-cell | 83% of capacity retention at 3 C after 500 cycles | 228 |

### 6.3 HEO as Chemical Anchor of Polysulfide in Li-S Batteries

An important challenge in Li-S batteries is the capacity fading during cycling due to the shuttle effect of LIPS.[229,230] Many efforts have contributed to finding the suitable catalyst material for the cathode to anchor the LIPS and improve the cycling stability of Li-S batteries. Multicomponent metal oxides such as $ZnCo_2O_4$ and $Ba_{0.5}Sr_{0.5}Co_{0.8}Fe_{0.2}O_{3-\delta}$ are examples of the materials proposed for this purpose as they can chemically immobilize the polysulfide in the cathode side.[231–234] Zheng *et al.*[235] reported on applying CoCuMgNiZnO as the cathode catalyst to anchor the LIPSs. They observed that due to the synergic contribution of Li-O and S-Ni binding interactions, HEO can highly restrain the LIPS by chemical absorption. Therefore, they tested the effect of HEO added to the KB carbon cathode in the Li-S cell. The obtained results demonstrated that the cells with HEMO-1/KB/S cathode and KB/S at 0.1C start working with very similar initial capacities of 1191 mAh $g^{-1}$ and 1131 mAh $g^{-1}$, respectively (Figure 18a). However, the cell with HEO catalyst maintained a high capacity over 200 cycles, while the routine KB/S cell showed very rapid capacity degradation (Figure 21a). Furthermore, testing at the higher charge/discharge rate of 0.5 C revealed the outstanding cycle stability of HEO/KB/S cell over 600 cycles comparing to the fast capacity fading of KB/S cell after 100 cycles (Figure 21b).

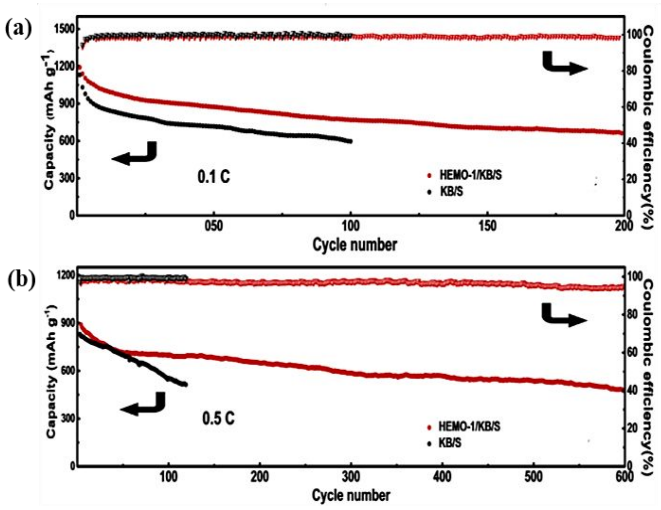


**Figure 21-** Capacity retention and Coulombic efficiency of the HEMO-1 and KB at (a) 0.1C and (b) 0.5C. Reproduced with permission (ref. [235]). Copyright 2019, Elsevier.

### 6.4 HEM as active electrode material in electrochemical capacitors

Electrochemical capacitors (ECs) or supercapacitors are electrochemical energy storage devices with long cycling life, power density and energy density higher than batteries and dielectric capacitors, respectively. The Electric double-layer capacitors (EDLCs) and pseudo-capacitors are two types of ECs working based on two different mechanisms. The energy storage in EDLCs happens because of electrostatic interaction in the double-layer between the electrode surface and electrolyte. The electrode material for EDLCs are carbon nanomaterials and provide high power density and long cycling but show limited energy density. On the other hand, faradaic charge transfer at the interface of pseudocapacitive electrode and electrolyte is the working mechanism in pseudo-capacitors, which provide higher energy density but suffer from poor cycling life.[236] Therefore, many efforts have been made to develop new electrode material for ECs with improved energy density and cycling life.

Lal and Sundara[211] employed the idea of metal oxide embedded in CNT using HEO NPs instead of single metal oxides. They synthesized the HEO based on Al, Co, Cr, Fe and Ni metal ions by sol-gel auto combustion method. The as-prepared nanoparticles were used as a catalyst for the CVD growth of CNTs to fabricate the HEO-CNT nanocomposite electrode (Figure 22a). The electrochemical performance of the nanocomposite electrode was tested in half cell and full cell with polyvinyl alcohol/$H_2SO_4$ hydrogel electrolyte. The CV plots of the full cell exhibited a quasi-rectangular shape due to the dual electric double layer and pseudo-capacitive behavior of nanocomposite electrode material (Figure 22b). More importantly, excellent cycling stability of assembled full cell EC working with the HEO-CNT nanocomposite electrode at the current density of 5 A $g^{-1}$ was achieved over 15000 cycles with 100% capacitance retention and Coulombic efficiency (Figure 22c).

Jin *et al.* [237] synthesized nitride HEM (HEMN-1) composed of equimolar V, Cr, Nb, Mo, Zr metals in a cubic crystal structure via soft urea method assisted by mechanochemical synthesis.

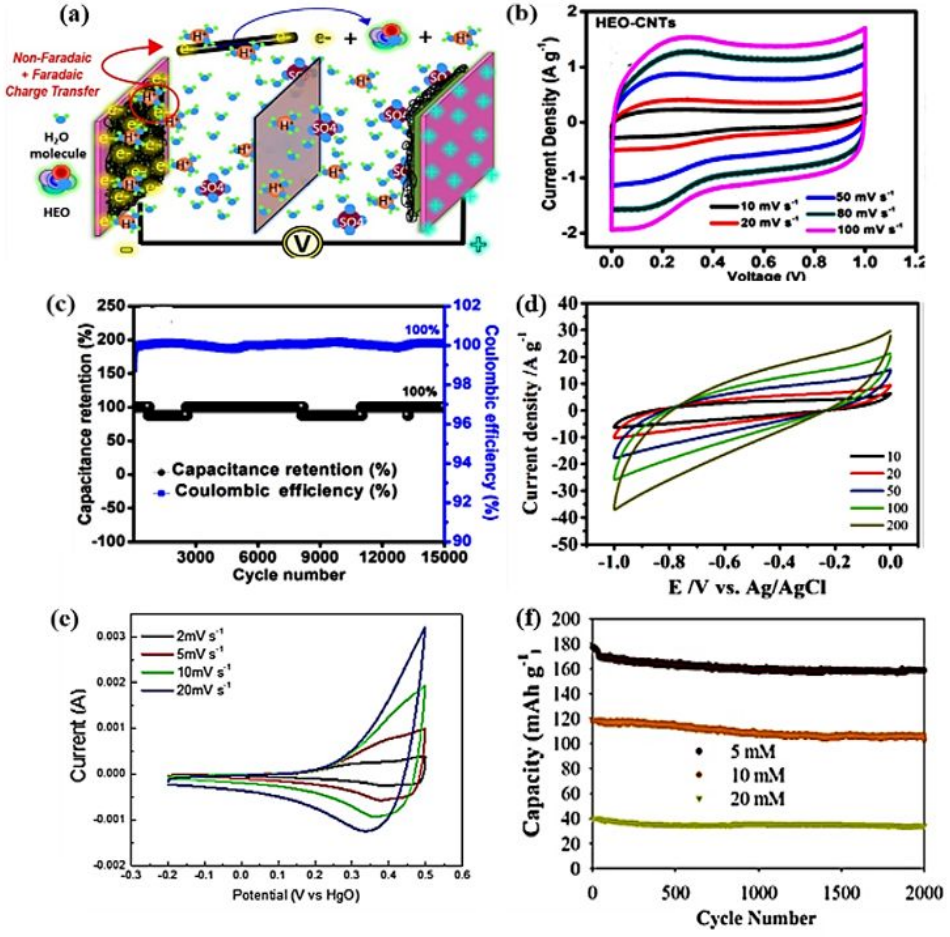


**Figure 22 -** (a) Schematic of ECs cell with HEO-CNT nanocomposite electrode; (b) CV curves at different scan rates for HEO-CNT nanocomposite electrode; and (c) capacitance retention and Coulombic efficiency at a current density of 5 A $g^{-1}$ for HEO−CNT nanocomposites electrode in the fc-EC fabrication with the PVA/ $H_2SO_4$ hydrogel electrolyte. Reproduced with permission (ref. [211]). Copyright 2019, American Chemical Society. (d) CV curves at different scan rates for HEMN-1 electrode in 1 m KOH electrolyte in a three-electrode cell. Reproduced with permission (ref. [237]). Copyright 2018, Wiley-VCH. (e) CV curves at different scan rates for Cr-Fe rich nano-porous HEA electrode in 1 M $H_2SO_4$ solution. Reproduced with permission (ref. [240]). Copyright 2019, Elsevier. (f) Capacity retention of HEA-NPs/ACNF electrodes formed from precursor concentration of 5, 10 and 20 mM in cell with 6 M KOH electrolyte solution. Reproduced with permission (ref. [241]). Copyright 2020, Elsevier.

The single-phase HEMN-1 was evaluated as an electrode for supercapacitor in 1 M KOH electrolyte solution. The cyclic voltammetry (CV) was obtained at different scan rates of 10, 20, 50, 100 and 200 mV $s^{-1}$ (Figure 22d) and the specific capacitance values of 230, 175, 113, 78, and 54 F $g^{-1}$ were calculated accordingly. The measured capacitance of the HEMN-1 electrode is higher compared to that of single metal nitride electrodes reported in the literature (46.9 F $g^{-1}$ for VN@C nanowire electrodes at 100 mV $s^{-1}$).[238,239]

Kong *et al.*[240] applied a single-phase nano-porous HEA as binder-free electrode for supercapacitor. The single-phase Cr-Fe rich HEM was obtained from the two-phase equimolar AlCoCrFeNi precursor by selective degloving of Al-Ni rich phase. Also, a thin nanometre layer of metal oxide/hydroxide was formed and detected on the surface of nano ligaments. As a combined result of having the highly conductive ligament metals in the core structure and pseudocapacitive oxide layer on the surface, the HEA electrode showed good performance with a high volumetric capacitance of 700 $cm^{-3}$ (Figure 22e) and long-term cycling stability of over 3000 cycles.

Xu *et al.* [241] recently reported the electrochemical performance of HEA NPs and carbon nanofiber (CNF) composite as a new supercapacitor electrode. In their study, using metal chloride precursor solution with different concentrations of 5, 10 and 20 mM, quinary FeNiCoMnMg HEA NPs are uniformly synthesized on aligned carbon nanofiber (ACNFs) through carbothermal shock method. The electrochemical performances of the HEA NPs/ACNFs electrodes were examined in a cell with 6 M KOH electrolyte solution. The composite electrode prepared by 5 mM precursor solution exhibited better performance with a high capacitance of 203 F/g and a specific energy density of 21.7 Wh/kg. Moreover, the electrode showed 89.2 % capacity retention up to 2000 cycles, which makes it a promising candidate for practical purposes (Figure 22f).

## 7. High-Entropy Material in Hydrogen Storage Application

Hydrogen is known as a potential renewable source of energy and green alternative for fossil fuels due to its abundance and various production and storage technologies. One of the suitable and safe hydrogen storage methods is using metal hydrides as an on-board hydrogen tank.[242–244] The most important properties of metal hydride to be used for hydrogen storage applications are high hydrogen storage capacity (>2 wt.% at room T), fast kinetics (high absorption-desorption reaction rate), easiness in activation, reversible and stable hydrogen absorption-desorption over cycling as well as the low cost of the metals and alloys.[242–244] Hydrogen atoms dissolved in the metal matrix occupy the octahedral and tetrahedral interstices sites of the crystal lattice.[245–247] This fact indicates that the maximum atomic ratio of absorbed hydrogens to metals or their alloys ($(\mathrm{H/M})_{\mathbf{max}}$) is related to the number of interstitial sites in the metallic host lattice.[248,249]

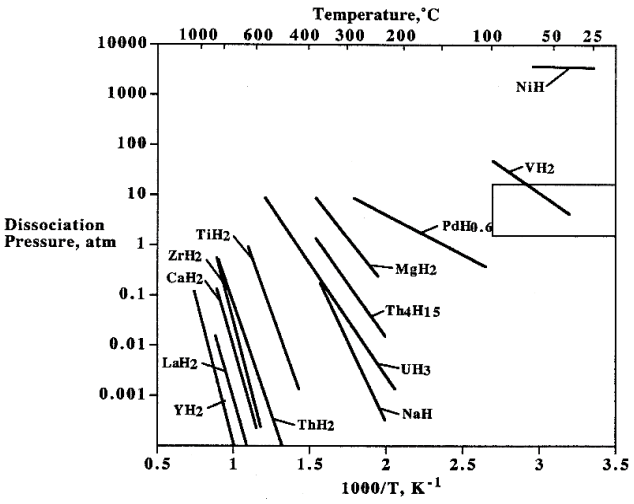


**Figure 23** - Van't Hoff lines of hydrogen desorption for metal hydrides. Reproduced with permission (ref. [250]). Copyright 1999, Elsevier.

Most of the metal elements can absorb hydrogen and form a hydride. However, the thermodynamic conditions that hydrogenation and dehydrogenation of metals occur are in a wide range for different elements. This can be explained by Pressure-Composition-Temperature (PCT) diagram of each element and its related Van't Hoff equation of $\ln \mathrm{P} = (\Delta \mathrm{H}/\mathrm{RT}) - (\Delta \mathrm{S}/\mathrm{R})$, where $\Delta \mathrm{H}$, $\Delta S$ and T are enthalpy, entropy and absolute temperature of the hydrating reaction, respectively, and R is the gas constant.[250] For all hydrides, $\Delta H$ and $\Delta S$ are negative during hydrogen absorption and the reaction is exothermic while they are both positive for the endothermic hydrogen desorption reaction. The change in entropy during hydrogen absorption and desorption reactions is mainly the change in entropy of hydrogen from the gas phase to metal solution phase and vice versa.[242] Therefore, from the Van't Hoff equation, for each metal at a constant given temperature, the constant pressure of hydrogenation or dehydrogenation (Plateau P) depends on the value of hydride reaction enthalpy and strength of the metal-hydrogen bonds.[242,250]

For the practical applications, it is favorable that desorption of hydrogen occurs in near-ambient conditions, i.e., temperature and pressure range of 1-100 °C and 1- 10 atm, respectively. Based on the Van't Hoff desorption lines for elemental hydrides (Figure 23)[250], only V has this thermodynamic condition for hydrogen desorption. The elemental hydride on the down-left side of the diagram with very low pressure and high-temperature ranges of hydrogen desorption is called strong hydride forms. On the other hand, the elemental hydride on the up-right with very high hydrogen desorption pressure is known as weak hydride forms. Therefore, the main reason for using metal alloy hydride instead of a pure metal hydride is to combine the strong (A, e.g., La, Ti and Zr) and weak (B, e.g., Ni, Mn and Co) hydride forming elements and make an alloy with intermediate thermodynamic affinities for hydrogen.

Over the years, various types and combinations of intermetallic compounds and alloys composed of weak and robust hydride former elements with different structures for hydrogen storage are studied. The most common types of these

alloys are $AB_5$ intermetallic compounds, $AB_2$ intermetallic compounds and solid solution alloys.[109] The effects of element selection and their composition in alloy, phases and crystal structure of alloy, as well as alloys' synthesis methods and heat treatment on hydrogen capacity (PCT diagram), equilibrium plateau pressure, hydrogen absorption and desorption kinetics, are mostly investigated.[115–128] Intermetallic compounds have a low hydrogen storage capacity limited to about 1.4 wt.%, which is not sufficient to meet the requirements for many hydrogen storage applications (capacity > 2 wt.%). The other problem related to intermetallic phases is their low cycling stability. However, alloys with intermetallic phase specially Laves phase structures, show fast kinetics for hydrogen absorption-desorption in addition to easy activation step for the processes.[243,251,252,257–259]

The BCC solid solutions are known to have very high hydrogen storage capacity (H/M > 2 wt.%), but they suffer from poor kinetic properties and difficulty in activation. BCC metals and their alloys usually undergo a structural transition during the hydrogenation process and show FCC structure in their hydride forms[243]. Among all BCC metals, only vanadium and rubidium hydrides can desorb the stored hydrogen at atmospheric pressure and the room temperature.[260] Hence many V-based solid solutions are studied, focusing on the impact of different added elements and their compositions on hydrogen storage properties of the system.[253–256,261–264]

The multiphase alloys with a mixture of BCC solid solution and intermetallic laves phase are found to have the intermediate properties of high hydrogen storage and fast kinetics. The concept of Laves phase-related BCC structure was introduced first by Akiba and Iba[243]. These multi-phase alloys showed high hydrogen storage on BCC phase and fast kinetic due to intermetallic Laves phases.[262,264–266] Kao *et al.*[267] reported the hydrogen storage properties of $CoFeMnTi_xV_yZr_z$ HEA with a single $C_{14}$ Laves phase structure. They also studied the effect of chemical composition and the affinity between alloy components and hydrogen on the maximum hydrogen capacity. It was found that the $CoFeMnTi_2VZr$ alloy exhibited maximum hydrogen capacity up to 1.8 wt.% at room temperature. Kunce *et al.*[268–270] synthesized ZrTiVCrFeNi, TiZrNbMoV and LaNiFeVMn[269] alloys with laser engineered net shaping (LENS) method and studied the effect of fabrication parameters and elemental compositions on alloy phases and hydrogen absorption-desorption properties associated with them. Based on their results, ZrTiVCrFeNi, with a dominant $C_{14}$ Laves phase, showed the maximum hydrogen capacity of 1.8 wt.% and 1.56 wt.% at 100 bar and 50 °C for as-synthesized and annealed samples, respectively[270]. TiZrNbMoV samples synthesized with different laser power led to different phase composition and hydrogen storage capacities. Chen *et al.* [271] showed that $Cr_uFe_vMn_wTi_xV_yZr_z$ HEAs have stable $C_{14}$ Laves structure during the absorption-desorption cycling, which is very beneficial for having a long-life alloy for hydrogen storage application. They also investigated the effect of elemental composition on maximum hydrogen capacity and kinetic of hydrogenation reaction while the phase structure of the alloys remained unchanged. It was concluded that $(H/M)_{max}$ is mainly dependent on hydride formation enthalpy of alloys which can be optimized by the compositions of hydrogen absorbing (Zr,Ti) and hydrogen desorbing (Fe,Mn,Cr) elements. Similarly, rate of the hydrogenation reaction increases with Fe,

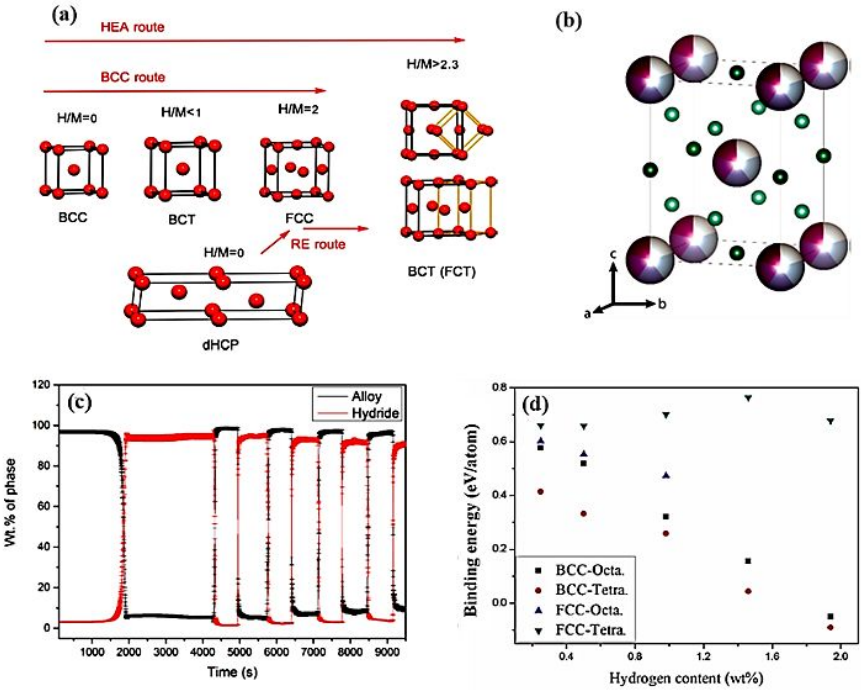


**Figure 24 -** (a) Different routes for hydrogen absorption in metals. Reproduced with permission (ref. [272]). Copyright 2016, Springer Nature. (b) Structural model for the metal deuteride; and (c) phase contents for the alloy and hydride phase at 500 °C. Reproduced with permission (ref. [273]). Copyright 2018, American Chemical Society. (d) Variation of the binding energy for the BCC and FCC hydrogenated TiZrHfMoNb with the H content. Octa.: octahedral occupation for H; Tetra.: Tetrahedral occupation for H (ref. [277]).

Mn and Cr concentrations while decreases with Zr concentration.

Sahlberg *et al.* [272] reported the hydrogen storage properties of an equimolar single solid solution TiVZrNbHf (synthesized by arc-melting) with BCC structure. They measured the $(H/M)_{max}$ of 2.5 equivalent to 2.7 wt.% for fully hydrogenated HEA hydride at 300 °C to 53 bar with a plateau pressure of 0.1 bar and a reversible H/M ratio range of 0.3-1.7 (~ 1.5 wt.%). The measured H/M ratio of 2.5 in the hydrogenated HEA (HEA-$H_{2.5}$) is higher than the maximum (H/M) ratio of 2 in fully hydrogenated binary hydrides of components ($MH_2$). They proposed a new mechanism of hydrogenation and the associated phase transition for HEA, which makes it different from normal BCC metals and other alloys. A normal BCC metal or alloy undergoes a phase transition during hydrogenation from initially BCC structure (H/M = 0) to distorted BCC (BCT) when getting partially hydrogenated (H/M <1) and finally to FCC in their fully hydrogenated form (H/M = 2) when hydrogen atoms occupy the tetrahedral sites (BCC route in Figure 24a). However, reaching to H/M ratio of 2.5 with the HEA indicates that in addition to all tetrahedral sites, hydrogen atoms could occupy about 50% of the octahedral sites. In the other hand, in phase transition during hydride formation of light rare-earth (RE) metals (La, Ce) with H/M >2, first the initial double hexagonal close-packed (dHCP) structure changes to FCC (H/M <3) and upon more hydrogenation, a distorted tetragonal FCC (BTC) structure is formed (RE route in Figure 23a). From the observed BTC structure of hydrogenated HEA with H/M >2, a unique hydrogenation mechanism, which is a combination of two BCC and RE routes, is introduced as the HEA route (Figure 24a). It is suggested that the high lattice strain build-up due to atomic size difference in HEA is the main reason for providing more available interstitial sites for hydrogen occupying and formation of final BCT structure in hydride HEA. The proposed mechanism was investigated more by neutron diffraction for determination of the positions of hydrogen atoms in the HEA hydride in their next study[273]. It was observed that at high temperature and pressure (500°C and 50 bar) hydrogen fills both tetrahedral and octahedral sites of the tetragonal structure (Figure 24b). The PCT diagram measurements showed that the hydrogen absorption-desorption is reversible at 500°C (Figure 24c). The reactions are kinetically slow due to the low activation energy of the alloy since the reaction rate increase slightly (about 20%) after activation over cycling (Figure 24c).

Different observation and phase transformation for the TiZrNbHfTa HEA with BCC structure was reported by the same group when they substituted V by the larger element of Ta to examine the effect of change in lattice size and distortion on hydrogen sorption properties of HEA.[274] They synthesized the alloy that undergoes the BCC route phase transition from BCC to BCT during hydrogenation and to FCC in the full hydride form. Moreover, two plateaus at low and high pressure were observed in pressure-composition isotherm curves, which is again like the hydrogenation behavior of ordinary BCC metals. The substitution of V by Ta leads to a decrease in the $\delta$ parameter from 6.8% to 4.6%, and consequently, a decrease in the associated lattice distortion. From the different observations for the mentioned HEAs, the authors suggested that higher $\delta$ could be responsible for single-phase transition from BCC to BCT and hydrogenation occupation in tetrahedral sites. The HEAs with smaller lattice distortion act similarly to normal BCC type metals.

In the following studies, Nygard *et al.*[118] investigated the accuracy of the hypothesis that the high atomic H/M ratio capacity of HEAs is related to the value of its lattice strain. They measured the hydrogen absorption-desorption and BCC/FCC lattice parameters of the synthesized $TiVZr_zNbTa_{1-z}$ alloys and their hydrides. The lattice parameter (a) and local lattice strain ($\boldsymbol{\delta}$) increases with the composition of Zr as the largest atom in the alloy. The result showed that all alloys (with BCC structures), regardless of their different lattice strains, have FCC structures in their hydride form and H/M ratio~2. Therefore, no relation between the hydrogen capacity of HEAs and higher lattice strain as well as Zr/M ratio was observed. However, increasing Zr composition in alloys stabilizes the hydrides. In another work[119], they studied the effect of VEC of the alloys on their hydride crystal structures and their corresponding hydrogen capacities. They showed that the BCC alloys with VEC < 4.75 form hydrides with a single FCC structure and others with VEC > 4.75 form hydrides with multiple FCC/BCC phases and the ratio of FCC phase of them decreases with VEC. However, the first result reported for TiVZrNbHf was not observed in their findings.

Shen *et al.* [277] reported the maximum hydrogen capacity of 1.18 wt.% and a reversible BCC to FCC phase transformation during hydrogenation at room temperature and atmospheric pressure for the TiZrHfMoNb. The stabilities of the BCC and FCC structures of TiZrHfMoNb and its hydride form were calculated with DFT method. It was confirmed that the BCC structure is preferable for pure alloy due to 0.25 eV/atom lower energy than the FCC structure. For the hydrogenated alloy, however, the FCC structure is always favorable because of the higher binding energies. Therefore, hydrogen occupies tetrahedral sites in the FCC phase and octahedral site in the BCC phase (Figure 24d). In the same group, Hu *et al.* [278] did a DFT study on hydrogen storage properties of TiZrHfScMo HEAs with a BCC structure. The calculated result showed the maximum hydrogen capacity of 2.14 wt.% can be obtained and elements in the alloy play different roles based on their covalent bonding energies with hydrogen atoms during hydrogenation. Zepon *et al.*[279] synthesized non-equimolar $MgZrTiFe_{0.5}Co_{0.5}Ni_{0.5}$ HEM *($A_2B$* chemical composition) and its $(MgZrTiFe_{0.5}Co_{0.5}Ni_{0.5})H_x$ hydride form with BCC and FCC structures, respectively. A maximum hydrogen capacity of 1.2 wt.% equivalents to a low atomic ratio of H/M = 0.7 was observed during absorption at 350°C, which indicates that there exist kinetic and thermodynamic limitations preventing further hydrogenation to form the dihydride of the alloy.

## 8. Prospective Applications

HEMs have demonstrated many appealing features and capabilities which have significantly boosted their potential applications in catalysis, energy conversion and storage. While further studies are ongoing to explore their durability and

performance under severe conditions, we briefly highlight other possible energy-related applications with the opportunity of employing HEMs.

### 8.1 Catalysis

Up to now, there is a limited number of studies on the catalysis performance of HEMs. However, their exceptional activities and favorable performances are inspiring to investigate them in many other catalysis applications. It was observed in different studies that HEAs have higher catalytic activity and longer stability compared to the single-atom and binary/ternary alloys. The superior catalytic performance of HEAs is attributed to their entropy-stabilized structure, synergistic effect and continuum active area provided by their highly disordered distribution of atoms. Therefore, it can be expected that HEMs are potential alternative catalysts for many other catalytic reactions relying on precise noble metals as their state-of-art catalysts. The concept can be applied to many Pt group unary, binary, or ternary alloy catalysts by adding more elements to improve their catalytic performances due to the synergistic effect and optimization of catalyst surface adsorption energies. More importantly, by adding non-noble metals like active transition metals to the system, the cost of the catalyst and, accordingly, the cost of the process reduces significantly while the performance is expected to be enhanced. However, the most desirable perspective is to employ HEAs composed of non-noble metals as considerably cheaper and more abundant material with comparable or even better activities and stabilities. Therefore, these materials can be one of the most attractive solutions for cost and sustainability problems related to green energy processes relying on precious metal catalysts.

HEMs, specially HEOs, are a suitable choice of material for any application that requires high temperature stable active catalyst due to the high-temperature dependency of entropic contribution in minimizing free Gibbs energy. In addition, HEOs are proper support for dispersion of single noble metal atoms on their highly active sites. This means they can play a double-effective role in improving the catalyst activity and reducing the cost of the materials by using less amount of precious metals. HEMs are also appealing choices for any application in harsh acidic and basic environmental, due to their high corrosion resistance.[280,281]

There are many binary and ternary transition metal alloys known as efficient catalysts for different applications. However, they usually suffer from a miscibility gap and limited compositional flexibility[76]. In this respect, adding two or three more proper elements to these combinates and employing them in the form of HEAs catalysis for the same reaction resolves not only the miscibility problem but also improves their activity and performance stability.

We also believe that other aspects of HEMs in catalysis applications are required to be investigated in future research works. (1) The intrinsic properties of HEAs in published studies are mostly tested by comparing the five-elemental alloys with four and less than four elemental alloys. However, it is still necessary to investigate the effect of the number of elements and compositions in HEMs with a higher number of elements to clearly examine the impact of adding components on properties and performances. (2) The inherent capability and high performance of HEMs are attributed to the known four effects of these materials (Figure 1). However, further studies are needed to fully understand the mechanisms by which catalytic HEMs work.

### 8.2 Batteries

A few types of HEOs are evaluated as electrode material for Li/Na ion batteries due to its high alkali ion conductivity and structural stability over cycling (Table 1). However, to broaden the observations and findings of their advanced performances, many various oxides and non-oxide HEMs with other compositions and crystal structures need to be examined as electrode material in different metal-ion batteries. HEAs can also be applied to SiGeSn type alloys for Li/Na-ion batteries, with the ability to control their properties with vast compositional tuning. Moreover, high electrocatalytic activity HEAs toward OER and ORR makes them a promising candidate for air electrode catalysts in Li and Na-air batteries[282].

Besides the application as electrode materials, due to the superior ionic conductivity of HEOs doped with alkali metal cations [216] (~$10^{-3}$ S $cm^{-1}$), they can be considered as solid-state electrolytes for alkali ion and alkali sulfur batteries. Similarly, it is worth studying the sulfide HEMs as a solid electrolyte for Li/Na-ion batteries and compared with the well-known sulfide solid electrolyte (LISICON and NASICON) [283].

Although high-entropy polymers are still in the early stages of development, further studies can be conducted to emerge new functional solid polymer electrolytes with enhanced ionic conductivity and cycling stability for Li/Na-ion batteries.[32,284] Addition of ionic conductive nanoparticles and nanosheets to the polymeric matrix are a known effective approach to increase the low ionic conductivity and mechanical stability of composite polymer electrolytes and eventually improve the performance of solid-electrolyte Li-ion batteries.[285,286] Many different types of metal oxides and ceramics nanoparticles or nano-flakes, as well as MOFs, have been used in the fabrication of polymer composite electrolyte and studied for their performance as solid electrolytes.[285–289] Due to the possible advantages of the high-entropy form of these materials (high-entropy oxide, nitride, phosphorus, and MOFs), many new high-entropy polymer-composite materials have the potential to be designed and studied in the future.

### 8.3 Electrochemical Capacitors (ECs)

Pseud-capacitors are one type of supercapacitors working based on faradic charge transfer mechanisms from redox reaction at the interface of the electrode (metal oxides)-electrolyte with high energy density but suffer from poor cycling life[236]. HEO composed of TM-metal oxides can be designed with optimal pseudo-capacitance properties to be used as electrode material in capacitors. Other HEMs like carbide HEM and sulfide HEM could also be suitable electrode material for EC devices since they are used in their binary and ternary forms before. The entropy-stabilization feature of these materials is expected to enhance the cycling stability of pseudo-capacitors, which is their

main disadvantage. Moreover, the colossal dialectic constant of rock-salt HEO doped with aliovalent cations could make them a proper candidate as solid electrolyte material in capacitors[85]. More investigations on other HEOs with different compositions are needed for a better understanding of this behavior. On the other hand, embedding metal NPs in polymers is known to have significant enchantment in dielectric constant.[290,291] In this regard, HEM NPs could be evaluated in a composite membrane as another novel solid electrolyte for capacitors.

### 8.4 Solar Cells

Solar is obviously one of the cleanest and most abundant sources of renewable energy. However, solar cells are still too expensive comparing to other energy sources concerning material cost and efficiency. Demanding low-cost, abundant, and highly effective material for different types of solar cells and accordingly, research efforts in this area are still facing challenges of finding new efficient advanced materials. High-entropy materials can provide further advantages in several parts of solar cells by improving efficiency and reducing the cost. Developing suitable HEAs with vast compositional tailoring enables the possibility of fine-tuning the optical properties and bandgap reduction of semiconductors materials for thin-film solar cells.

Wide bandgap metal oxides like $TiO_2$ and ZnO are imperative material in dye-sensitized solar cells (DSSC) and perovskite solar cells (PCS). Modifying their bandgap energy and optical properties of partial doping with other metal oxides is one of the adequate directions to improve the performance of cells. Obtaining a single-phase crystal structure is the difficulty in ternary oxides, which limits the compositional tuning and requires a very high synthesis temperature. These issues can be resolved by the concept of entropy-stabilization in single-phase HEO and their vast compositional space for the high number of elements.

The high-entropy concept is expanding to various types of material. In this regard, high-entropy halides could be another perspective material with superior properties compared to their binary and ternary forms. Designing and synthesizing single-phase crystallin high-entropy halide perovskites ($ABX_3$) as quantum dot material for light-sensitized perovskite solar cells is possible to have beneficial impacts on the performance of the cell.

### 8.5 Fuel Cells

HEMs have shown highly promising activity as anode and cathode electrocatalyst material for fuel cells. Still, many compositional spaces need to be explored for further

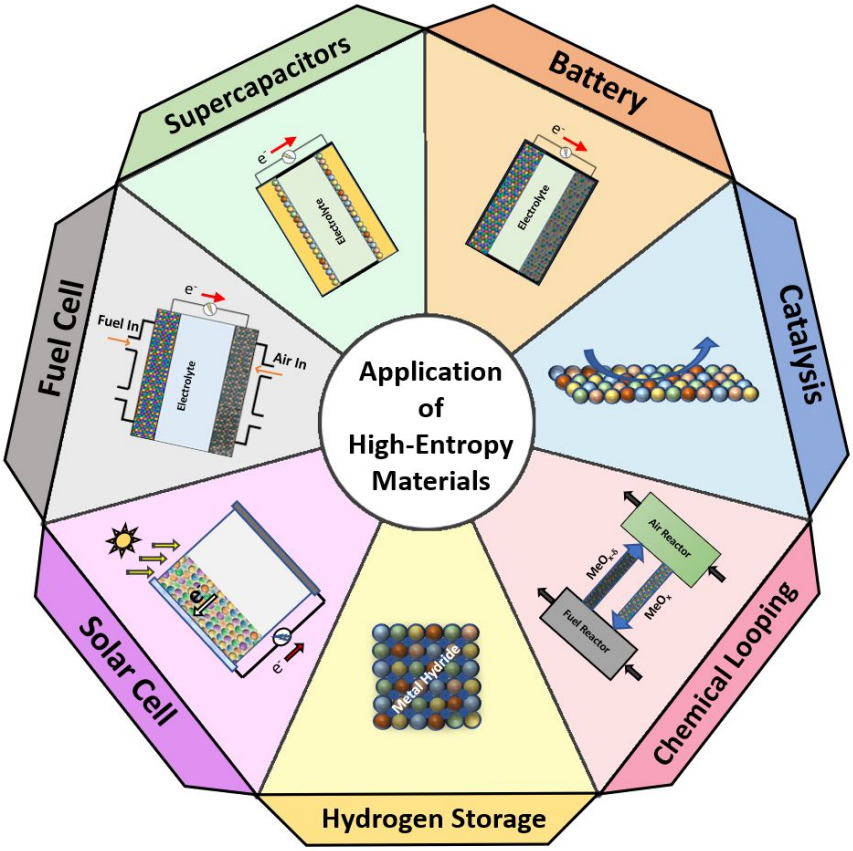


**Figure 25 -** Energy-related applications of high-entropy materials

performance optimization. Fluorite HEO, composed of

equimolar cerium and other rear earth elements, shows higher oxygen vacancies compared to binary oxides and doped cerium oxides with a limited amount of added elements.[11,12,292] Due to this high oxygen conductivity property and strong stability at high temperatures, they could be promising solid electrolyte material for solid oxide fuel. These features, as well as high chemical and mechanical stability comparable with YSZ, also make them an attractive choice of material for porous ceramic supports in molten carbonate fuel cell and ceramic-molten carbonate dual-phase membranes.[292]

### 8.6 Chemical Looping Systems

Oxygen stored in the lattice of metal oxides is used for methane combustion in chemical looping systems as an inherent $CO_2$ separation method or in chemical looping reforming for $H_2$ production.[293] In these systems, metal oxides as oxygen carriers circulating between two fuel and air reactors, where they are reduced by methane and re-oxidized by air, respectively [293]. The selection of proper oxygen carriers with high oxygen capacity and decent mechanical stability is a critical factor for the efficiency of systems.[294] $CeO_2$-based oxygen carriers have high oxygen capacity due to oxygen vacancies in lattice. Doping with other metal oxides like Zr, Fe and Cu can modify the performance of oxygen carriers in oxygen uptake and release the conversion and selectivity of the reaction as well.[295–298] However, the percentage of dopants is kept at a limited amount not to affect the fluorite structure of $CeO_2$. Fluorite HEO composed of near equimolar Ce and other metal cations in a single cubic crystalline structure with high oxygen vacancy and excellent mechanical stability is expected to be an ideal material selection for these applications. They can open a new perspective in oxygen carrier modification, and future studies can be directed to compositional space for optimizing their essential properties.

### 8.7 Hydrogen Storage

HEAs have shown remarkable hydrogen storage capacity and reversible phase transformation upon hydrogenation/dehydrogenation cycling. However, the details regarding the associated properties and factors affecting their hydrogen storage performance are not clear yet. Therefore, more comprehensive studies on potential HEMs are needed to clarify their specific advantages as hydrogen storage material. Also, computational studies on a large number of HEAs with various numbers and combinations of elements and their vast compositional tuning can explore new materials with enhanced hydrogen storage capabilities.

## 9. Summary

The concept of high-entropy is now covering a wide range of organic and inorganic materials and can be effectively used to design and develop vast types of new materials with desired properties. Entropy, as the level of the disorder, can be manipulated by both compositional complexity and structural disorder to evolve the mechanical and functional properties of materials for various applications.

HEMs, including metallic alloys as well as oxides, diborides, carbides, and sulfides, are emerging new materials with promising properties and high-performance durability due to their entropy-driven stabilization. High $\Delta S_{mix}$ associated with mixing five or more near-equimolar metal elements or ions favors the formation of a single-phase solid solution thermodynamically. Subsequent studies have shown that other thermodynamic and structural parameters as well as kinetic factors, are also important in the formation of a single-phase crystalline solid solution. Beyond the well-known mechanical properties, HEMs have received attention for the outstanding functional properties attributed to their entropic phase stabilization, lattice distortion, sluggish diffusion, and cocktail effects.

As catalyst materials or as catalyst supports, HEMs show outstanding properties. HEMs have been investigated as cathode/anode electrocatalyst for reactions like MOR, FAOR, EOR, ORR, HER and OER, as well as catalysts for ammonia decomposition, CO oxidation, $CO_2$ reduction and azo dye degradation. Noble-based and TM-based HEMs demonstrated higher activity and stability than many commercial Pt group catalysts. The enhanced performance of HEMs is described by the synergistic effect of multiple elements, higher atomic coordination and active surfaces, optimized surface adsorption energies and entropy-stabilization of their structure. HEOs also revealed outstanding properties as catalyst itself and stable support for homogenous dispersion of active metal single atoms. These manifest that HEMs are promising catalyst material with high activity, excellent stability and low-cost for several applications.

In the energy storage field, HEMs are shown to be promising as hydrogen storage materials, battery electrodes, and capacitors. HEAs with single-phase BCC structure are reported as a high capacity metallic alloy for hydrogen storage. Due to their interesting electrochemical properties such as colossal dielectric constant and high Li conductivity, HEOs are studied as electrode material for Li-ion batteries and performed with high capacity and long cycling life. Different types of HEM NPs demonstrated good performance in electrochemical capacitor systems. The outstanding physical and chemical properties of HEMs and their capability of being vastly compositional tuned make them a promising choice of material for various energy conversion and storage applications.

Organic high-entropy materials such as high-entropy polymers, meso-entropy 2D carbon and phosphorus materials are other potential material to receive more attention and be explored for desired properties in different energy-related applications. Organic high-entropy materials such as high-entropy polymers, meso-entropy 2D carbon and phosphorus materials are other potential material to receive more attention and be explored for desired properties in different energy-related applications.

## Conflicts of interest

There are no conflicts to declare.

## Acknowledgements

The authors acknowledge the financial support from National Science Foundation (NSF) Award DMR-1809439.

## References

(1) Cantor, B.; Chang, I. T. H.; Knight, P.; Vincent, A. J. B. Microstructural Development in Equiatomic Multicomponent Alloys. *Mater. Sci. Eng. A* **2004**, *375–377* (1-2 SPEC. ISS.), 213–218. https://doi.org/10.1016/j.msea.2003.10.257.

(2) Yeh, J. W.; Chen, S. K.; Lin, S. J.; Gan, J. Y.; Chin, T. S.; Shun, T. T.; Tsau, C. H.; Chang, S. Y. Nanostructured High-Entropy Alloys with Multiple Principal Elements: Novel Alloy Design Concepts and Outcomes. *Adv. Eng. Mater.* **2004**, *6* (5), 299-303+274. https://doi.org/10.1002/adem.200300567.

(3) Zhang, Y.; Zuo, T. T.; Tang, Z.; Gao, M. C.; Dahmen, K. A.; Liaw, P. K.; Lu, Z. P. Microstructures and Properties of High-Entropy Alloys. *Prog. Mater. Sci.* **2014**, *61* (September 2013), 1–93. https://doi.org/10.1016/j.pmatsci.2013.10.001.

(4) Yeh, J. W. Alloy Design Strategies and Future Trends in High-Entropy Alloys. *Jom* **2013**, *65* (12), 1759–1771. https://doi.org/10.1007/s11837-013-0761-6.

(5) Miracle, D. B.; Senkov, O. N. Acta Materialia A Critical Review of High Entropy Alloys and Related Concepts. *Acta Mater.* **2017**, *122*, 448–511. https://doi.org/10.1016/j.actamat.2016.08.081.

(6) Yeh, J.; Chen, S.; Gan, J.; Lin, S. *Communications: Formation of Simple Crystal Structures in Cu-Co-Ni-Cr-Al-Fe-Ti-V Alloys with Multiprincipal Metallic Elements*; 2004; Vol. 35.

(7) High-Entropy Alloys - B.S. Murty, Jien-Wei Yeh, S. Ranganathan, P. P. Bhattacharjee - Google Books https://books.google.com/books?hl=en&lr=&id=VU2NDwAAQBAJ&oi=fnd&pg=PP1&ots=_68YqvgEu9&sig=fZ2qQkGzzjU0CML6uDrU6WlFX3c#v=onepage&q&f=false (accessed Sep 11, 2020).

(8) Yeh, J.-W. Recent Progress in High-Entropy Alloys. *Ann. Chim. Sci. des Matériaux* **2006**, *31* (6), 633–648. https://doi.org/10.3166/acsm.31.633-648.

(9) Rost, C. M.; Sachet, E.; Borman, T.; Moballegh, A.; Dickey, E. C.; Hou, D.; Jones, J. L.; Curtarolo, S.; Maria, J. Entropy-Stabilized Oxides. *Nat. Commun.* **2015**, *6*, 1–8. https://doi.org/10.1038/ncomms9485.

(10) Djenadic, R.; Sarkar, A.; Clemens, O.; Loho, C.; Botros, M.; Chakravadhanula, V. S. K.; Kübel, C.; Bhattacharya, S. S.; Gandhi, A. S.; Hahn, H. Multicomponent Equiatomic Rare Earth Oxides. *Mater. Res. Lett.* **2017**, *5* (2), 102–109. https://doi.org/10.1080/21663831.2016.1220433.

(11) Gild, J.; Samiee, M.; Braun, J. L.; Harrington, T.; Vega, H.; Hopkins, P. E.; Vecchio, K.; Luo, J. High-Entropy Fluorite Oxides. *J. Eur. Ceram. Soc.* **2018**, *38* (10), 3578–3584. https://doi.org/10.1016/j.jeurceramsoc.2018.04.010.

(12) Chen, K.; Pei, X.; Tang, L.; Cheng, H.; Li, Z.; Li, C.; Zhang, X. Journal of the European Ceramic Society Short Communication A Fi Ve-Component Entropy-Stabilized Fl Uorite Oxide. *J. Eur. Ceram. Soc.* **2018**, *38* (11), 4161–4164. https://doi.org/10.1016/j.jeurceramsoc.2018.04.063.

(13) Sarkar, A.; Djenadic, R.; Wang, D.; Hein, C.; Kautenburger, R.; Clemens, O.; Hahn, H. Rare Earth and Transition Metal Based Entropy Stabilised Perovskite Type Oxides. *J. Eur. Ceram. Soc.* **2018**, *38* (5), 2318–2327. https://doi.org/10.1016/j.jeurceramsoc.2017.12.058.

(14) Jiang, S.; Hu, T.; Gild, J.; Zhou, N.; Nie, J.; Qin, M.; Harrington, T.; Vecchio, K.; Luo, J. A New Class of High-Entropy Perovskite Oxides. *Scr. Mater.* **2018**, *142*, 116–120. https://doi.org/10.1016/j.scriptamat.2017.08.040.

(15) Dąbrowa, J.; Stygar, M.; Mikuła, A.; Knapik, A.; Mroczka, K.; Tejchman, W.; Danielewski, M.; Martin, M. Synthesis and Microstructure of the (Co,Cr,Fe,Mn,Ni)3O4 High Entropy Oxide Characterized by Spinel Structure. *Mater. Lett.* **2018**, *216*, 32–36. https://doi.org/10.1016/j.matlet.2017.12.148.

(16) Wang, S.; wang, dongdong; LIU, Z.; DU, S.; ZHANG, Y.; Li, H.; Chen, R.; Wang, Y.; zou, yuqin; XIAO, Z.; CHEN, W. Low-Temperature Synthesis of Small-Size High-Entropy Oxide for Water Oxidation. *J. Mater. Chem. A* **2019**. https://doi.org/10.1039/c9ta08740k.

(17) Dusza, J.; Peter, Š.; Girman, V.; Sedlák, R.; Castle, E. G.; Csanádi, T.; Koval, A.; Reece, M. J. Journal of the European Ceramic Society Microstructure of ( Hf-Ta-Zr-Nb ) C High-Entropy Carbide at Micro and Nano / Atomic Level. **2018**, *38* (May), 4303–4307. https://doi.org/10.1016/j.jeurceramsoc.2018.05.006.

(18) Zhou, J.; Zhang, J.; Zhang, F.; Niu, B.; Lei, L.; Wang, W. High-Entropy Carbide : A Novel Class of Multicomponent Ceramics. *Ceram. Int.* **2018**, *44* (17), 22014–22018. https://doi.org/10.1016/j.ceramint.2018.08.100.

(19) Feng, L.; Fahrenholtz, W. G.; Hilmas, G. E.; Zhou, Y. Scripta Materialia Synthesis of Single-Phase High-Entropy Carbide Powders. *Scr. Mater.* **2019**, *162*, 90–93. https://doi.org/10.1016/j.scriptamat.2018.10.049.

(20) Chu, Y. Acta Materialia First-Principles Study , Fabrication and Characterization Of. *Acta Mater.* **2019**, *170*, 15–23. https://doi.org/10.1016/j.actamat.2019.03.021.

(21) Gild, J.; Zhang, Y.; Harrington, T.; Jiang, S.; Hu, T.; Quinn, M. C.; Mellor, W. M.; Zhou, N.; Vecchio, K.; Luo, J. High-Entropy Metal Diborides : A New Class of High-Entropy Materials and a New Type of Ultrahigh Temperature Ceramics. *Nat. Publ. Gr.* **2016**, *2016* (October), 2–11. https://doi.org/10.1038/srep37946.

(22) Mayrhofer, P. H.; Kirnbauer, A.; Ertelthaler, P.; Koller, C. M. Scripta Materialia High-Entropy Ceramic Thin Fi Lms ; A Case Study on Transition Metal Diborides. *Scr. Mater.* **2018**, *149*, 93–97. https://doi.org/10.1016/j.scriptamat.2018.02.008.

(23) Hsieh, M. H.; Tsai, M. H.; Shen, W. J.; Yeh, J. W. Structure and Properties of Two Al-Cr-Nb-Si-Ti High-Entropy Nitride Coatings. *Surf. Coatings Technol.* **2013**, *221*, 118–123. https://doi.org/10.1016/j.surfcoat.2013.01.036.

(24) Mo, A.; Ta, N.; Si, T. W.; Gild, J.; Braun, J.; Kaufmann, K.; Marin, E.; Harrington, T.; Hopkins, P.; Vecchio, K.; Luo, J. A High-Entropy Silicide: (Mo0.2Nb0.2Ta0.2Ti0.2W0.2)Si2. *J. Mater.* **2019**, No. xxxx. https://doi.org/10.1016/j.jmat.2019.03.002.

(25) Zhang, R.; Gucci, F.; Zhu, H.; Chen, K.; Reece, M. J. Data-

Driven Design of Ecofriendly Thermoelectric High-Entropy Sulfides. *Inorg. Chem.* **2018**, *57*, 13027–13033. https://doi.org/10.1021/acs.inorgchem.8b02379.

(26) Zhao, X.; Xue, Z.; Chen, W.; Wang, Y.; Mu, T. Eutectic Synthesis of High-Entropy Metal Phosphides for Electrocatalytic Water Splitting. *ChemSusChem* **2020**, 1–6. https://doi.org/10.1002/cssc.202000173.

(27) Wang, T.; Chen, H.; Yang, Z.; Liang, J.; Dai, S. High-Entropy Perovskite Fluorides: A New Platform for Oxygen Evolution Catalysis. *J. Am. Chem. Soc.* **2020**. https://doi.org/10.1021/jacs.9b12377.

(28) Materials, H.; Xu, W.; Chen, H.; Jie, K.; Yang, Z.; Li, T.; Dai, S. Zuschriften Entropy-Driven Mechanochemical Synthesis of Polymetallic Zeolitic Imidazolate Frameworks for CO 2 Fixation Zuschriften. **2019**, 5072–5076. https://doi.org/10.1002/ange.201900787.

(29) Huang, K.; Zhang, B.; Wu, J.; Zhang, T.; Peng, D.; Cao, X.; Zhang, Z.; Li, Z.; Huang, Y. Exploring the Impact of Atomic Lattice Deformation on Oxygen Evolution Reactions Based on a Sub-5 Nm Pure Face-Centred Cubic High-Entropy Alloy Electrocatalyst. *J. Mater. Chem. A* **2020**, *8* (24), 11938–11947. https://doi.org/10.1039/d0ta02125c.

(30) Zhao, X.; Xue, Z.; Chen, W.; Bai, X.; Shi, R.; Mu, T. Ambient Fast, Large-Scale Synthesis of Entropy-Stabilized Metal-Organic Framework Nanosheets for Electrocatalytic Oxygen Evolution. *J. Mater. Chem. A* **2019**, *7* (46), 26238–26242. https://doi.org/10.1039/c9ta09975a.

(31) Feng, B.; Zhuang, X. The Philosophy of Carbon: Meso-Entropy Materials. *Faraday Discuss.* **2019**. https://doi.org/10.1039/c9fd00115h.

(32) Wu, C. F.; Arifin, D. E. S.; Wang, C. A.; Ruan, J. Coalescence and Split of High-Entropy Polymer Lamellar Cocrystals. *Polymer (Guildf).* **2018**, *138*, 188–202. https://doi.org/10.1016/j.polymer.2018.01.064.

(33) Ye, Y. F.; Wang, Q.; Lu, J.; Liu, C. T.; Yang, Y. High-Entropy Alloy: Challenges and Prospects. *Mater. Today* **2016**, *19* (6), 349–362. https://doi.org/10.1016/j.mattod.2015.11.026.

(34) Zhang, W.; Liaw, P. K.; Zhang, Y. Science and Technology in High-Entropy Alloys. **2017**, 1–21.

(35) Yeh, J.; Lin, S. Breakthrough Applications of High-Entropy Materials. **2018**, 3129–3137. https://doi.org/10.1557/jmr.2018.283.

(36) George, E. P.; Raabe, D.; Ritchie, R. O. High-Entropy Alloys. *Nat. Rev. Mater.* https://doi.org/10.1038/s41578-019-0121-4.

(37) Steurer, W. Single-Phase High-Entropy Alloys – A Critical Update. *Mater. Charact.* **2020**, *162* (February), 110179. https://doi.org/10.1016/j.matchar.2020.110179.

(38) Zhang, Y.; Wen, C.; Wang, C.; Antonov, S.; Xue, D.; Bai, Y.; Su, Y. Phase Prediction in High Entropy Alloys with a Rational Selection of Materials Descriptors and Machine Learning Models. *Acta Mater.* **2020**, *185*, 528–539. https://doi.org/10.1016/j.actamat.2019.11.067.

(39) Gao, M. C.; Liaw, P. K.; Yeh, J. W.; Zhang, Y. *High-Entropy Alloys: Fundamentals and Applications*; 2016. https://doi.org/10.1007/978-3-319-27013-5.

(40) Sarkar, A.; Wang, Q.; Schiele, A.; Chellali, M. R.; Bhattacharya, S. S.; Wang, D.; Brezesinski, T.; Hahn, H.; Velasco, L.; Breitung, B. High-Entropy Oxides : Fundamental Aspects and Electrochemical Properties. **2019**, *1806236*. https://doi.org/10.1002/adma.201806236.

(41) Zhang, B. Y.; Zhou, Y. J.; Lin, J. P.; Chen, G. L.; Liaw, P. K. Solid-Solution Phase Formation Rules for Multi-Component Alloys **. **2008**, No. 6, 534–538. https://doi.org/10.1002/adem.200700240.

(42) Guo, S.; Liu, C. T. Phase Stability in High Entropy Alloys : Formation of Solid-Solution Phase or Amorphous Phase. *Prog. Nat. Sci. Mater. Int.* **2011**, *21* (6), 433–446. https://doi.org/10.1016/S1002-0071(12)60080-X.

(43) Yang, X.; Zhang, Y. Prediction of High-Entropy Stabilized Solid-Solution in Multi-Component Alloys. *Mater. Chem. Phys.* **2012**, *132* (2–3), 233–238. https://doi.org/10.1016/j.matchemphys.2011.11.021.

(44) Troparevsky, M. C.; Morris, J. R.; Kent, P. R. C.; Lupini, A. R.; Stocks, G. M. Criteria for Predicting the Formation of Single-Phase High-Entropy Alloys. **2015**, *011041*, 1–6. https://doi.org/10.1103/PhysRevX.5.011041.

(45) Singh, A. K.; Kumar, N.; Dwivedi, A.; Subramaniam, A. A Geometrical Parameter for the Formation of Disordered Solid Solutions in Multi-Component Alloys. *Intermetallics* **2014**, *53*, 112–119. https://doi.org/10.1016/j.intermet.2014.04.019.

(46) Phys, J. A. Effect of Valence Electron Concentration on Stability of Fcc or Bcc Phase in High Entropy Alloys. **2016**, *103505* (May 2011). https://doi.org/10.1063/1.3587228.

(47) Ye, Y. F.; Wang, Q.; Lu, J.; Liu, C. T.; Yang, Y. Design of High Entropy Alloys: A Single-Parameter Thermodynamic Rule. *Scr. Mater.* **2015**, *104*, 53–55. https://doi.org/10.1016/j.scriptamat.2015.03.023.

(48) Ye, Y. F.; Wang, Q.; Lu, J.; Liu, C. T.; Yang, Y. The Generalized Thermodynamic Rule for Phase Selection in Multicomponent Alloys. *Intermetallics* **2015**, *59*, 75–80. https://doi.org/10.1016/j.intermet.2014.12.011.

(49) Poletti, M. G.; Battezzati, L. ScienceDirect Electronic and Thermodynamic Criteria for the Occurrence of High Entropy Alloys in Metallic Systems. *Acta Mater.* **2014**, *75*, 297–306. https://doi.org/10.1016/j.actamat.2014.04.033.

(50) Miedema, A. R.; de Châtel, P. F.; de Boer, F. R. Cohesion in Alloys - Fundamentals of a Semi-Empirical Model. *Phys. B+C* **1980**, *100* (1), 1–28. https://doi.org/10.1016/0378-4363(80)90054-6.

(51) Zhang, K.; Fu, Z. Effects of Annealing Treatment on Phase Composition and Microstructure of CoCrFeNiTiAl x High-Entropy Alloys. *Intermetallics* **2012**, *22*, 24–32. https://doi.org/10.1016/j.intermet.2011.10.010.

(52) Mann, J. B.; Meek, T. L.; Allen, L. C. Configuration Energies of the Main Group Elements. **2000**, *III* (1), 2780–2783. https://doi.org/10.1021/ja992866e.

(53) Takeuchi, A.; Amiya, K.; Wada, T.; Yubuta, K.; Zhang, W. High-Entropy Alloys with a Hexagonal Close-Packed Structure Designed by Equi-Atomic Alloy Strategy and Binary Phase Diagrams. *Jom* **2014**, *66* (10), 1984–1992. https://doi.org/10.1007/s11837-014-1085-x.

(54) Zhao, Y. J.; Qiao, J. W.; Ma, S. G.; Gao, M. C.; Yang, H. J.;

 

Chen, M. W.; Zhang, Y. A Hexagonal Close-Packed High-Entropy Alloy: The Effect of Entropy. *Mater. Des.* **2016**, *96*, 10–15. https://doi.org/10.1016/j.matdes.2016.01.149.

(55) Feuerbacher, M.; Heidelmann, M.; Thomas, C. Hexagonal High-Entropy Alloys. *Mater. Res. Lett.* **2014**, *3* (1), 1–6. https://doi.org/10.1080/21663831.2014.951493.

(56) Phys, J. A. Effect of Valence Electron Concentration on Stability of Fcc or Bcc Phase in High Entropy Alloys. **2016**, *103505* (April 2011). https://doi.org/10.1063/1.3587228.

(57) Hume-Rothery Rules for Structurally Complex Alloy Phases - 1st Edition https://www.routledge.com/Hume-Rothery-Rules-for-Structurally-Complex-Alloy-Phases/Mizutani/p/book/9780367383374 (accessed Nov 2, 2020).

(58) Wang, F.; Zhang, Y.; Chen, G.; Davies, H. A. Tensile and Compressive Mechanical Behavior of a CoCrCuFeNiAl0.5 High Entropy Alloy. In *International Journal of Modern Physics B*; World Scientific Publishing Co. Pte Ltd, 2009; Vol. 23, pp 1254–1259. https://doi.org/10.1142/s0217979209060774.

(59) Senkov, O. N.; Wilks, G. B.; Miracle, D. B.; Chuang, C. P.; Liaw, P. K. Refractory High-Entropy Alloys. *Intermetallics* **2010**, *18* (9), 1758–1765. https://doi.org/10.1016/j.intermet.2010.05.014.

(60) Mansoori, G. A.; Carnahan, N. F.; Starling, K. E.; Leland, T. W. Equilibrium Thermodynamic Properties of the Mixture of Hard Spheres. *J. Chem. Phys.* **1971**, *54* (4), 1523–1525. https://doi.org/10.1063/1.1675048.

(61) Yang, Y.; Song, B.; Ke, X.; Xu, F.; Bozhilov, K. N.; Hu, L.; Shahbazian-yassar, R.; Zachariah, M. R. Aerosol Synthesis of High Entropy Alloy Nanoparticles. **2020**. https://doi.org/10.1021/acs.langmuir.9b03392.

(62) He, F.; Wang, Z.; Li, Y.; Wu, Q.; Li, J.; Wang, J.; Liu, C. T. Kinetic Ways of Tailoring Phases in High Entropy Alloys. *Sci. Rep.* **2016**, *6* (September), 1–9. https://doi.org/10.1038/srep34628.

(63) Luan, H. W.; Shao, Y.; Li, J. F.; Mao, W. L.; Han, Z. D.; Shao, C.; Yao, K. F. Phase Stabilities of High Entropy Alloys. *Scr. Mater.* **2020**, *179*, 40–44. https://doi.org/10.1016/j.scriptamat.2019.12.041.

(64) Anand, G.; Wynn, A. P.; Handley, C. M.; Freeman, C. L. Acta Materialia Phase Stability and Distortion in High-Entropy Oxides. *Acta Mater.* **2018**, *146*, 119–125. https://doi.org/10.1016/j.actamat.2017.12.037.

(65) Wu, Q.; Wang, Z.; He, F.; Wang, L.; Luo, J.; Li, J.; Wang, J. High Entropy Alloys: From Bulk Metallic Materials to Nanoparticles. *Metall. Mater. Trans. A Phys. Metall. Mater. Sci.* **2018**, *49* (10), 4986–4990. https://doi.org/10.1007/s11661-018-4802-1.

(66) Zhang, Y.; Zhou, Y. J.; Lin, J. P.; Chen, G. L.; Liaw, P. K. Solid-Solution Phase Formation Rules for Multi-Component Alloys. *Adv. Eng. Mater.* **2008**, *10* (6), 534–538. https://doi.org/10.1002/adem.200700240.

(67) Yeh, J. W.; Chen, S. K.; Lin, S. J.; Gan, J. Y.; Chin, T. S.; Shun, T. T.; Tsau, C. H.; Chang, S. Y. Nanostructured High-Entropy Alloys with Multiple Principal Elements: Novel Alloy Design Concepts and Outcomes. *Adv. Eng. Mater.* **2004**, *6* (5), 299–303. https://doi.org/10.1002/adem.200300567.

(68) Chen, X.; Si, C.; Gao, Y.; Frenzel, J.; Sun, J.; Eggeler, G.; Zhang, Z. Multi-Component Nanoporous Platinum-Ruthenium-Copper-Osmium-Iridium Alloy with Enhanced Electrocatalytic Activity towards Methanol Oxidation and Oxygen Reduction. *J. Power Sources* **2015**, *273*, 324–332. https://doi.org/10.1016/j.jpowsour.2014.09.076.

(69) Rekha, M. Y.; Mallik, N.; Srivastava, C. First Report on High Entropy Alloy Nanoparticle Decorated Graphene. *Sci. Rep.* **2018**, *8* (1), 8737. https://doi.org/10.1038/s41598-018-27096-8.

(70) Qiu, H.-J.; Fang, G.; Gao, J.; Wen, Y.; Lv, J.; Li, H.; Xie, G.; Liu, X.; Sun, S. Noble Metal-Free Nanoporous High-Entropy Alloys as Highly Efficient Electrocatalysts for Oxygen Evolution Reaction. *ACS Mater. Lett.* **2019**, *1* (5), 526–533. https://doi.org/10.1021/acsmaterialslett.9b00414.

(71) Li, S.; Tang, X.; Jia, H.; Li, H.; Xie, G.; Liu, X.; Lin, X.; Qiu, H. J. Nanoporous High-Entropy Alloys with Low Pt Loadings for High-Performance Electrochemical Oxygen Reduction. *J. Catal.* **2020**, *383*, 164–171. https://doi.org/10.1016/j.jcat.2020.01.024.

(72) Qiu, H. J.; Fang, G.; Wen, Y.; Liu, P.; Xie, G.; Liu, X.; Sun, S. Nanoporous High-Entropy Alloys for Highly Stable and Efficient Catalysts. *J. Mater. Chem. A* **2019**, *7* (11), 6499–6506. https://doi.org/10.1039/c9ta00505f.

(73) Bondesgaard, M.; Broge, N. L. N.; Mamakhel, A.; Bremholm, M.; Iversen, B. B. General Solvothermal Synthesis Method for Complete Solubility Range Bimetallic and High-Entropy Alloy Nanocatalysts. *Adv. Funct. Mater.* **2019**, *29* (50), 1905933. https://doi.org/10.1002/adfm.201905933.

(74) Liu, M.; Zhang, Z.; Okejiri, F.; Yang, S.; Zhou, S.; Dai, S. Entropy-Maximized Synthesis of Multimetallic Nanoparticle Catalysts via a Ultrasonication-Assisted Wet Chemistry Method under Ambient Conditions. *Adv. Mater. Interfaces* **2019**, *6* (7), 1900015. https://doi.org/10.1002/admi.201900015.

(75) Niu, B.; Zhang, F.; Ping, H.; Li, N.; Zhou, J.; Lei, L.; Xie, J.; Zhang, J.; Wang, W.; Fu, Z. Sol-Gel Autocombustion Synthesis of Nanocrystalline High-Entropy Alloys. *Sci. Rep.* **2017**, *7* (1), 1–7. https://doi.org/10.1038/s41598-017-03644-6.

(76) Xie, P.; Yao, Y.; Huang, Z.; Liu, Z.; Zhang, J.; Li, T.; Wang, G.; Shahbazian-Yassar, R.; Hu, L.; Wang, C. Highly Efficient Decomposition of Ammonia Using High-Entropy Alloy Catalysts. *Nat. Commun.* **2019**, *10* (1), 1–12. https://doi.org/10.1038/s41467-019-11848-9.

(77) Yao, Y.; Huang, Z.; Xie, P.; Lacey, S. D.; Jacob, R. J.; Xie, H.; Chen, F.; Nie, A.; Pu, T.; Rehwoldt, M.; Yu, D.; Zachariah, M. R.; Wang, C.; Shahbazian-Yassar, R.; Li, J.; Hu, L. Carbothermal Shock Synthesis of High-Entropy-Alloy Nanoparticles. *Science (80-. ).* **2018**, *359* (6383), 1489–1494. https://doi.org/10.1126/science.aan5412.

(78) Xu, X.; Du, Y.; Wang, C.; Guo, Y.; Zou, J.; Zhou, K.; Zeng, Z.; Liu, Y.; Li, L. High-Entropy Alloy Nanoparticles on Aligned Electronspun Carbon Nanofibers for Supercapacitors. **2020**. https://doi.org/10.1016/j.jallcom.2020.153642.

(79) Gao, S.; Hao, S.; Huang, Z.; Yuan, Y.; Han, S.; Lei, L.; Zhang,

X.; Shahbazian-Yassar, R.; Lu, J. Synthesis of High-Entropy Alloy Nanoparticles on Supports by the Fast Moving Bed Pyrolysis. *Nat. Commun.* **2020**, *11* (1). https://doi.org/10.1038/s41467-020-15934-1.

(80) Löffler, T.; Meyer, H.; Savan, A.; Wilde, P.; Garzón Manjón, A.; Chen, Y.-T.; Ventosa, E.; Scheu, C.; Ludwig, A.; Schuhmann, W. Discovery of a Multinary Noble Metal-Free Oxygen Reduction Catalyst. *Adv. Energy Mater.* **2018**, *8* (34), 1802269. https://doi.org/10.1002/aenm.201802269.

(81) Tsai, C. F.; Wu, P. W.; Lin, P.; Chao, C. G.; Yeh, K. Y. Sputter Deposition of Multi-Element Nanoparticles as Eleetroeatalysts for Methanol Oxidation. *Jpn. J. Appl. Phys.* **2008**, *47* (7 PART 1), 5755–5761. https://doi.org/10.1143/JJAP.47.5755.

(82) Tomboc, G. M.; Kwon, T.; Joo, J.; Lee, K. High Entropy Alloy Electrocatalysts: A Critical Assessment of Fabrication and Performance. *J. Mater. Chem. A* **2020**, *8* (30), 14844–14862. https://doi.org/10.1039/d0ta05176d.

(83) Xin, Y.; Li, S.; Qian, Y.; Zhu, W.; Yuan, H.; Jiang, P.; Guo, R.; Wang, L. High-Entropy Alloys as a Platform for Catalysis: Progress, Challenges, and Opportunities. *ACS Catal.* **2020**, 11280–11306. https://doi.org/10.1021/acscatal.0c03617.

(84) Ostovari Moghaddam, A.; Trofimov, E. A. Toward Expanding the Realm of High Entropy Materials to Platinum Group Metals: A Review. *J. Alloys Compd.* **2021**, *851*. https://doi.org/10.1016/j.jallcom.2020.156838.

(85) Cnrs, I. U. M. R.; Paris-sud, U.; Paris-saclay, U.; Bérardan, D.; Franger, S.; Dragoe, D.; Meena, A. K.; Dragoe, N. Colossal Dielectric Constant in High Entropy Oxides Pss. **2016**, *333* (4), 328–333. https://doi.org/10.1002/pssr.201600043.

(86) Sarkar, A.; Djenadic, R.; Usharani, N. J.; Sanghvi, K. P.; Chakravadhanula, V. S. K.; Gandhi, A. S.; Hahn, H.; Bhattacharya, S. S. Nanocrystalline Multicomponent Entropy Stabilised Transition Metal Oxides. *J. Eur. Ceram. Soc.* **2017**, *37* (2), 747–754. https://doi.org/10.1016/j.jeurceramsoc.2016.09.018.

(87) Biesuz, M.; Spiridigliozzi, L.; Dell'Agli, G.; Bortolotti, M.; Sglavo, V. M. Synthesis and Sintering of (Mg, Co, Ni, Cu, Zn)O Entropy-Stabilized Oxides Obtained by Wet Chemical Methods. *J. Mater. Sci.* **2018**, *53* (11), 8074–8085. https://doi.org/10.1007/s10853-018-2168-9.

(88) Wang, D.; Liu, Z.; Du, S.; Zhang, Y.; Li, H.; Xiao, Z.; Chen, W.; Chen, R.; Wang, Y.; Zou, Y.; Wang, S. Low-Temperature Synthesis of Small-Sized High-Entropy Oxides for Water Oxidation. *J. Mater. Chem. A* **2019**, *7* (42), 24211–24216. https://doi.org/10.1039/c9ta08740k.

(89) Djenadic, R.; Sarkar, A.; Clemens, O.; Loho, C.; Botros, M.; Chakravadhanula, V. S. K.; Kübel, C.; Bhattacharya, S. S.; Gandhi, A. S.; Hahn, H. Multicomponent Equiatomic Rare Earth Oxides. *Mater. Res. Lett.* **2017**, *5* (2), 102–109. https://doi.org/10.1080/21663831.2016.1220433.

(90) Sarkar, A.; Djenadic, R.; Wang, D.; Hein, C.; Kautenburger, R.; Clemens, O.; Hahn, H. Rare Earth and Transition Metal Based Entropy Stabilised Perovskite Type Oxides. *J. Eur. Ceram. Soc.* **2018**, *38* (5), 2318–2327. https://doi.org/10.1016/j.jeurceramsoc.2017.12.058.

(91) Chen, H.; Lin, W.; Zhang, Z.; Jie, K.; Mullins, D. R.; Sang, X.; Yang, S. Z.; Jafta, C. J.; Bridges, C. A.; Hu, X.; Unocic, R. R.; Fu, J.; Zhang, P.; Dai, S. Mechanochemical Synthesis of High Entropy Oxide Materials under Ambient Conditions: Dispersion of Catalysts via Entropy Maximization. *ACS Mater. Lett.* **2019**, *1* (1), 83–88. https://doi.org/10.1021/acsmaterialslett.9b00064.

(92) Balcerzak, M.; Kawamura, K.; Bobrowski, R.; Rutkowski, P.; Brylewski, T. Mechanochemical Synthesis of (Co,Cu,Mg,Ni,Zn)O High-Entropy Oxide and Its Physicochemical Properties. *J. Electron. Mater.* **2019**, *48* (11), 7105–7113. https://doi.org/10.1007/s11664-019-07512-z.

(93) Okejiri, F.; Zhang, Z.; Liu, J.; Liu, M.; Yang, S.; Dai, S. Room-Temperature Synthesis of High-Entropy Perovskite Oxide Nanoparticle Catalysts through Ultrasonication-Based Method. *ChemSusChem* **2020**, *13* (1), 111–115. https://doi.org/10.1002/cssc.201902705.

(94) Mao, A.; Xiang, H. Z.; Zhang, Z. G.; Kuramoto, K.; Yu, H.; Ran, S. Solution Combustion Synthesis and Magnetic Property of Rock-Salt (Co 0.2 Cu 0.2 Mg 0.2 Ni 0.2 Zn 0.2 )O High-Entropy Oxide Nanocrystalline Powder. *J. Magn. Magn. Mater.* **2019**, *484*, 245–252. https://doi.org/10.1016/j.jmmm.2019.04.023.

(95) Sarkar, A.; Breitung, B.; Hahn, H. High Entropy Oxides: The Role of Entropy, Enthalpy and Synergy. *Scr. Mater.* **2020**, *187*, 43–48. https://doi.org/10.1016/j.scriptamat.2020.05.019.

(96) Xin, Y.; Li, S.; Qian, Y.; Zhu, W.; Yuan, H.; Jiang, P.; Guo, R.; Wang, L. High-Entropy Alloys as a Platform for Catalysis: Progress, Challenges, and Opportunities. *ACS Catalysis*. American Chemical Society 2020, pp 11280–11306. https://doi.org/10.1021/acscatal.0c03617.

(97) Titus, D.; James Jebaseelan Samuel, E.; Roopan, S. M. Nanoparticle Characterization Techniques. In *Green Synthesis, Characterization and Applications of Nanoparticles*; Elsevier, 2019; pp 303–319. https://doi.org/10.1016/b978-0-08-102579-6.00012-5.

(98) Mourdikoudis, S.; Pallares, R. M.; Thanh, N. T. K. Characterization Techniques for Nanoparticles: Comparison and Complementarity upon Studying Nanoparticle Properties. *Nanoscale*. Royal Society of Chemistry July 21, 2018, pp 12871–12934. https://doi.org/10.1039/c8nr02278j.

(99) Qiu, H. J.; Fang, G.; Wen, Y.; Liu, P.; Xie, G.; Liu, X.; Sun, S. Nanoporous High-Entropy Alloys for Highly Stable and Efficient Catalysts. *J. Mater. Chem. A* **2019**, *7* (11), 6499–6506. https://doi.org/10.1039/c9ta00505f.

(100) Waag, F.; Li, Y.; Ziefuß, A. R.; Bertin, E.; Kamp, M.; Duppel, V.; Marzun, G.; Kienle, L.; Barcikowski, S.; Gökce, B. Kinetically-Controlled Laser-Synthesis of Colloidal High-Entropy Alloy Nanoparticles. *RSC Adv.* **2019**, *9* (32), 18547–18558. https://doi.org/10.1039/c9ra03254a.

(101) Yao, Y.; Liu, Z.; Xie, P.; Huang, Z.; Li, T.; Morris, D.; Finfrock, Z.; Zhou, J.; Jiao, M.; Gao, J.; Mao, Y.; Miao, J.; Zhang, P.; Shahbazian-Yassar, R.; Wang, C.; Wang, G.; Hu, L. Computationally Aided, Entropy-Driven Synthesis of Highly Efficient and Durable Multi-Elemental Alloy Catalysts. *Sci.*

*Adv.* **2020**, *6* (11), 510–523. https://doi.org/10.1126/sciadv.aaz0510.

(102) Liu, H.; Song, C.; Zhang, L.; Zhang, J.; Wang, H.; Wilkinson, D. P. A Review of Anode Catalysis in the Direct Methanol Fuel Cell. **2006**, *155*, 95–110. https://doi.org/10.1016/j.jpowsour.2006.01.030.

(103) Wang, F. H.; Jhuang, H. S.; Eremin, E. N.; Syzdykova, A. S. Sputter Deposition of Multi-Element Nanoparticles as Electrocatalysts for Methanol Oxidation. **2008**. https://doi.org/10.1143/JJAP.47.5755.

(104) Reddington, E.; Sapienza, A.; Gurau, B.; Viswanathan, R.; Sarangapani, S.; Smotkin, E. S.; Mallouk, T. E. Combinatorial Electrochemistry : A Highly Parallel , Optical Screening Method for Discovery of Better Electrocatalysts. **1998**, *280* (June), 1–4.

(105) Gurau, B.; Viswanathan, R.; Liu, R.; Lafrenz, T. J.; Ley, K. L.; Smotkin, E. S.; Reddington, E.; Sapienza, A.; Chan, B. C.; Mallouk, T. E.; Pennsylania, T.; Uni, S.; Park, U. V; Pennsyl, V. Structural and Electrochemical Characterization of Binary , Ternary , and Quaternary Platinum Alloy Catalysts for Methanol Electro-Oxidation 1. **1998**, No. 5, 9997–10003. https://doi.org/10.1021/jp982887f.

(106) Igarashi, H.; Fujino, T.; Zhu, Y.; Uchida, H.; Watanabe, M. CO Tolerance of Pt Alloy Electrocatalysts for Polymer Electrolyte Fuel Cells and the DetoxiÐcation Mechanism. **2001**.

(107) Uchida, H.; Ozuka, H.; Watanabe, M. Electrochemical Quartz Crystal Microbalance Analysis of CO-Tolerance at Pt Ã Fe Alloy Electrodes. **2002**, *47*, 3629–3636.

(108) Guo, J. W.; Zhao, T. S.; Prabhuram, J.; Chen, R.; Wong, C. W. Preparation and Characterization of a PtRu / C Nanocatalyst for Direct Methanol Fuel Cells. **2005**, *51*, 754–763. https://doi.org/10.1016/j.electacta.2005.05.056.

(109) Yajima, T.; Uchida, H.; Watanabe, M. In-Situ ATR-FTIR Spectroscopic Study of Electro-Oxidation of Methanol and Adsorbed CO at Pt-Ru Alloy. *J. Phys. Chem. B* **2004**, *108* (8), 2654–2659. https://doi.org/10.1021/jp037215q.

(110) Zou, L.; Guo, J.; Liu, J.; Zou, Z.; Akins, D. L.; Yang, H. Highly Alloyed PtRu Black Electrocatalysts for Methanol Oxidation Prepared Using Magnesia Nanoparticles as Sacri Fi Cial Templates. *J. Power Sources* **2014**, *248*, 356–362. https://doi.org/10.1016/j.jpowsour.2013.09.086.

(111) Strasser, P.; Fan, Q.; Devenney, M.; Weinberg, W. H.; Liu, P.; Nørskov, J. K. High Throughput Experimental and Theoretical Predictive Screening of Materials - A Comparative Study of Search Strategies for New Fuel Cell Anode Catalysts. **2003**, 11013–11021. https://doi.org/10.1021/jp030508z.

(112) Park, K.; Choi, J.; Lee, S.; Pak, C.; Chang, H. PtRuRhNi Nanoparticle Electrocatalyst for Methanol Electrooxidation in Direct Methanol Fuel Cell. **2004**, *224*, 236–242. https://doi.org/10.1016/j.jcat.2004.02.010.

(113) Whitacre, J. F.; Valdez, T.; Narayanan, S. R. Investigation of Direct Methanol Fuel Cell Electrocatalysts Using a Robust Combinatorial Technique. **2005**, 1780–1789. https://doi.org/10.1149/1.1990129.

(114) Dai, W.; Lu, T.; Pan, Y. Novel and Promising Electrocatalyst for Oxygen Evolution Reaction Based on MnFeCoNi High Entropy Alloy. *J. Power Sources* **2019**, *430* (April), 104–111. https://doi.org/10.1016/j.jpowsour.2019.05.030.

(115) Tsai, C.; Yeh, K.; Wu, P.; Hsieh, Y.; Lin, P. Effect of Platinum Present in Multi-Element Nanoparticles on Methanol Oxidation. **2009**, *478*, 868–871. https://doi.org/10.1016/j.jallcom.2008.12.055.

(116) Chen, X.; Si, C.; Gao, Y.; Frenzel, J.; Sun, J.; Eggeler, G.; Zhang, Z. Multi-Component Nanoporous Platinum e Ruthenium e Copper e Osmium e Iridium Alloy with Enhanced Electrocatalytic Activity towards Methanol Oxidation and Oxygen Reduction. *J. Power Sources* **2015**, *273*, 324–332. https://doi.org/10.1016/j.jpowsour.2014.09.076.

(117) Chen, Y. X.; Lavacchi, A.; Chen, S. P.; Di Benedetto, F.; Bevilacqua, M.; Bianchini, C.; Fornasiero, P.; Innocenti, M.; Marelli, M.; Oberhauser, W.; Sun, S. G.; Vizza, F. Electrochemical Milling and Faceting: Size Reduction and Catalytic Activation of Palladium Nanoparticles. *Angew. Chemie - Int. Ed.* **2012**, *51* (34), 8500–8504. https://doi.org/10.1002/anie.201203589.

(118) Tian, N.; Zhou, Z. Y.; Sun, S. G. Electrochemical Preparation of Pd Nanorods with High-Index Facets. *Chem. Commun.* **2009**, No. 12, 1502–1504. https://doi.org/10.1039/b819751b.

(119) Xing, Y.; Cai, Y.; Vukmirovic, M. B.; Zhou, W. P.; Karan, H.; Wang, J. X.; Adzic, R. R. Enhancing Oxygen Reduction Reaction Activity via Pd-Au Alloy Sublayer Mediation of Pt Monolayer Electrocatalysts. *J. Phys. Chem. Lett.* **2010**, *1* (21), 3238–3242. https://doi.org/10.1021/jz101297r.

(120) Mazumder, V.; Chi, M.; Mankin, M. N.; Liu, Y.; Metin, Ö.; Sun, D.; More, K. L.; Sun, S. A Facile Synthesis of MPd (M = Co, Cu) Nanoparticles and Their Catalysis for Formic Acid Oxidation. *Nano Lett.* **2012**, *12* (2), 1102–1106. https://doi.org/10.1021/nl2045588.

(121) Du, W.; MacKenzie, K. E.; Milano, D. F.; Deskins, N. A.; Su, D.; Teng, X. Palladium-Tin Alloyed Catalysts for the Ethanol Oxidation Reaction in an Alkaline Medium. *ACS Catal.* **2012**, *2* (2), 287–297. https://doi.org/10.1021/cs2005955.

(122) Wang, A. L.; Wan, H. C.; Xu, H.; Tong, Y. X.; Li, G. R. Quinary PdNiCoCuFe Alloy Nanotube Arrays as Efficient Electrocatalysts for Methanol Oxidation. *Electrochim. Acta* **2014**, *127*, 448–453. https://doi.org/10.1016/j.electacta.2014.02.076.

(123) Wang, Y.; Zou, S.; Catalysts, W. C.-; 2015, undefined. Recent Advances on Electro-Oxidation of Ethanol on Pt-and Pd-Based Catalysts: From Reaction Mechanisms to Catalytic Materials. *mdpi.com*.

(124) Fang, X.; Wang, L.; Shen, P. K.; Cui, G.; Bianchini, C. An in Situ Fourier Transform Infrared Spectroelectrochemical Study on Ethanol Electrooxidation on Pd in Alkaline Solution. *J. Power Sources* **2010**, *195* (5), 1375–1378. https://doi.org/10.1016/j.jpowsour.2009.09.025.

(125) Lai, S. C. S.; Koper, M. T. M. The Influence of Surface Structure on Selectivity in the Ethanol Electro-Oxidation Reaction on Platinum. *J. Phys. Chem. Lett.* **2010**, *1* (7), 1122–1125. https://doi.org/10.1021/jz100272f.

(126) Pech-Rodríguez, W. J.; González-Quijano, D.; Vargas-

Gutiérrez, G.; Morais, C.; Napporn, T. W.; Rodríguez-Varela, F. J. Electrochemical and in Situ FTIR Study of the Ethanol Oxidation Reaction on PtMo/C Nanomaterials in Alkaline Media. *Appl. Catal. B Environ.* **2017**, *203*, 654–662. https://doi.org/10.1016/j.apcatb.2016.10.058.

(127) Wu, D.; Kusada, K.; Yamamoto, T.; Toriyama, T.; Matsumura, S.; Kawaguchi, S.; Kubota, Y.; Kitagawa, H. Platinum-Group-Metal High-Entropy-Alloy Nanoparticles. *J. Am. Chem. Soc.* **2020**, *142* (32), 13833–13838. https://doi.org/10.1021/jacs.0c04807.

(128) Liang, Z.; Song, L.; Deng, S.; Zhu, Y.; Stavitski, E.; Adzic, R. R.; Chen, J.; Wang, J. X. Direct 12-Electron Oxidation of Ethanol on a Ternary Au(Core)-PtIr(Shell) Electrocatalyst. *J. Am. Chem. Soc.* **2019**, *141* (24), 9629–9636. https://doi.org/10.1021/jacs.9b03474.

(129) Marcinkowski, M. D.; Liu, J.; Murphy, C. J.; Liriano, M. L.; Wasio, N. A.; Lucci, F. R.; Flytzani-Stephanopoulos, M.; Sykes, E. C. H. Selective Formic Acid Dehydrogenation on Pt-Cu Single-Atom Alloys. *ACS Catal.* **2017**, *7* (1), 413–420. https://doi.org/10.1021/acscatal.6b02772.

(130) Kim, J.; Roh, C. W.; Sahoo, S. K.; Yang, S.; Bae, J.; Han, J. W.; Lee, H. Highly Durable Platinum Single-Atom Alloy Catalyst for Electrochemical Reactions. *Adv. Energy Mater.* **2018**, *8* (1), 1–8. https://doi.org/10.1002/aenm.201701476.

(131) Yin, A. X.; Min, X. Q.; Zhang, Y. W.; Yan, C. H. Shape-Selective Synthesis and Facet-Dependent Enhanced Electrocatalytic Activity and Durability of Monodisperse Sub-10 Nm Pt-Pd Tetrahedrons and Cubes. *J. Am. Chem. Soc.* **2011**, *133* (11), 3816–3819. https://doi.org/10.1021/ja200329p.

(132) Zhang, S.; Shao, Y.; Yin, G.; Lin, Y. Electrostatic Self-Assembly of a Pt-around-Au Nanocomposite with High Activity towards Formic Acid Oxidation. *Angew. Chemie - Int. Ed.* **2010**, *49* (12), 2211–2214. https://doi.org/10.1002/anie.200906987.

(133) Iyyamperumal, R.; Zhang, L.; Henkelman, G.; Crooks, R. M. Efficient Electrocatalytic Oxidation of Formic Acid Using Au@Pt Dendrimer-Encapsulated Nanoparticles. *J. Am. Chem. Soc.* **2013**, *135* (15), 5521–5524. https://doi.org/10.1021/ja4010305.

(134) Katiyar, N. K.; Nellaiappan, S.; Kumar, R.; Malviya, K. D.; Pradeep, K. G.; Singh, A. K.; Sharma, S.; Tiwary, C. S.; Biswas, K. Formic Acid and Methanol Electro-Oxidation and Counter Hydrogen Production Using Nano High Entropy Catalyst. *Mater. Today Energy* **2020**, *16*, 100393. https://doi.org/10.1016/j.mtener.2020.100393.

(135) Li, J.; Stein, H. S.; Sliozberg, K.; Liu, J.; Liu, Y.; Sertic, G.; Scanley, E.; Ludwig, A.; Schroers, J. Combinatorial Screening of Pd-Based Quaternary Electrocatalysts for Oxygen Reduction Reaction in Alkaline Media †. **2017**, 67–72. https://doi.org/10.1039/c6ta08088j.

(136) Nørskov, J. K.; Rossmeisl, J.; Logadottir, A.; Lindqvist, L.; Lyngby, D.-; Jo, H. Origin of the Overpotential for Oxygen Reduction at a Fuel-Cell Cathode. **2004**, 17886–17892. https://doi.org/10.1021/jp047349j.

(137) Shao, M.; Chang, Q.; Dodelet, J.; Chenitz, R. Recent Advances in Electrocatalysts for Oxygen Reduction Reaction. **2016**. https://doi.org/10.1021/acs.chemrev.5b00462.

(138) Löffler, T.; Meyer, H.; Savan, A.; Wilde, P.; Garzón Manjón, A.; Chen, Y. T.; Ventosa, E.; Scheu, C.; Ludwig, A.; Schuhmann, W. Discovery of a Multinary Noble Metal–Free Oxygen Reduction Catalyst. *Adv. Energy Mater.* **2018**, *8* (34), 1–7. https://doi.org/10.1002/aenm.201802269.

(139) Qiu, H. J.; Fang, G.; Wen, Y.; Liu, P.; Xie, G.; Liu, X.; Sun, S. Nanoporous High-Entropy Alloys for Highly Stable and Efficient Catalysts. *J. Mater. Chem. A* **2019**, *7* (11), 6499–6506. https://doi.org/10.1039/c9ta00505f.

(140) Yao, Y.; Huang, Z.; Li, T.; Wang, H.; Liu, Y.; Stein, H. S.; Mao, Y.; Gao, J.; Jiao, M.; Dong, Q.; Dai, J.; Xie, P.; Xie, H.; Lacey, S. D.; Takeuchi, I.; Gregoire, J. M.; Jiang, R.; Wang, C.; Taylor, A. D.; Shahbazian-Yassar, R.; Hu, L. High-Throughput, Combinatorial Synthesis of Multimetallic Nanoclusters. *Proc. Natl. Acad. Sci. U. S. A.* **2020**, *117* (12), 6316–6322. https://doi.org/10.1073/pnas.1903721117.

(141) Batchelor, T. A. A.; Pedersen, J. K.; Winther, S. H.; Castelli, I. E.; Jacobsen, K. W.; Rossmeisl, J. High-Entropy Alloys as a Discovery Platform for Electrocatalysis. *Joule* **2019**, *3* (3), 834–845. https://doi.org/10.1016/j.joule.2018.12.015.

(142) Chu, S.; Majumdar, A. Opportunities and Challenges for a Sustainable Energy Future. *Nature* **2012**, *488* (7411), 294–303. https://doi.org/10.1038/nature11475.

(143) Solmaz, R.; Kardaş, G. Electrochemical Deposition and Characterization of NiFe Coatings as Electrocatalytic Materials for Alkaline Water Electrolysis. *Electrochim. Acta* **2009**, *54* (14), 3726–3734. https://doi.org/10.1016/j.electacta.2009.01.064.

(144) Li, Y.; Zhang, J. Z. Hydrogen Generation from Photoelectrochemical Water Splitting Based on Nanomaterials. *Laser Photonics Rev.* **2010**, *4* (4), 517–528. https://doi.org/10.1002/lpor.200910025.

(145) Zeradjanin, A. R.; Grote, J. P.; Polymeros, G.; Mayrhofer, K. J. J. A Critical Review on Hydrogen Evolution Electrocatalysis: Re-Exploring the Volcano-Relationship. *Electroanalysis* **2016**, *28* (10), 2256–2269. https://doi.org/10.1002/elan.201600270.

(146) 2014-PtRu.Pdf.

(147) Liang, Y.; Li, Y.; Wang, H.; Dai, H. Strongly Coupled Inorganic/Nanocarbon Hybrid Materials for Advanced Electrocatalysis. *J. Am. Chem. Soc.* **2013**, *135* (6), 2013–2036. https://doi.org/10.1021/ja3089923.

(148) Xu, G. R.; Bai, J.; Jiang, J. X.; Lee, J. M.; Chen, Y. Polyethyleneimine Functionalized Platinum Superstructures: Enhancing Hydrogen Evolution Performance by Morphological and Interfacial Control. *Chem. Sci.* **2017**, *8* (12), 8411–8418. https://doi.org/10.1039/c7sc04109h.

(149) Lee, Y.; Suntivich, J.; May, K. J.; Perry, E. E.; Shao-Horn, Y. Synthesis and Activities of Rutile IrO 2 and RuO 2 Nanoparticles for Oxygen Evolution in Acid and Alkaline Solutions. *J. Phys. Chem. Lett.* **2012**, *3* (3), 399–404. https://doi.org/10.1021/jz2016507.

(150) Jaks, M. M. Hypo – Hyper-. **2000**, *45*, 4085–4099.

(151) McKone, J. R.; Sadtler, B. F.; Werlang, C. A.; Lewis, N. S.; Gray, H. B. Ni-Mo Nanopowders for Efficient

 

Electrochemical Hydrogen Evolution. *ACS Catal.* **2013**, *3* (2), 166–169. https://doi.org/10.1021/cs300691m.

(152) Elezović, N. R.; Jović, V. D.; Krstajić, N. V. Kinetics of the Hydrogen Evolution Reaction on Fe-Mo Film Deposited on Mild Steel Support in Alkaline Solution. *Electrochim. Acta* **2005**, *50* (28), 5594–5601. https://doi.org/10.1016/j.electacta.2005.03.037.

(153) Schalenbach, M.; Speck, F. D.; Ledendecker, M.; Kasian, O.; Goehl, D.; Mingers, A. M.; Breitbach, B.; Springer, H.; Cherevko, S.; Mayrhofer, K. J. J. Nickel-Molybdenum Alloy Catalysts for the Hydrogen Evolution Reaction: Activity and Stability Revised. *Electrochim. Acta* **2018**, *259*, 1154–1161. https://doi.org/10.1016/j.electacta.2017.11.069.

(154) Raj, I. A.; Vasu, K. I. Transition Metal-Based Cathodes for Hydrogen Evolution in Alkaline Solution: Electrocatalysis on Nickel-Based Ternary Electrolytic Codeposits. *J. Appl. Electrochem.* **1992**, *22* (5), 471–477. https://doi.org/10.1007/BF01077551.

(155) Cherevko, S.; Geiger, S.; Kasian, O.; Kulyk, N.; Grote, J. P.; Savan, A.; Shrestha, B. R.; Merzlikin, S.; Breitbach, B.; Ludwig, A.; Mayrhofer, K. J. J. Oxygen and Hydrogen Evolution Reactions on Ru, RuO2, Ir, and IrO2 Thin Film Electrodes in Acidic and Alkaline Electrolytes: A Comparative Study on Activity and Stability. *Catal. Today* **2016**, *262*, 170–180. https://doi.org/10.1016/j.cattod.2015.08.014.

(156) Canales, C.; Olea, A. F.; Gidi, L.; Arce, R.; Ramírez, G. Enhanced Light-Induced Hydrogen Evolution Reaction by Supramolecular Systems of Cobalt(II) and Copper(II) Octaethylporphyrins on Glassy Carbon Electrodes. *Electrochim. Acta* **2017**, *258*, 850–857. https://doi.org/10.1016/j.electacta.2017.11.135.

(157) Zhang, G.; Ming, K.; Kang, J.; Huang, Q.; Zhang, Z.; Zheng, X.; Bi, X. High Entropy Alloy as a Highly Active and Stable Electrocatalyst for Hydrogen Evolution Reaction. *Electrochim. Acta* **2018**, *279*, 19–23. https://doi.org/10.1016/j.electacta.2018.05.035.

(158) Liu, M.; Zhang, Z.; Okejiri, F.; Yang, S.; Zhou, S.; Dai, S. Entropy-Maximized Synthesis of Multimetallic Nanoparticle Catalysts via a Ultrasonication-Assisted Wet Chemistry Method under Ambient Conditions. **2019**, *1900015*, 1–6. https://doi.org/10.1002/admi.201900015.

(159) Gao, S.; Hao, S.; Huang, Z.; Yuan, Y.; Han, S.; Lei, L.; Zhang, X.; Shahbazian-Yassar, R.; Lu, J. Synthesis of High-Entropy Alloy Nanoparticles on Supports by the Fast Moving Bed Pyrolysis. *Nat. Commun.* **2020**, *11* (1), 1–12. https://doi.org/10.1038/s41467-020-15934-1.

(160) Wu, D.; Kusada, K.; Yamamoto, T.; Toriyama, T.; Matsumura, S.; Gueye, I.; Seo, O.; Kim, J.; Hiroi, S.; Sakata, O.; Kawaguchi, S.; Kubota, Y.; Kitagawa, H. On the Electronic Structure and Hydrogen Evolution Reaction Activity of Platinum Group Metal-Based High-Entropy-Alloy Nanoparticles. *Chem. Sci.* **2020**. https://doi.org/10.1039/d0sc02351e.

(161) Qiu, H.-J.; Fang, G.; Gao, J.; Wen, Y.; Lv, J.; Li, H.; Xie, G.; Liu, X.; Sun, S. Noble Metal-Free Nanoporous High-Entropy Alloys as Highly Efficient Electrocatalysts for Oxygen Evolution Reaction. *ACS Mater. Lett.* **2019**, *1*, 526–533. https://doi.org/10.1021/acsmaterialslett.9b00414.

(162) Yang, D.; Gates, B. C. Catalysis by Metal Organic Frameworks: Perspective and Suggestions for Future Research. *ACS Catal.* **2019**, *9* (3), 1779–1798. https://doi.org/10.1021/acscatal.8b04515.

(163) Shi, Q.; Fu, S.; Zhu, C.; Song, J.; Du, D.; Lin, Y. Metal-Organic Frameworks-Based Catalysts for Electrochemical Oxygen Evolution. *Mater. Horizons* **2019**, *6* (4), 684–702. https://doi.org/10.1039/c8mh01397g.

(164) Royer, S.; Duprez, D. Catalytic Oxidation of Carbon Monoxide over Transition Metal Oxides. *ChemCatChem* **2011**, *3* (1), 24–65. https://doi.org/10.1002/cctc.201000378.

(165) Yao, Y. F. Y. The Oxidation of CO and Hydrocarbons over Noble Metal Catalysts. *J. Catal.* **1984**, *87* (1), 152–162. https://doi.org/10.1016/0021-9517(84)90178-7.

(166) Barbier, J.; Duprez, D. Reactivity of Steam in Exhaust Gas Catalysis I. Steam and Oxygen/Steam Conversions of Carbon Monoxide and of Propane over PtRh Catalysts. *Appl. Catal. B, Environ.* **1993**, *3* (1), 61–83. https://doi.org/10.1016/0926-3373(93)80069-P.

(167) Swartz, S. L. Catalysis by Ceria and Related Materials Edited by Alessandro Trovarelli (Università Di Udine, Italy). Catalytic Science Series. Volume 2. Series Edited by Graham J. Hutchings. Imperial College Press: London. 2002. Vviii + 508 Pp. $78.00. ISBN: 1-86094-. *J. Am. Chem. Soc.* **2002**, *124* (43), 12923–12924. https://doi.org/10.1021/ja025256e.

(168) Rences, R. E. F. E.; Es, N. O. T. Thermally Stable Single-Atom Platinum-on-Ceria Catalysts via Atom Trapping. **2016**, *353* (6295).

(169) Bell, A. T. The Impact of Nanoscience on Heterogeneous Catalysis. **2003**, *299* (March), 1688–1692.

(170) Arnal, P. M.; Comotti, M. High-Temperature-Stable Catalysts by Hollow Sphere Encapsulation**. **2006**, 8224–8227. https://doi.org/10.1002/anie.200603507.

(171) Chen, C.; Nan, C.; Wang, D.; Su, Q.; Duan, H.; Liu, X. Mesoporous Multicomponent Nanocomposite Colloidal Spheres : Ideal High-Temperature Stable Model Catalysts **. **2011**, 3725–3729. https://doi.org/10.1002/anie.201007229.

(172) Yan, H.; Cheng, H.; Yi, H.; Lin, Y.; Yao, T.; Wang, C.; Li, J.; Wei, S.; Lu, J. Single-Atom Pd 1 /Graphene Catalyst Achieved by Atomic Layer Deposition: Remarkable Performance in Selective Hydrogenation of 1,3-Butadiene. **2015**, 5–8. https://doi.org/10.1021/jacs.5b06485.

(173) Peterson, E. J.; Delariva, A. T.; Lin, S.; Johnson, R. S.; Guo, H.; Miller, J. T.; Kwak, J. H.; Peden, C. H. F.; Kiefer, B.; Allard, L. F.; Ribeiro, F. H.; Datye, A. K. Palladium on Alumina. *Nat. Commun.* **2014**. https://doi.org/10.1038/ncomms5885.

(174) Farsi, S.; Olbrich, W.; Pfeifer, P.; Dittmeyer, R. A Consecutive Methanation Scheme for Conversion of CO 2 – A Study on Ni 3 Fe Catalyst in a Short-Contact Time Micro Packed Bed Reactor. *Chem. Eng. J.* **2020**, *388* (January), 124233. https://doi.org/10.1016/j.cej.2020.124233.

(175) Chen, H.; Fu, J.; Zhang, P.; Peng, H.; Abney, C. W.; Jie, K.; Liu, X.; Chi, M.; Dai, S. Entropy-Stabilized Metal Oxide Solid Solutions as CO Oxidation Catalysts with High-Temperature

Stability. *J. Mater. Chem. A* **2018**, *6* (24), 11129–11133. https://doi.org/10.1039/c8ta01772g.

(176) Chen, H.; Lin, W.; Zhang, Z.; Jie, K.; Mullins, D. R.; Sang, X.; Yang, S.-Z.; Jafta, C. J.; Bridges, C. A.; Hu, X.; Unocic, R. R.; Fu, J.; Zhang, P.; Dai, S. Mechanochemical Synthesis of High Entropy Oxide Materials under Ambient Conditions: Dispersion of Catalysts via Entropy Maximization. *ACS Mater. Lett.* **2019**, *1* (1), 83–88. https://doi.org/10.1021/acsmaterialslett.9b00064.

(177) Okejiri, F.; Zhang, Z.; Liu, J.; Liu, M.; Yang, S.; Dai, S. Room-Temperature Synthesis of High-Entropy Perovskite Oxide Nanoparticle Catalysts through Ultrasonication-Based Method. *ChemSusChem* **2020**, *13* (1), 111–115. https://doi.org/10.1002/cssc.201902705.

(178) Xu, H.; Zhang, Z.; Liu, J.; Do-Thanh, C. L.; Chen, H.; Xu, S.; Lin, Q.; Jiao, Y.; Wang, J.; Wang, Y.; Chen, Y.; Dai, S. Entropy-Stabilized Single-Atom Pd Catalysts via High-Entropy Fluorite Oxide Supports. *Nat. Commun.* **2020**, *11* (1), 1–9. https://doi.org/10.1038/s41467-020-17738-9.

(179) Brunson, G. W. Foil Based Heat Exchanger and Reactor Development. *EFC 2009 - Piero Lunghi Conf. Proc. 3rd Eur. Fuel Cell Technol. Appl. Conf.* **2009**, *72* (3), 193–194.

(180) Schüth, F.; Palkovits, R.; Schlögl, R.; Su, D. S. Ammonia as a Possible Element in an Energy Infrastructure: Catalysts for Ammonia Decomposition. *Energy Environ. Sci.* **2012**, *5* (4), 6278–6289. https://doi.org/10.1039/c2ee02865d.

(181) Ganley, J. C.; Thomas, F. S.; Seebauer, E. G.; Masel, R. I. A Priori Catalytic Activity Correlations: The Difficult Case of Hydrogen Production from Ammonia. *Catal. Letters* **2004**, *96* (3–4), 117–122. https://doi.org/10.1023/B:CATL.0000030108.50691.d4.

(182) Yin, S. F.; Xu, B. Q.; Zhou, X. P.; Au, C. T. A Mini-Review on Ammonia Decomposition Catalysts for on-Site Generation of Hydrogen for Fuel Cell Applications. *Appl. Catal. A Gen.* **2004**, *277* (1–2), 1–9. https://doi.org/10.1016/j.apcata.2004.09.020.

(183) Yin, S. F.; Zhang, Q. H.; Xu, B. Q.; Zhu, W. X.; Ng, C. F.; Au, C. T. Investigation on the Catalysis of CO x -Free Hydrogen Generation from Ammonia. *J. Catal.* **2004**, *224* (2), 384–396. https://doi.org/10.1016/j.jcat.2004.03.008.

(184) Jacobsen, C. J. H. Novel Class of Ammonia Synthesis Catalysts. *Chem. Commun.* **2000**, No. 12, 1057–1058. https://doi.org/10.1039/b002930k.

(185) Jacobsen, C. J. H.; Dahl, S.; Clausen, B. G. S.; Bahn, S.; Logadottir, A.; Nørskov, J. K. Catalyst Design by Interpolation in the Periodic Table: Bimetallic Ammonia Synthesis Catalysts [2]. *J. Am. Chem. Soc.* **2001**, *123* (34), 8404–8405. https://doi.org/10.1021/ja010963d.

(186) Duan, X.; Ji, J.; Yan, X.; Qian, G.; Chen, D.; Zhou, X. Understanding Co-Mo Catalyzed Ammonia Decomposition: Influence of Calcination Atmosphere and Identification of Active Phase. *ChemCatChem* **2016**, *8* (5), 938–945. https://doi.org/10.1002/cctc.201501275.

(187) Boisen, A.; Dahl, S.; Jacobsen, C. J. H. Promotion of Binary Nitride Catalysts: Isothermal N2 Adsorption, Microkinetic Model, and Catalytic Ammonia Synthesis Activity. *J. Catal.* **2002**, *208* (1), 180–186. https://doi.org/10.1006/jcat.2002.3571.

(188) Boisen, A.; Dahl, S.; Nørskov, J. K.; Christensen, C. H. Why the Optimal Ammonia Synthesis Catalyst Is Not the Optimal Ammonia Decomposition Catalyst. *J. Catal.* **2005**, *230* (2), 309–312. https://doi.org/10.1016/j.jcat.2004.12.013.

(189) Podila, S.; Zaman, S. F.; Driss, H.; Alhamed, Y. A.; Al-Zahrani, A. A.; Petrov, L. A. Hydrogen Production by Ammonia Decomposition Using High Surface Area Mo2N and Co3Mo3N Catalysts. *Catal. Sci. Technol.* **2016**, *6* (5), 1496–1506. https://doi.org/10.1039/c5cy00871a.

(190) Pedersen, J. K.; Batchelor, T. A. A.; Bagger, A.; Rossmeisl, J. High-Entropy Alloys as Catalysts for the CO2 and CO Reduction Reactions. *ACS Catal.* **2020**, *10*, 2169–2176. https://doi.org/10.1021/acscatal.9b04343.

(191) Xu, W.; Chen, H.; Jie, K.; Yang, Z.; Li, T.; Dai, S. Entropy-Driven Mechanochemical Synthesis of Polymetallic Zeolitic Imidazolate Frameworks for CO 2 Fixation. *Angew. Chemie - Int. Ed.* **2019**, *58* (15), 5018–5022. https://doi.org/10.1002/anie.201900787.

(192) Nellaiappan, S.; Katiyar, N. K.; Kumar, R.; Parui, A.; Malviya, K. D.; Pradeep, K. G.; Singh, A. K.; Sharma, S.; Tiwary, C. S.; Biswas, K. High-Entropy Alloys as Catalysts for the CO2 and CO Reduction Reactions: Experimental Realization. *ACS Catal.* **2020**, *10* (6), 3658–3663. https://doi.org/10.1021/acscatal.9b04302.

(193) Singh, R. L.; Singh, P. K.; Singh, R. P. Enzymatic Decolorization and Degradation of Azo Dyes - A Review. *Int. Biodeterior. Biodegrad.* **2015**, *104*, 21–31. https://doi.org/10.1016/j.ibiod.2015.04.027.

(194) Vinodgopal, K.; Kamat, P. V. Enhanced Rates of Photocatalytic Degradation of an Azo Dye Using SnO2/TiO2 Coupled Semiconductor Thin Films. *Environ. Sci. Technol.* **1995**, *29* (3), 841–845. https://doi.org/10.1021/es00003a037.

(195) Laszlo, J. A. Regeneration of Azo-Dye-Saturated Cellulosic Anion Exchange Resin by Burkholderia Cepacia Anaerobic Dye Reduction. *Environ. Sci. Technol.* **2000**, *34* (1), 167–172. https://doi.org/10.1021/es990918u.

(196) Kalme, S. D.; Parshetti, G. K.; Jadhav, S. U.; Govindwar, S. P. Biodegradation of Benzidine Based Dye Direct Blue-6 by Pseudomonas Desmolyticum NCIM 2112. *Bioresour. Technol.* **2007**, *98* (7), 1405–1410. https://doi.org/10.1016/j.biortech.2006.05.023.

(197) Konstantinou, I. K.; Albanis, T. A. TiO2-Assisted Photocatalytic Degradation of Azo Dyes in Aqueous Solution: Kinetic and Mechanistic Investigations: A Review. *Appl. Catal. B Environ.* **2004**, *49* (1), 1–14. https://doi.org/10.1016/j.apcatb.2003.11.010.

(198) Lachheb, H.; Puzenat, E.; Houas, A.; Ksibi, M.; Elaloui, E.; Guillard, C.; Herrmann, J. M. Photocatalytic Degradation of Various Types of Dyes (Alizarin S, Crocein Orange G, Methyl Red, Congo Red, Methylene Blue) in Water by UV-Irradiated Titania. *Appl. Catal. B Environ.* **2002**, *39* (1), 75–90. https://doi.org/10.1016/S0926-3373(02)00078-4.

(199) Amin, N. K. Removal of Direct Blue-106 Dye from Aqueous Solution Using New Activated Carbons Developed from Pomegranate Peel: Adsorption Equilibrium and Kinetics. *J.*

*Hazard. Mater.* **2009**, *165* (1–3), 52–62. https://doi.org/10.1016/j.jhazmat.2008.09.067.

(200) Meshko, V.; Markovska, L.; Mincheva, M.; Rodrigues, A. E. Adsorption of Basic Dyes on Granular Acivated Carbon and Natural Zeolite. *Water Res.* **2001**, *35* (14), 3357–3366. https://doi.org/10.1016/S0043-1354(01)00056-2.

(201) Shu, H. Y.; Chang, M. C.; Yu, H. H.; Chen, W. H. Reduction of an Azo Dye Acid Black 24 Solution Using Synthesized Nanoscale Zerovalent Iron Particles. *J. Colloid Interface Sci.* **2007**, *314* (1), 89–97. https://doi.org/10.1016/j.jcis.2007.04.071.

(202) Cao, J.; Wei, L.; Huang, Q.; Wang, L.; Han, S. Reducing Degradation of Azo Dye by Zero-Valent Iron in Aqueous Solution. *Chemosphere* **1999**, *38* (3), 565–571. https://doi.org/10.1016/S0045-6535(98)00201-X.

(203) Matheson, L. J.; Tratnyek, P. G. Reductive Dehalogenation of Chlorinated Methanes by Iron Metal. *Environ. Sci. Technol.* **1994**, *28* (12), 2045–2053. https://doi.org/10.1021/es00061a012.

(204) Agrawal, A.; Tratnyek, P. G. Reduction of Nitro Aromatic Compounds by Zero-Valent Iron Metal. *Environ. Sci. Technol.* **1996**, *30* (1), 153–160. https://doi.org/10.1021/es950211h.

(205) Wang, J. Q.; Liu, Y. H.; Chen, M. W.; Xie, G. Q.; Louzguine-Luzgin, D. V.; Inoue, A.; Perepezko, J. H. Rapid Degradation of Azo Dye by Fe-Based Metallic Glass Powder. *Adv. Funct. Mater.* **2012**, *22* (12), 2567–2570. https://doi.org/10.1002/adfm.201103015.

(206) Tang, Y.; Shao, Y.; Chen, N.; Liu, X.; Chen, S. Q.; Yao, K. F. Insight into the High Reactivity of Commercial Fe-Si-B Amorphous Zero-Valent Iron in Degrading Azo Dye Solutions. *RSC Adv.* **2015**, *5* (43), 34032–34039. https://doi.org/10.1039/c5ra02870a.

(207) Zhao, Y. F.; Si, J. J.; Song, J. G.; Yang, Q.; Hui, X. D. Synthesis of Mg-Zn-Ca Metallic Glasses by Gas-Atomization and Their Excellent Capability in Degrading Azo Dyes. *Mater. Sci. Eng. B Solid-State Mater. Adv. Technol.* **2014**, *181* (1), 46–55. https://doi.org/10.1016/j.mseb.2013.11.019.

(208) Wang, J. Q.; Liu, Y. H.; Chen, M. W.; Dmitri, V. L. L.; Inoue, A.; Perepezko, J. H. Excellent Capability in Degrading Azo Dyes by MgZn-Based Metallic Glass Powders. *Sci. Rep.* **2012**, *2*, 1–6. https://doi.org/10.1038/srep00418.

(209) Lv, Z. Y.; Liu, X. J.; Jia, B.; Wang, H.; Wu, Y.; Lu, Z. P. Development of a Novel High-Entropy Alloy with Eminent Efficiency of Degrading Azo Dye Solutions. *Sci. Rep.* **2016**, *6* (November 2015), 1–11. https://doi.org/10.1038/srep34213.

(210) Wu, S.; Pan, Y.; Lu, J.; Wang, N.; Dai, W.; Lu, T. Effect of the Addition of Mg, Ti, Ni on the Decoloration Performance of AlCrFeMn High Entropy Alloy. *J. Mater. Sci. Technol.* **2019**, *35* (8), 1629–1635. https://doi.org/10.1016/j.jmst.2019.03.025.

(211) Lal, M. S.; Sundara, R. High Entropy Oxides—A Cost-Effective Catalyst for the Growth of High Yield Carbon Nanotubes and Their Energy Applications. *ACS Appl. Mater. Interfaces* **2019**, *11* (34), 30846–30857. https://doi.org/10.1021/acsami.9b08794.

(212) Wu, D.; Kusada, K.; Yamamoto, T.; Toriyama, T.; Matsumura, S.; Kawaguchi, S.; Kubota, Y.; Kitagawa, H. Platinum-Group-Metal High-Entropy-Alloy Nanoparticles. *J. Am. Chem. Soc.* **2020**. https://doi.org/10.1021/jacs.0c04807.

(213) Yao, Y.; Huang, Z.; Li, T.; Wang, H.; Liu, Y.; Stein, H. S.; Mao, Y. High-Throughput , Combinatorial Synthesis of Multimetallic Nanoclusters. https://doi.org/10.1073/pnas.1903721117.

(214) In, O.; With, A. Nstructions For.

(215) Osenciat, N.; Bérardan, D.; Meena, A. K.; Léridon, B.; Dragoe, N. Charge Compensation Mechanisms in Li - Substituted High - Entropy Oxides and Influence on Li Superionic Conductivity. **2019**, No. February, 6156–6162. https://doi.org/10.1111/jace.16511.

(216) Online, V. A. In High Entropy Oxides †. **2016**, 9536–9541. https://doi.org/10.1039/c6ta03249d.

(217) Li, X.; Wei, J.; Li, Q.; Zheng, S.; Xu, Y.; Du, P.; Chen, C.; Zhao, J.; Xue, H.; Xu, Q.; Pang, H. Nitrogen-Doped Cobalt Oxide Nanostructures Derived from Cobalt–Alanine Complexes for High-Performance Oxygen Evolution Reactions. *Adv. Funct. Mater.* **2018**, *28* (23), 1–7. https://doi.org/10.1002/adfm.201800886.

(218) Guo, X.; Zheng, S.; Zhang, G.; Xiao, X.; Li, X.; Xu, Y.; Xue, H.; Pang, H. Nanostructured Graphene-Based Materials for Flexible Energy Storage. *Energy Storage Mater.* **2017**, *9* (July), 150–169. https://doi.org/10.1016/j.ensm.2017.07.006.

(219) Zheng, S.; Li, X.; Yan, B.; Hu, Q.; Xu, Y.; Xiao, X.; Xue, H.; Pang, H. Transition-Metal (Fe, Co, Ni) Based Metal-Organic Frameworks for Electrochemical Energy Storage. *Adv. Energy Mater.* **2017**, *7* (18), 1–27. https://doi.org/10.1002/aenm.201602733.

(220) Lu, Y.; Yu, L.; Lou, X. W. (David). Nanostructured Conversion-Type Anode Materials for Advanced Lithium-Ion Batteries. *Chem* **2018**, *4* (5), 972–996. https://doi.org/10.1016/j.chempr.2018.01.003.

(221) Kübel, C.; Velasco, L.; Wang, D.; Wang, Q.; Talasila, G.; Biasi, L. De; Brezesinski, T.; Bhattacharya, S. S.; Hahn, H.; Breitung, B. High Entropy Oxides for Reversible Energy Storage. *Nat. Commun.* No. 2018. https://doi.org/10.1038/s41467-018-05774-5.

(222) Wang, Q.; Sarkar, A.; Li, Z.; Lu, Y.; Velasco, L. Electrochemistry Communications High Entropy Oxides as Anode Material for Li-Ion Battery Applications : A Practical Approach. *Electrochem. commun.* **2019**, *100* (February), 121–125. https://doi.org/10.1016/j.elecom.2019.02.001.

(223) Qiu, N.; Chen, H.; Yang, Z.; Sun, S.; Wang, Y.; Cui, Y. Lithium Storage Performance. *J. Alloys Compd.* **2019**, *777*, 767–774. https://doi.org/10.1016/j.jallcom.2018.11.049.

(224) Balogun, M. S.; Qiu, W.; Luo, Y.; Meng, H.; Mai, W.; Onasanya, A.; Olaniyi, T. K.; Tong, Y. A Review of the Development of Full Cell Lithium-Ion Batteries: The Impact of Nanostructured Anode Materials. *Nano Res.* **2016**, *9* (10), 2823–2851. https://doi.org/10.1007/s12274-016-1171-1.

(225) Chem, J. M.; Liu, K.; Zheng, J.; Zhong, G.; Yang, Y. For Lithium Ion Batteries. **2011**, 4125–4131. https://doi.org/10.1039/c0jm03127e.

(226) Yan, J.; Wang, D.; Zhang, X.; Li, J.; Du, Q.; Liu, X.; Zhang, J.; Qi, X. Materials A High-Entropy Perovskite Titanate Lithium-Ion Battery Anode. *J. Mater. Sci.* **2020**, *v*. https://doi.org/10.1007/s10853-020-04482-0.

(227) Wang, S. Q.; Hahn, H.; Breitung, B.; Du, A.; Heitjans, P.; Brezesinski, T. As Featured in : Energy & Environmental Science f Ac. **2019**. https://doi.org/10.1039/c9ee00368a.

(228) Zhao, C.; Ding, F.; Lu, Y.; Chen, L.; Hu, Y. S. High-Entropy Layered Oxide Cathodes for Sodium-Ion Batteries. *Angew. Chemie - Int. Ed.* **2020**, *59* (1), 264–269. https://doi.org/10.1002/anie.201912171.

(229) Zheng, D.; Wang, G.; Liu, D.; Si, J.; Ding, T.; Qu, D.; Yang, X.; Qu, D. The Progress of Li–S Batteries—Understanding of the Sulfur Redox Mechanism: Dissolved Polysulfide Ions in the Electrolytes. *Adv. Mater. Technol.* **2018**, *3* (9). https://doi.org/10.1002/admt.201700233.

(230) Huang, J. Q.; Zhang, Q.; Wei, F. Multi-Functional Separator/Interlayer System for High-Stable Lithium-Sulfur Batteries: Progress and Prospects. *Energy Storage Mater.* **2015**, *1*, 127–145. https://doi.org/10.1016/j.ensm.2015.09.008.

(231) Li, W.; Hicks-Garner, J.; Wang, J.; Liu, J.; Gross, A. F.; Sherman, E.; Graetz, J.; Vajo, J. J.; Liu, P. V 2 O 5 Polysulfide Anion Barrier for Long-Lived Li-S Batteries. *Chem. Mater.* **2014**, *26* (11), 3404–3410. https://doi.org/10.1021/cm500575q.

(232) Kong, L.; Chen, X.; Li, B. Q.; Peng, H. J.; Huang, J. Q.; Xie, J.; Zhang, Q. A Bifunctional Perovskite Promoter for Polysulfide Regulation toward Stable Lithium–Sulfur Batteries. *Adv. Mater.* **2018**, *30* (2), 1–7. https://doi.org/10.1002/adma.201705219.

(233) Tao, Y.; Wei, Y.; Liu, Y.; Wang, J.; Qiao, W.; Ling, L.; Long, D. Kinetically-Enhanced Polysulfide Redox Reactions by Nb2O5 Nanocrystals for High-Rate Lithium-Sulfur Battery. *Energy Environ. Sci.* **2016**, *9* (10), 3230–3239. https://doi.org/10.1039/c6ee01662f.

(234) Zhang, Y.; Zhao, Y.; Yermukhambetova, A.; Bakenov, Z.; Chen, P. Ternary Sulfur/Polyacrylonitrile/Mg0.6Ni0.4O Composite Cathodes for High Performance Lithium/Sulfur Batteries. *J. Mater. Chem. A* **2013**, *1* (2), 295–301. https://doi.org/10.1039/c2ta00105e.

(235) Zheng, Y.; Yi, Y.; Fan, M.; Liu, H.; Li, X.; Zhang, R.; Li, M.; Qiao, Z. A High-Entropy Metal Oxide as Chemical Anchor of Polysul Fi de for Lithium-Sulfur Batteries. *Energy Storage Mater.* **2019**, No. February. https://doi.org/10.1016/j.ensm.2019.02.030.

(236) Augustyn, V.; Dunn, B. Environmental Science Pseudocapacitive Oxide Materials for High-Rate Electrochemical Energy Storage. **2014**, 1597–1614. https://doi.org/10.1039/c3ee44164d.

(237) Jin, T.; Sang, X.; Unocic, R. R.; Kinch, R. T.; Liu, X.; Hu, J.; Liu, H.; Dai, S. Mechanochemical-Assisted Synthesis of High-Entropy Metal Nitride via a Soft Urea Strategy. *Adv. Mater.* **2018**, *30* (23), 1–5. https://doi.org/10.1002/adma.201707512.

(238) Zhang, L.; Holt, C. M. B.; Luber, E. J.; Olsen, B. C.; Wang, H.; Danaie, M.; Cui, X.; Tan, X.; Lui, V. W.; Kalisvaart, W. P.; Mitlin, D. High Rate Electrochemical Capacitors from Three-Dimensional Arrays of Vanadium Nitride Functionalized Carbon Nanotubes. *J. Phys. Chem. C* **2011**, *115* (49), 24381–24393. https://doi.org/10.1021/jp205052f.

(239) Lu, X.; Liu, T.; Zhai, T.; Wang, G.; Yu, M.; Xie, S.; Ling, Y.; Liang, C.; Tong, Y.; Li, Y. Improving the Cycling Stability of Metal-Nitride Supercapacitor Electrodes with a Thin Carbon Shell. *Adv. Energy Mater.* **2014**, *4* (4), 1–6. https://doi.org/10.1002/aenm.201300994.

(240) Kong, K.; Hyun, J.; Kim, Y.; Kim, W.; Kim, D. Nanoporous Structure Synthesized by Selective Phase Dissolution of AlCoCrFeNi High Entropy Alloy and Its Electrochemical Properties as Supercapacitor Electrode. *J. Power Sources* **2019**, *437* (April), 226927. https://doi.org/10.1016/j.jpowsour.2019.226927.

(241) Xu, X.; Du, Y.; Wang, C.; Guo, Y.; Zou, J.; Zhou, K.; Zeng, Z.; Liu, Y.; Li, L. High-Entropy Alloy Nanoparticles on Aligned Electronspun Carbon Nano Fi Bers for Supercapacitors. *J. Alloys Compd.* **2020**, *822*, 153642. https://doi.org/10.1016/j.jallcom.2020.153642.

(242) Züttel, A. Materials for Hydrogen Storage & Separation. *Mater. Today* **2003**, No. May, 24–33.

(243) Akiba, E.; Iba, H. Hydrogen Absorption by Laves Phase Related BCC Solid Solution. *Intermetallics* **1998**, *6* (6), 461–470. https://doi.org/10.1016/S0966-9795(97)00088-5.

(244) Dornheim, M. Thermodynamics of Metal Hydrides: Tailoring Reaction Enthalpies of Hydrogen Storage Materials. *Thermodyn. - Interact. Stud. - Solids, Liq. Gases* **2011**, No. November 2011. https://doi.org/10.5772/21662.

(245) Perdana. 済無No Title No Title. *J. Chem. Inf. Model.* **2018**, *53* (9), 1689–1699. https://doi.org/10.1017/CBO9781107415324.004.

(246) Zeng, C. A.; Hu, J. P.; Ouyang, C. Y. Hydrogen Solution in Tetrahedral or Octahedral Interstitial Sites in Al. *J. Alloys Compd.* **2011**, *509* (37), 9214–9217. https://doi.org/10.1016/j.jallcom.2011.06.115.

(247) Ouyang, C.; Lee, Y. S. Hydrogen-Induced Interactions in Vanadium from First-Principles Calculations. *Phys. Rev. B - Condens. Matter Mater. Phys.* **2011**, *83* (4), 1–7. https://doi.org/10.1103/PhysRevB.83.045111.

(248) Scholar.

(249) Gross, K. J.; Züttel, A.; Schlapbach, L. On the Possibility of Metal Hydride Formation Part II: Geometric Considerations. *J. Alloys Compd.* **1998**, *274* (1–2), 239–247. https://doi.org/10.1016/S0925-8388(98)00503-9.

(250) Sandrock, G. Panoramic Overview of Hydrogen Storage Alloys from a Gas Reaction Point of View. *J. Alloys Compd.* **1999**, *293*, 877–888. https://doi.org/10.1016/S0925-8388(99)00384-9.

(251) Latroche, M. Structural and Thermodynamic Properties of Metallic Hydrides Used for Energy Storage. *J. Phys. Chem. Solids* **2004**, *65* (2–3), 517–522. https://doi.org/10.1016/j.jpcs.2003.08.037.

(252) Sakintuna, B.; Lamari-Darkrim, F.; Hirscher, M. Metal Hydride Materials for Solid Hydrogen Storage: A Review. *Int. J. Hydrogen Energy* **2007**, *32* (9), 1121–1140. https://doi.org/10.1016/j.ijhydene.2006.11.022.

(253) Tominaga1999 Protium Absorption-Desorption Properties of Ti–V–Cr Alloys with a BCC Structure.Pdf.

(254) Iba, H.; Akiba, E. Hydrogen Absorption and Modulated Structure in Ti-V-Mn Alloys. *J. Alloys Compd.* **1997**, *253–254*, 21–24. https://doi.org/10.1016/S0925-8388(96)03072-1.

(255) 5.Pdf.

(256) Cho, S. W.; Enoki, H.; Akiba, E. Effect of Fe Addition on Hydrogen Storage Characteristics of Ti0.16Zr0.05Cr0.22V0.57 Alloy. *J. Alloys Compd.* **2000**, *307* (1–2), 304–310. https://doi.org/10.1016/S0925-8388(00)00839-2.

(257) Kohno, T.; Yoshida, H.; Kawashima, F.; Inaba, T.; Sakai, I.; Yamamoto, M.; Kanda, M. Hydrogen Storage Properties of New Ternary System Alloys: La2MgNi9, La5Mg2Ni23, La3MgNi14. *J. Alloys Compd.* **2000**, *311* (2), 5–7. https://doi.org/10.1016/S0925-8388(00)01119-1.

(258) Young, K. hsiung; Nei, J. The Current Status of Hydrogen Storage Alloy Development for Electrochemical Applications. *Materials (Basel).* **2013**, *6* (10), 4574–4608. https://doi.org/10.3390/ma6104574.

(259) Lototskyy, M. V.; Yartys, V. A.; Pollet, B. G.; Bowman, R. C. Metal Hydride Hydrogen Compressors: A Review. *Int. J. Hydrogen Energy* **2014**, *39* (11), 5818–5851. https://doi.org/10.1016/j.ijhydene.2014.01.158.

(260) Reilly, J. J.; Wiswall, R. H. The Higher Hydrides of Vanadium and Niobium1. *Inorg. Chem.* **1970**, *9* (7), 1678–1682. https://doi.org/10.1021/ic50089a013.

(261) Tsukahara, M.; Takahashi, K.; Mishima, T.; Isomura, A.; Sakai, T. Vanadium-Based Solid Solution Alloys with Three-Dimensional Network Structure for High Capacity Metal Hydride Electrodes. *J. Alloys Compd.* **1997**, *253–254*, 583–586. https://doi.org/10.1016/S0925-8388(96)02912-X.

(262) 7.Pdf.

(263) Seo, C. Y.; Kim, J. H.; Lee, P. S.; Lee, J. Y. Hydrogen Storage Properties of Vanadium-Based b.c.c. Solid Solution Metal Hydrides. *J. Alloys Compd.* **2003**, *348* (1–2), 252–257. https://doi.org/10.1016/S0925-8388(02)00831-9.

(264) Cho, S. W.; Han, C. S.; Park, C. N.; Akiba, E. Hydrogen Storage Characteristics of Ti-Cr-V Alloys. *J. Alloys Compd.* **1999**, *288* (1–2), 294–298. https://doi.org/10.1016/S0925-8388(99)00096-1.

(265) Kuriiwa, T.; Tamura, T.; Amemiya, T.; Fuda, T.; Kamegawa, A.; Takamura, H.; Okada, M. New V-Based Alloys with High Protium Absorption and Desorption Capacity. *J. Alloys Compd.* **1999**, *293*, 433–436. https://doi.org/10.1016/S0925-8388(99)00325-4.

(266) Young, K.; Nei, J.; Wong, D. F.; Wang, L. Structural, Hydrogen Storage, and Electrochemical Properties of Laves Phase-Related Body-Centered-Cubic Solid Solution Metal Hydride Alloys. *Int. J. Hydrogen Energy* **2014**, *39* (36), 21489–21499. https://doi.org/10.1016/j.ijhydene.2014.01.134.

(267) Kao, Y.; Chen, S.; Sheu, J.; Lin, J.; Lin, W.; Yeh, J.; Lin, S.; Liou, T.; Wang, C. Hydrogen Storage Properties of Multi-Principal-Component CoFeMnTi x V y Zr z Alloys. *Int. J. Hydrogen Energy* **2010**, *35* (17), 9046–9059. https://doi.org/10.1016/j.ijhydene.2010.06.012.

(268) Kunce, I.; Polanski, M.; Bystrzycki, J. Microstructure and Hydrogen Storage Properties of a TiZrNbMoV High Entropy Alloy Synthesized Using Laser Engineered Net Shaping (LENS). *Int. J. Hydrogen Energy* **2014**, *39* (18), 9904–9910. https://doi.org/10.1016/j.ijhydene.2014.02.067.

(269) Czujko, T. ScienceDirect Microstructures and Hydrogen Storage Properties of La e Ni e Fe e V e Mn Alloys. **2017**, *2*. https://doi.org/10.1016/j.ijhydene.2017.09.039.

(270) Kunce, I.; Polanski, M.; Bystrzycki, J. Structure and Hydrogen Storage Properties of a High Entropy ZrTiVCrFeNi Alloy Synthesized Using Laser Engineered Net Shaping ( LENS ) Structure and Hydrogen Storage Properties of a High Entropy ZrTiVCrFeNi Alloy Synthesized Using Laser Engineered Net Shap. *Int. J. Hydrogen Energy* **2013**, *38* (January), 12180–12189. https://doi.org/10.1016/j.ijhydene.2013.05.071.

(271) Chen, S.; Lee, P.; Lee, H.; Su, H. Hydrogen Storage of C14-Cr u Fe v Mn w Ti x V y Zr z Alloys. **2018**, *210*, 336–347. https://doi.org/10.1016/j.matchemphys.2017.08.008.

(272) Sahlberg, M.; Karlsson, D.; Zlotea, C.; Jansson, U. Superior Hydrogen Storage in High Entropy Alloys. *Nat. Publ. Gr.* **2016**, 1–6. https://doi.org/10.1038/srep36770.

(273) Karlsson, D.; Ek, G.; Cedervall, J.; Zlotea, C.; Møller, K. T.; Hansen, T. C.; Bednarčík, J.; Paskevicius, M.; Sørby, M. H.; Jensen, T. R.; Jansson, U.; Sahlberg, M. Structure and Hydrogenation Properties of a HfNbTiVZr High-Entropy Alloy. *Inorg. Chem.* **2018**, *57* (4), 2103–2110. https://doi.org/10.1021/acs.inorgchem.7b03004.

(274) Perri, L.; Møller, K. T.; Jensen, T. R.; Akiba, E.; Sahlberg, M. Hydrogen Sorption in TiZrNbHfTa High Entropy Alloy. **2019**, *775*, 667–674. https://doi.org/10.1016/j.jallcom.2018.10.108.

(275) Ek, G.; Karlsson, D.; Sahlberg, M.; Sørby, M. H.; Hauback, B. C. ScienceDirect Hydrogen Storage in High-Entropy Alloys with Varying Degree of Local Lattice Strain. **2019**, No. xxxx. https://doi.org/10.1016/j.ijhydene.2019.03.223.

(276) Moe, M.; Ek, G.; Karlsson, D.; Sørby, M. H.; Sahlberg, M.; Hauback, B. C. Acta Materialia Counting Electrons - A New Approach to Tailor the Hydrogen Sorption Properties of High-Entropy Alloys. *Acta Mater.* **2019**, *175*, 121–129. https://doi.org/10.1016/j.actamat.2019.06.002.

(277) Shen, H.; Zhang, J.; Hu, J.; Zhang, J.; Mao, Y.; Xiao, H. A Novel TiZrHfMoNb High-Entropy Alloy for Solar Thermal Energy Storage. **2019**, 1–9. https://doi.org/10.3390/nano9020248.

(278) Hu, J.; Shen, H.; Jiang, M.; Gong, H.; Xiao, H. A DFT Study of Hydrogen Storage in High-Entropy Alloy TiZrHfScMo. *d*, 1–12. https://doi.org/10.3390/nano9030461.

(279) Zepon, G.; Leiva, D. R.; Strozi, R. B.; Bedoch, A.; Figueroa, S. J. A.; Ishikawa, T. T.; Botta, W. J. Hydrogen-Induced Phase Transition of MgZrTiFe0.5Co0.5Ni0.5 High Entropy Alloy. *Int. J. Hydrogen Energy* **2018**, *43* (3), 1702–1708. https://doi.org/10.1016/j.ijhydene.2017.11.106.

(280) Luo, H.; Li, Z.; Raabe, D. Hydrogen Enhances Strength and Ductility of an Equiatomic High-Entropy Alloy. *Sci. Rep.* **2017**, *7* (1), 1–7. https://doi.org/10.1038/s41598-017-10774-4.

(281) Oses, C.; Toher, C.; Curtarolo, S. High-Entropy Ceramics. *Nat. Rev. Mater.* **2020**. https://doi.org/10.1038/s41578-

019-0170-8.

(282) Lacey, S. D.; Dong, Q.; Huang, Z.; Luo, J.; Xie, H.; Lin, Z.; Kirsch, D. J.; Vattipalli, V.; Povinelli, C.; Fan, W.; Shahbazian-Yassar, R.; Wang, D.; Hu, L. Stable Multimetallic Nanoparticles for Oxygen Electrocatalysis. *Nano Lett.* **2019**, *19* (8), 5149–5158. https://doi.org/10.1021/acs.nanolett.9b01523.

(283) Lau, J.; Deblock, R. H.; Butts, D. M.; Ashby, D. S.; Choi, C. S.; Dunn, B. S. Sulfide Solid Electrolytes for Lithium Battery Applications. **2018**, *1800933*, 1–24. https://doi.org/10.1002/aenm.201800933.

(284) Murata, K.; Izuchi, S.; Yoshihisa, Y. Overview of the Research and Development of Solid Polymer Electrolyte Batteries. *Electrochim. Acta* **2000**, *45* (8), 1501–1508. https://doi.org/10.1016/S0013-4686(99)00365-5.

(285) Manuel Stephan, A.; Nahm, K. S. Review on Composite Polymer Electrolytes for Lithium Batteries. *Polymer*. Elsevier BV July 26, 2006, pp 5952–5964. https://doi.org/10.1016/j.polymer.2006.05.069.

(286) Yao, P.; Yu, H.; Ding, Z.; Liu, Y.; Lu, J.; Lavorgna, M.; Wu, J.; Liu, X. Review on Polymer-Based Composite Electrolytes for Lithium Batteries. *Frontiers in Chemistry*. Frontiers Media S.A. August 8, 2019, p 522. https://doi.org/10.3389/fchem.2019.00522.

(287) Rojaee, R.; Cavallo, S.; Mogurampelly, S.; Wheatle, B. K.; Yurkiv, V.; Deivanayagam, R.; Foroozan, T.; Rasul, M. G.; Sharifi-Asl, S.; Phakatkar, A. H.; Cheng, M.; Son, S.; Pan, Y.; Mashayek, F.; Ganesan, V.; Shahbazian-Yassar, R. Highly-Cyclable Room-Temperature Phosphorene Polymer Electrolyte Composites for Li Metal Batteries. *Adv. Funct. Mater.* **2020**, *30* (32), 1910749. https://doi.org/10.1002/adfm.201910749.

(288) Cheng, M.; Ramasubramanian, A.; Rasul, M. G.; Jiang, Y.; Yuan, Y.; Foroozan, T.; Deivanayagam, R.; Tamadoni Saray, M.; Rojaee, R.; Song, B.; Yurkiv, V. R.; Pan, Y.; Mashayek, F.; Shahbazian-Yassar, R. Direct Ink Writing of Polymer Composite Electrolytes with Enhanced Thermal Conductivities. *Adv. Funct. Mater.* **2020**, 2006683. https://doi.org/10.1002/adfm.202006683.

(289) Deivanayagam, R.; Cheng, M.; Wang, M.; Vasudevan, V.; Foroozan, T.; Medhekar, N. V.; Shahbazian-Yassar, R. Composite Polymer Electrolyte for Highly Cyclable Room-Temperature Solid-State Magnesium Batteries. *ACS Appl. Energy Mater.* **2019**. https://doi.org/10.1021/acsaem.9b01455.

(290) Pothukuchi, S.; Li, Y.; Wong, C. P. Development of a Novel Polymer-Metal Nanocomposite Obtained through the Route of in Situ Reduction for Integral Capacitor Application. *J. Appl. Polym. Sci.* **2004**, *93* (4), 1531–1538. https://doi.org/10.1002/app.20626.

(291) Zare, Y.; Shabani, I. Polymer/Metal Nanocomposites for Biomedical Applications. *Mater. Sci. Eng. C* **2016**, *60* (28), 195–203. https://doi.org/10.1016/j.msec.2015.11.023.

(292) Cerón, M. R.; Lai, L. S.; Amiri, A.; Monte, M.; Katta, S.; Kelly, J. C.; Worsley, M. A.; Merrill, M. D.; Kim, S.; Campbell, P. G. Surpassing the Conventional Limitations of CO<inf>2</Inf>separation Membranes with Hydroxide/Ceramic Dual-Phase Membranes. *J. Memb. Sci.* **2018**, *567*. https://doi.org/10.1016/j.memsci.2018.09.028.

(293) Duhoux, B.; Mehrani, P.; Lu, D. Y.; Symonds, R. T.; Anthony, E. J.; Macchi, A. Combined Calcium Looping and Chemical Looping Combustion for Post-Combustion Carbon Dioxide Capture : Process Simulation and Sensitivity Analysis. **2016**, 1158–1170. https://doi.org/10.1002/ente.201600024.

(294) Ada, J.; Diego, L. F. De; Garcı, F.; Gaya, P.; Abad, A.; Casta, M. L. Selection of Oxygen Carriers for Chemical-Looping Combustion. **2004**, No. 3, 371–377. https://doi.org/10.1021/ef0301452.

(295) Amiri, A. Extraction of Oxygen from CO2 in Chemical Looping Using Doped Ceria, Southern, Illinois University, 2017.

(296) Amiri, A; Sims, A; Mondal, K. CO2 Driven Chemical Looping Gasification on Doubly Doped Ceria. In *2017 AIChE Annual Meeting*; minneapolis MN, 2017. https://doi.org/978-0-8169-1102-8.

(297) Sun, S.; Zhao, M.; Cai, L.; Zhang, S.; Zeng, D.; Xiao, R. Performance of CeO2-Modified Iron-Based Oxygen Carrier in the Chemical Looping Hydrogen Generation Process. *Energy and Fuels* **2015**, *29* (11), 7612–7621. https://doi.org/10.1021/acs.energyfuels.5b01444.

(298) He, F.; Wei, Y.; Li, H.; Wang, H. Synthesis Gas Generation by Chemical-Looping Reforming Using Ce-Based Oxygen Carriers Modified with Fe, Cu, and Mn Oxides. *Energy and Fuels* **2009**, *23* (4), 2095–2102. https://doi.org/10.1021/ef800922m.

This review covers the recent developments in catalysis, water splitting, fuel cells, batteries, supercapacitors, and hydrogen storage enabled by the high entropy materials.